

Coherent Vortex States in Two-Dimensional Ideal Fluids

Thesis by
PEI-LONG CHEN

In Partial Fulfillment of the Requirements
for the Degree of
Doctor of Philosophy

California Institute of Technology
Pasadena, California

1996
(Submitted May 22, 1996)

Acknowledgements

It is a pleasure to have the opportunity to express my gratitude to all the people who have helped me through the years toward the completion of this work.

First and foremost, I am grateful to my thesis advisor, Dr. Michael Cross, for directing my research, providing constant support and encouragement, and teaching me how to think and study a physical problem.

I am also thankful to Dr. Peter Weichman for many valuable advice and discussion. A great deal of my education on condensed matter physics is indebted to him.

Thanks also to many people at Caltech during the years for their assistance, especially Drs. Daniel Meiron, Yuhai Tu, Chung-Yu Mou, Eugenia Kuo, Dean Petrich, Jonathan Miller, Ron Lifshitz, and Sima Setayeshgar.

The financial support from California Institute of Technology and National Science Foundation is also greatly acknowledged.

Finally I would like to thank my wife for her patience and encouragement throughout the course of my graduate study.

Abstract

In this thesis we study the coherent vortices of a two-dimensional incompressible ideal fluid (the Euler equations) which is important to many physical systems, including the atmosphere of outer planets, two-dimensional turbulence, and pure electron plasma experiments. Using the statistical equilibrium theory derived recently which respects all the infinite conservation laws of the ideal fluid, we solve the coherent vortex solutions in a disk and an annulus. In addition to finding the solutions, we develop the formulation and numerical scheme for a bifurcation and a thermodynamic stability analysis. Numerical simulations of the Euler equations are also performed to study dynamical relaxation from an initial flow to final steady states.

In these studies we pay attention to the problem of the lack of ergodicity which results from incomplete flow mixing. Ergodicity is assumed in the statistical theory but has not been justified. Our general conclusion concerning ergodicity is as follows: Mixing processes during the dynamics have strong effects on the final steady states. Mixing may not be complete as required for ergodicity, but can happen in particular regions or periods, or even in some special flow modes. When strong mixing does occur, the flow structure follows very closely the prediction of statistical mechanics.

Specifically our statistical calculations are on the following questions: (a) single coherent vortices and their bifurcation behavior in a disk, and comparison with the final states in an electron plasma experiment, (b) the stable state of two identical vortices and the prediction, which agrees well with many experimental and simulation results, of the critical separation for merging, (c) the proposal of “vorticity localization” which is used to explain the recently observed states with regular multiple-vortex patterns, (d) work towards explaining the formation of stable vortices on the surfaces of outer planets under the influence of deeper shear flows. Finally using numerical simulations we study vorticity mixing during the relaxation of a vortex ring and its effect on the final states.

Contents

Acknowledgements	iii
Abstract	iv
1 Introduction	1
2 Theory and Numerical Method	6
2.1 Overview	6
2.2 Two-Dimensional Ideal Fluid	6
2.3 Drift Dynamics of an Electron Column	7
2.4 Conservation Laws	8
2.5 Mean Field Statistical Equilibrium	10
2.6 Nonlinear Bifurcation Analysis	13
2.7 Thermodynamic Instability	16
2.8 Numerical Simulation	18
3 Single Vortices in a Disk	19
3.1 Overview	19
3.2 Single-Vortex Solutions	20
3.3 Bifurcation Analysis	23
3.4 Thermodynamic Instability	27
4 Double and Multiple Vortex States	32
4.1 Overview	32
4.2 Mean Field Two-Vortex Solutions in a Disk	33
4.3 Thermodynamic Stability	38
4.3.1 Separation of Eigenmodes	38
4.3.2 Nonmixing Eigenmodes	39

4.3.3	Mixing Eigenmode and Merging Critical Ratio	42
4.4	Vorticity Localization	45
4.4.1	Two-Vortex State in a Large System	45
4.4.2	Vorticity Localization in Mean Field Solution	48
4.4.3	Multiple-Vortex Solution	49
5	Vortex Formation in an Annulus	52
5.1	Overview	52
5.2	Inner Circulation and Background Shear	53
5.3	Axisymmetric Solutions	54
5.4	Bifurcation to Coherent Vortex	56
5.5	Single-Vortex Solution	58
6	Dynamical Relaxation	65
6.1	Overview	65
6.2	Relaxation of the $m=2$ Instability	67
6.3	Relaxation of the $m=3$ Instability	72
6.4	Higher Mode Instability	77
6.5	Conclusion	77
7	Summary and Conclusion	80
	Bibliography	82

List of Figures

3.1	Energy-entropy relations for mean field solutions in a disk.	20
3.2	Vorticity distributions for single-vortex solutions in a disk.	22
3.3	Comparison of q_2 between calculations and experiments.	24
3.4	Bifurcation behavior for $Q = 0.2$ and $M = 0.04$	25
3.5	Bifurcation behavior for $Q = 0.2$ and $M = 0.06$	26
3.6	Equation of state for $Q = 0.2$ and $M = 0.06$	28
3.7	Largest eigenvalues for symmetric solutions.	29
3.8	$m = 1$ modes from the bifurcation and thermodynamic stability analysis.	30
3.9	Largest eigenvalues for off-center vortices.	31
4.1	Vorticity distribution contour plots for two-vortex solutions.	34
4.2	Angular frequency from two-vortex solutions and two point vortices. .	35
4.3	Entropies for two-vortex and single-vortex solutions.	37
4.4	Largest eigenvalues for two-vortex solutions.	39
4.5	Vorticity distribution and eigenmode contour plots.	40
4.6	Constant entropy contours for odd eigenmodes.	42
4.7	Displacement ratio for odd eigenmodes.	43
4.8	Contour plots of vorticity field and corotating stream function for two circular vortices.	46
4.9	Vorticity field and corotating stream function for two circular vortices.	47
4.10	Uneven two-vortex “local” mean field solutions.	50
4.11	Three and four vortex “local” mean field solutions.	51
4.12	Six and seven circular vortices.	51
5.1	Axisymmetric solutions in the annulus.	55
5.2	Phase diagram for asymmetric solutions.	57
5.3	Axisymmetric vorticity distributions at the bifurcation.	58

5.4	Energy-entropy relations for symmetric and single-vortex solutions. . .	59
5.5	Vorticity contour plots for symmetric and single-vortex solutions. . .	60
5.6	Bifurcation behavior for asymmetric solutions.	62
5.7	Vorticity contour plot for $Q = 3.14$, $M = 19.67$, $C = 0.875$, and $\beta = -12.8$	64
6.1	(a) $t = 0$ and (b) $t = 65$	68
6.1	(c) $t = 100$ and (d) $t = 200$	68
6.1	(e) $t = 300$ and (f) $t = 400$	69
6.1	(g) $t = 500$ and (h) $t = 600$. Dynamical relaxation of a vortex ring with the $m = 2$ instability.	69
6.2	$\psi + \Omega r^2$ versus $\ln[q/\omega - 1]$ plots for the $m = 2$ instability.	71
6.3	(a) $t = 0$ and (b) $t = 30$	73
6.3	(c) $t = 100$ and (d) $t = 200$	73
6.3	(e) $t = 400$ and (f) $t = 800$	74
6.3	(g) $t = 1200$ and (h) $t = 1500$. Dynamical relaxation of a vortex ring with the $m = 3$ instability.	74
6.4	$\psi + \Omega r^2$ versus $\ln[q/\omega - 1]$ plots for the $m = 3$ instability.	76
6.5	$\psi + \Omega r^2$ versus $\ln[q/\omega - 1]$ plots for the $m = 4$ and $m = 5$ instability.	78

Chapter 1 Introduction

In this thesis we study the solutions of the statistical equilibrium theory [1, 2, 3] of a two-dimensional incompressible ideal fluid (the Euler equations). Since the statistical theory is developed assuming ergodicity of the flow, i.e, that the dynamics samples all the phase space consistent with the conservation laws, its usefulness depends on the validity of ergodicity. Our main goals are to demonstrate that the results from statistical mechanics agree with real physical systems at least in some cases we have considered, and make predictions about some phenomena not yet observed. For the systems we have considered, a disk and an annulus, there are many relevant physical systems, including the coherent vortices in planetary atmospheres with the Great Red Spot of Jupiter as the best example, the emergence of coherent structures from two-dimensional turbulence, and a pure electron plasma in a strong magnetic field. This statistical approach holds the promise of understanding equilibrium states without the numerically expensive process of solving the long time evolution of the dynamical equations.

The Great Red Spot of Jupiter is a remarkable phenomenon which has excited astronomers and physicists since its first observation. We can now say that this structure has remained stable for over three hundred years, a very long time compared to the time scale of the small features of the flow in the turbulent background that usually last for a few hours or a day. Most current models [4, 5, 6, 7, 8, 9, 10, 11] for the Great Red Spot assume a two-layer model where a thin upper layer containing the vortices is evolving on a deeper steady stratified zonal flow. From observational data of the surface flow, papers [4, 6, 7, 10] using different assumptions to derive Jupiter's deeper atmosphere, which can not be observed directly, have shown numerically that stable coherent vortices on the upper layer similar to the Great Red Spot can exist. Furthermore simulations done by Dowling and Ingersoll [10] demonstrate the genesis of a GRS-like vortex from an initial zonal upper layer in a time scale about 2000

days. This single large vortex is formed through the coalescence of small eddies from the initial instability of the zonal flow, and persists indefinitely against dissipation by absorbing a constant supply of smaller eddies. On the other hand the numerical simulations done by Marcus [9, 11] and experiments by Sommeria *et al.* [12] of a two-dimensional fluid in an annulus have tried to understand the influence of a simple shearing zonal flow on the formation of coherent vortices. The simulations show a generic requirement of a background shearing flow for the production of a single large vortex. Although dissipation and driving by the absorption of small scale vorticity must clearly be involved in a complete theory of the Great Red Spot, the tendency of an inviscid two-dimensional fluid to form coherent vortices may explain the basic mechanism of this phenomenon and an equilibrium description may be used. The background shearing flow can be included as an external field in the equilibrium theory and comparison with the dynamical studies can be made.

Two-dimensional turbulence has been the subject of extensive study recently. In a numerical simulation [13] of two-dimensional large-Reynolds-number turbulence, McWilliams showed that the flow has its vorticity concentrated in a small fraction of the spatial region. The traditional cascade picture with the transfer of vorticity to smaller scales and transfer of energy to larger scales is suppressed when the vorticity concentrations on intermediate scales are a dominant component of the total vorticity field. These coherent vortices have lifetimes long compared with the typical eddy turnover time for the turbulence. Many simulations and experiments [14, 15, 16, 17, 18, 19, 20] have confirmed this picture and the general idea now is that a featureless turbulent flow with only initial small scale motions will first relax to many isolated vortices in the characteristic time scale of nonlinear interactions in a turbulent flow. These vortices will then be advected by their mutual interactions with merging events from time to time when two vortices happen to come too close. Eventually a stable state is reached with very few large coherent vortices. For example, one positive and one negative coherent vortex are formed at opposite locations in the final equilibrium of the simulation by Matthaeus *et al.* [18]. These final states will then gradually dissipate in the viscous time scale. A turbulence decay model using this idea of

successive vortex mergings proposed by Carnevale *et al.* [21] agrees better with the numerical simulations than the selective decay hypothesis [22] does. With these studies showing a final equilibrium state only decaying in a viscous time scale, the statistical equilibrium of a two-dimensional ideal fluid becomes a natural method to describe these states.

It is difficult to perform experiments on a fluid to study the dynamics of the two-dimensional Euler flow due to the relatively large viscous effects in the real fluid. A shallow water system needed to approximate a two-dimensional situation also introduces a viscous boundary layer near the bottom plate [19, 20, 23]. Perhaps the best experimental system to model a two-dimensional ideal fluid is a pure electron plasma in a magnetic field. Under suitable conditions the dynamics of the electrons is two-dimensional and follows the guiding center motion. The governing equations can then be shown to be the same as the Euler equations: the integrated electron density along the direction of the magnetic field corresponds to the vorticity field and the electric field plays the role of the fluid stream function. Many experiments on the electron system have been done to study the dynamics and equilibrium states. These experiments include studies of the detailed properties of a single vortex [24], two-vortex equilibria and vortex merging [25, 26], relaxation and decay of the $m = 2$ diocotron mode [27], relaxation of a hollow distribution [28], different m mode instabilities of a ring distribution [29], persistent vorticity holes [30], and the formation of coherent vortices from initial small scale motion [31]. The loss of electrons will be minimal as long as electrons are far away from the apparatus walls. Experimental conditions can be reasonably well controlled and thus the experiments provide a large amount of information which can be compared with theoretical predictions and numerical simulations. In this thesis we will use many of these experimental results to compare with our mean field calculations.

The equilibrium description of two-dimensional inviscid fluid flow was first suggested by Onsager [32]. He used a system of identical point vortices to model the ideal fluid and applied statistical mechanics to the system using the Hamiltonian, $H = -\sum_{i \neq j} \omega_i \omega_j \Phi(\mathbf{r}_i, \mathbf{r}_j)$, first written down by Kirchoff [33], with Φ the Green's

function for the Laplacian. Onsager argued that in a bounded system negative temperatures will be found at high enough system energy due to the finite volume of the phase space, which here is the same as the system volume.

The statistical equilibrium equation for a point vortex system is the sinh-Poisson equation [34]. Calculations of the equilibrium states have been done under various conditions [34, 35, 36, 37, 38, 39] and negative temperatures appear in many of these solutions, with the appearance of coherent vortices. However, in the point vortex model, where the vorticity distribution is assumed to be a sum of many singular delta functions, the infinite number of conserved quantities in the two-dimensional Euler flow, $\int_{\Omega} d\mathbf{r} \omega^n(\mathbf{r})$ with n any integer and Ω the total volume, are not defined.

The complete statistical mechanics treatment of the two-dimensional Euler flow respecting all the infinite conserved quantities was developed independently by two groups [1, 40, 3]. The mean field equations are integral-differential equations of the vorticity distribution $n_0(\mathbf{r}, \sigma)$, with \mathbf{r} the position vector and σ the vorticity level. These equations give the asymptotic long-time equilibrium from a given initial condition. In the limit of a point vortex model, the sinh-Poisson equation is recovered.

The biggest question about the statistical theory is that ergodicity, the assumption that flow will explore all the phase space, has not yet been justified, and perhaps will not be done in the near future. Some recent experiments [28, 23] have strongly suggested that complete vorticity mixing and ergodicity are not achieved in almost all the studied initial distributions. Thus ergodicity is probably not valid in general but there is still the possibility that it can be true in some cases. Furthermore we believe ergodicity and vorticity mixing can be considered in some restricted sense and the statistical theory is still very useful in this situation. For example when considering two-vortex merging in Section 4.3, we deduce from the comparison between our calculations and experimental data that some flow modes are essentially nonmixing. Therefore we can study approach to thermal equilibrium only in a subspace of the whole phase space, and then we are able to obtain predictions about the vortex merging which agree quantitatively with experimental and simulation results. Another example is that at Section 4.4 we propose the idea of ‘‘vorticity localization’’ where

in some special configurations the flow will only explore some restricted regions and reach local thermal equilibrium. With this idea the mean field solutions can explain recently observed states with regular multiple-vortex patterns. Finally in Chapter 6 numerical simulations of the Euler equations will show that strong vorticity mixing happens in some particular regions and particular time periods. When this happens the vorticity field does follow closely the mean field equations.

This thesis is organized as follows: In Chapter 2 we briefly review the equations for a two-dimensional incompressible ideal fluid and the mean field statistical theory. The formulation of a nonlinear bifurcation analysis and the calculation of thermodynamic stability are also developed. Different numerical methods used in this thesis for the calculations are also described. We start with the discussion of single-vortex solutions in Chapter 3. First, single-vortex solutions are calculated and compared with the results of experiments on equilibrium electron columns. Then the nonlinear bifurcation and thermodynamic stability analysis are used to investigate the interesting bifurcation behavior depending on system parameters. In Chapter 4 two and multiple vortex solutions are studied. After finding two-vortex solutions, we show that thermodynamic stability calculations correctly predict the dynamical stability and also the critical separations for the merging of two-vortex states. From the difficulty of a two-vortex mean field solution in a large system, “vorticity localization” about local equilibrium is proposed and applied to find multiple-vortex solutions. In Chapter 5 we first study the symmetric solutions in an annulus and also their bifurcations to coherent vortex states, then two-dimensional single-vortex solutions similar to the planetary vortices are calculated. The effect of a background shear strength on the formation of these states is extensively investigated. In Chapter 6, we use numerical simulations of the Euler equations to study the different mode instabilities and dynamical relaxations of a vortex ring in a disk. We carefully study the vorticity mixing and nonmixing during the dynamics, and their implications for the final steady states. Finally, in the last chapter we summarize and conclude.

Chapter 2 Theory and Numerical Method

2.1 Overview

In this chapter we first review the governing equations of a two-dimensional incompressible ideal fluid (the Euler equations). The correspondence between the drift dynamics of a pure electron plasma and the Euler flow is next discussed. After pointing out the conservation laws of the system we review the results of the mean field statistical theory developed previously [1, 2, 3]. Also the numerical method used to find mean field solutions will be described. Two further developments beyond solving the mean field equations provide more insight into the system: the first is a nonlinear bifurcation analysis investigating the bifurcation between symmetric and asymmetric solutions; the other is a thermodynamic stability analysis enabling the calculation of the stability of a particular solution. In the last section we describe the numerical simulation of the Euler equations used in Chapter 6.

2.2 Two-Dimensional Ideal Fluid

For a two-dimensional incompressible ideal fluid the mass conservation equation is

$$\nabla \cdot \mathbf{u} = 0.$$

Here \mathbf{u} is the two-dimensional velocity field. This equation can be satisfied automatically by introducing the stream function $\psi(\mathbf{r})$ defined by

$$\mathbf{u}(\mathbf{r}) = \nabla\psi \times \hat{\mathbf{z}} = (\partial\psi/\partial y, -\partial\psi/\partial x).$$

The equation of motion of the flow is

$$\frac{\partial \mathbf{u}}{\partial t} + (\mathbf{u} \cdot \nabla) \mathbf{u} = -\nabla p,$$

where p is the fluid pressure. Taking the curl of the equation of motion we can eliminate the pressure term and have the equation of motion for the vorticity field $\omega(\mathbf{r})\hat{\mathbf{z}} \equiv \nabla \times \mathbf{u}(\mathbf{r})$:

$$\frac{\partial \omega}{\partial t} + (\mathbf{u} \cdot \nabla) \omega = 0. \quad (2.1)$$

The stream function and vorticity field are related by the Poisson's equation:

$$\nabla^2 \psi(\mathbf{r}) = -\omega(\mathbf{r}).$$

2.3 Drift Dynamics of an Electron Column

The dynamics of a pure electron column in an axial magnetic field is known to be well approximated by the two-dimensional guiding center theory [41, 42]. The fast bouncing time scale of an electron along the magnetic field makes the dynamics two-dimensional. Also the gyroradius of an electron is much smaller than the length scale of interest, validating the guiding center approximation. The cross-field drift motion of electrons is then given by

$$\mathbf{v}(\mathbf{r}) = -c\nabla\phi \times \hat{\mathbf{z}}/B.$$

Here ϕ is the electric potential given by the electron density $n(\mathbf{r})$ via the Poisson's equation

$$\nabla^2 \phi = 4\pi en$$

and B is the magnetic field along the z axis. The conservation of the number of electrons requires that

$$\frac{\partial n}{\partial t} + \mathbf{v} \cdot \nabla n = 0.$$

These equations of electron drift dynamics are isomorphic to the two-dimensional Euler equations, with the following correspondence:

$$\omega \longleftrightarrow -4\pi ecn/B$$

$$\psi \longleftrightarrow c\phi/B$$

$$\mathbf{u} \longleftrightarrow \mathbf{v}.$$

Many electron plasma experiments have been done conforming to the above conditions and provided valuable information about the two-dimensional ideal fluid. Electron experiments have the advantage over a real fluid system that the viscosity is much smaller, e.g., experiments with minimal viscous effects over a time period about $10^3 \sim 10^4$ characteristic time scales of the inviscid dynamics have been achieved (see, e.g., reference [25]). The only restriction is that electrons must be far from the apparatus walls to prevent the loss of electrons. Also diagnosis and imaging are more difficult in an electron system although great improvements have been made recently [31, 30]. In this thesis we will make many comparisons between our calculations and the results from this kind of experiment.

2.4 Conservation Laws

Before discussing the statistical equilibrium theory of a two-dimensional ideal fluid, the conserved quantities of the system must be identified. First is the Hamiltonian (kinetic energy) of the two-dimensional Euler flow:

$$\begin{aligned} H &= \frac{1}{2} \int d\mathbf{r} |\mathbf{u}(\mathbf{r})|^2 \\ &= \frac{1}{2} \int d\mathbf{r} \psi(\mathbf{r}) \omega(\mathbf{r}) + \frac{1}{2} \oint_{\text{boundary}} \psi(\nabla \times \psi) \cdot d\mathbf{l} \\ &= \frac{1}{2} \int d\mathbf{r} \int d\mathbf{r}' \omega(\mathbf{r}) \Phi(\mathbf{r}, \mathbf{r}') \omega(\mathbf{r}') + \frac{1}{2} \oint_{\text{boundary}} \psi(\nabla \times \psi) \cdot d\mathbf{l}. \end{aligned}$$

Here the Green's function $\Phi(\mathbf{r}, \mathbf{r}')$ satisfies $\nabla^2 \Phi(\mathbf{r}, \mathbf{r}') = -\delta(\mathbf{r} - \mathbf{r}')$ and in each variable satisfies the same boundary conditions that $\psi(\mathbf{r})$ does.

The two-dimensional Euler flow also has an infinite number of conservation laws of vorticity integrals. For any closed path $\partial\eta(t)$ moving with the fluid, the quantity $\int_{\eta(t)} f(\omega(\mathbf{r}))d\mathbf{r}$, with f an arbitrary function, is conserved by the flow:

$$\frac{d}{dt} \int_{\eta(t)} d\mathbf{r} f(\omega(\mathbf{r})) = \int_{\eta(t)} d\mathbf{r} f'(\omega(\mathbf{r})) \left[\frac{\partial\omega}{\partial t} + \mathbf{u} \cdot \nabla\omega \right] = 0. \quad (2.2)$$

A convenient way to write these conserved quantities is to use the conserved function $G(\sigma)$ defined as the fractional area in the system covered by vorticity equal or smaller than σ :

$$G(\sigma) \equiv \int \vartheta(\sigma - \omega(\mathbf{r}))d\mathbf{r}.$$

Here $\vartheta(x)$ is the step function defined by: $\vartheta(x) = 1$ for $x \geq 0$ and $\vartheta(x) = 0$ for $x < 0$. The derivative $g(\sigma)$ of $G(\sigma)$,

$$g(\sigma) = \frac{dG}{d\sigma} = \int \delta(\sigma - \omega(\mathbf{r}))d\mathbf{r}$$

is then the fractional area covered by vorticity equal to σ . Preserving the conservation of $G(\sigma)$ (or $g(\sigma)$) in statistical mechanics is what makes this theory more desirable than the point vortex model, which models the vorticity field by a collection of point vortices.

If the system has a rotational symmetry, e.g., a disk or an annulus, the angular momentum,

$$L \equiv \int \mathbf{r} \times \mathbf{u}(\mathbf{r})d\mathbf{r} = -\frac{1}{2} \int r^2\omega(\mathbf{r})d\mathbf{r} + \frac{1}{2} \oint_{\text{boundary}} r^2\mathbf{u}(\mathbf{r}) \cdot d\mathbf{l}$$

is also conserved. Since the second term is conserved for a rotationally symmetric system (the integral is just the circulation around the boundary), usually only the first term is used for the angular momentum.

2.5 Mean Field Statistical Equilibrium

Using the above conserved quantities, statistical mechanics predicts that the asymptotic large time equilibrium is given by [3]

$$n_0(\mathbf{r}, \sigma) = \frac{\exp\{-\beta[\sigma(\psi_0(\mathbf{r}) - h(\mathbf{r})) - \mu(\sigma)]\}}{\int_{-\infty}^{\infty} d\sigma' \exp\{-\beta[\sigma'(\psi_0(\mathbf{r}) - h(\mathbf{r})) - \mu(\sigma')]\}}. \quad (2.3)$$

Here the coarse-grained equilibrium stream function ψ_0 and vorticity field ω_0 are determined self-consistently from n_0 ,

$$-\nabla^2\psi_0(\mathbf{r}) = \omega_0(\mathbf{r}) = \int_{-\infty}^{\infty} d\sigma \sigma n_0(\mathbf{r}, \sigma). \quad (2.4)$$

$n_0(\mathbf{r}, \sigma)$ may be considered as the local density of vorticity with strength σ . The function $\mu(\sigma)$ is the Lagrange multiplier of the $g(\sigma)$ constraint, to be determined by:

$$g(\sigma) = \int d\mathbf{r} n_0(\mathbf{r}, \sigma),$$

and the inverse temperature β is determined by fixing the energy. The function $h(\mathbf{r})$ may be used to account for external fields and other conserved quantities in geometries of special symmetry, and is otherwise absent.

In this thesis we will solve the above mean field equations in a unit disk or an annulus. We also choose for simplicity the $g(\sigma)$ corresponding to an initial vorticity distribution with only two vorticity levels, 0 and q ,

$$g(\sigma) = (1 - \alpha)\delta(\sigma) + \alpha\delta(\sigma - q) \quad 0 \leq \alpha \leq V,$$

with V the area of the system. Here α is the area cover by the uniform vorticity q . In an equilibrium state the coarse-grained vorticity field $\omega_0(\mathbf{r})$ will typically take on a continuum of values, always bounded by the value q . The energy of the system is given by

$$E = \frac{1}{2} \int \psi_0 \omega_0 d\mathbf{r} + \frac{1}{2} \oint_{\text{boundary}} \psi_0 \nabla \times \psi_0 \cdot d\mathbf{l}.$$

The entropy is calculated by

$$S = - \int \left[\frac{\omega_0}{q} \ln\left(\frac{\omega_0}{q}\right) + \left(1 - \frac{\omega_0}{q}\right) \ln\left(1 - \frac{\omega_0}{q}\right) \right] d\mathbf{r}. \quad (2.5)$$

Finally because of the rotational symmetry of the disk and annulus, $h(\mathbf{r})$ includes a Lagrange multiplier term Ωr^2 to impose the conservation of angular momentum. With all these considerations, the mean field equations become [3]

$$-\nabla^2 \psi_0(\mathbf{r}) = \omega_0(\mathbf{r}) = \frac{q}{1 + \exp[\beta(q\psi_0(\mathbf{r}) + \Omega r^2 - \mu)]}. \quad (2.6)$$

Here Ω and μ are constants to be determined by the conservation of total vorticity Q and angular momentum M ,

$$Q = \alpha q = \int \omega_0 d\mathbf{r}, \quad M = \int r^2 \omega_0 d\mathbf{r}.$$

In our calculations we will always use $q = 1$.

The mean field equations, Equation (2.3) and (2.4), are complicated differential-integral equations. It seems unrealistic to expect analytical solutions. Even for the simplest case of a two-level initial vorticity where the equations become just differential equations, Equation (2.6), the hope of an analytical solution is still very slim because of the nonlinearity.

This leaves a numerical calculation the only practical way to solve the mean field equations. There are two points which complicate the numerical calculation. First is that the Lagrange multipliers β , Ω , and $\mu(\sigma)$ are unknown beforehand and only determined by matching solutions with prescribed conserved quantities E , M , and $g(\sigma)$. Next is that with a set of values of $(E, M, g(\sigma))$, there can be multiple solutions which can make it difficult to find a particular solution in some situations.

In this thesis we solve Equation (2.6) in a unit disk and an annulus with inner and outer radii one and two. Because of the rotational symmetry of the system, the simplest solutions from the viewpoint of numerical calculations are axisymmetric solutions with only radial dependence. Without azimuthal dependence Equation (2.6)

becomes

$$-\frac{1}{r} \frac{d}{dr} \left(r \frac{d\psi_0(r)}{dr} \right) = \omega_0(r) = \frac{q}{1 + \exp[\beta(q\psi_0(r) + \Omega r^2 - \mu)]}. \quad (2.7)$$

This ordinary differential equation can be numerically integrated by standard methods. To find the values of (μ, Ω, β) for required values of (Q_0, M_0, E_0) , a trust-region method with a Broyden update¹ is used to find the roots of the nonlinear equations

$$\begin{aligned} Q[\omega_0(r; \mu, \Omega, \beta)] - Q_0 &= 0 \\ M[\omega_0(r; \mu, \Omega, \beta)] - M_0 &= 0 \\ E[\omega_0(r; \mu, \Omega, \beta), \psi_0(r; \mu, \Omega, \beta)] - E_0 &= 0. \end{aligned}$$

Because $u_{\mathbf{n}} = 0$ at boundaries with \mathbf{n} denoting the direction normal to the boundary, the stream function is a constant on each separated boundary. Therefore we can use

$$\left. \frac{d\psi_0(r)}{dr} \right|_{r=0} = \psi_0(r=1) = 0$$

as the boundary conditions in a unit disk. For an annulus the stream function on the inner and outer boundaries will be different in general. Without losing generality we can set $\psi_0 = 0$ on the outer boundary. For the inner boundary we first note that, from Equation (2.2), the circulation defined as

$$2\pi C \equiv \int_{\text{a boundary}} \mathbf{u} \cdot d\mathbf{l}$$

is conserved dynamically. Thus in an annulus the circulation on the inner wall C should be specified initially along with the other conserved quantities, i.e., (Q, M, E) . On the other hand the circulation on the outer wall C' is taken care of automatically because of the identity: $Q = 2\pi(C + C')$. Since $\mathbf{u} \cdot d\mathbf{l}$ equals to $(\partial\psi_0/\partial r)d\theta$ on the inner wall of the annulus, the specification of C for a symmetric solution sets the radial derivative of ψ_0 at $r = 1$.

¹The actual routine used is DNQSOL in the MATH77 library developed by JPL.

The calculation becomes more involved when solving Equation (2.6) for general two-dimensional solutions. We use an iterative scheme to find these solutions. First, the domain of the system is discretized into a grid depending on whether a Fourier-finite difference or Fourier-Chebyshev expansion is used. The iteration starts with a guessed vorticity distribution $\omega_t(\mathbf{r})$. Naturally a distribution with (Q, M) approximately equal to the prescribed values and having the same character as the expected solution is used. With this $\omega_t(\mathbf{r})$ we solve the Poisson's equation $\nabla^2\psi_t = -\omega_t$. Next this calculated ψ_t is substituted back into the right-hand side of Equation (2.6) and we see that for each set of (μ, Ω, β) a new ω_t can be calculated. Again the root-seeking algorithm is used here to find the set of (μ, Ω, β) giving an ω_t with required Q , M , and E . Now the iteration can be repeated until a converged $\omega_t(\mathbf{r})$ is reached. Also for the annulus there is the extra quantity C which is to be satisfied by finding the correct value of $\psi_t(\mathbf{r})$ on the inner boundary. We find that this method is robust and usually ω_t converges quickly. There are some variations of this method, e.g., β could be chosen initially and (μ, Ω) are found for prescribed (Q, M) , or S instead of E could be one of the required quantities.

In Chapter 3 solutions in a disk with high symmetry, e.g., two, three, or four fold symmetry, are discussed. In finding these solutions it helps the iteration to explicitly enforce the symmetry at each iteration step.

2.6 Nonlinear Bifurcation Analysis

In Chapter 3 and 5 we will discuss symmetric and asymmetric single-vortex solutions in a disk and an annulus. In addition to finding these solutions, a bifurcation analysis can be performed on the symmetric solutions to understand the bifurcation from symmetric to asymmetric solutions better. Again the mean field equation is

$$\begin{aligned}\omega(\mathbf{r}) = -\nabla^2\psi(\mathbf{r}) &= q / [1 + e^{\beta(q\psi + \Omega r^2 - \mu)}] \\ &\equiv h(\psi(\mathbf{r}), \beta, \Omega, \mu).\end{aligned}\tag{2.8}$$

(Note that we drop the 0-subscript here for ψ and ω from Equation (2.6).) Near the bifurcation point, we write an asymmetric solution as primarily an $m = 1$ perturbation:

$$\begin{aligned}
\psi(\mathbf{r}) &= \psi_0(r) + \delta\psi(\mathbf{r}) = \psi_0(r) + \epsilon\psi_1(r)\cos\theta \\
&\quad + \epsilon^2(\psi_{2,0}(r) + \psi_{2,2}(r)\cos 2\theta) + O(\epsilon^3), \\
\omega(\mathbf{r}) &= \omega_0(r) + \delta\omega(\mathbf{r}) = \omega_0(r) + \epsilon\omega_1(r)\cos\theta \\
&\quad + \epsilon^2(\omega_{2,0}(r) + \omega_{2,2}(r)\cos 2\theta) + O(\epsilon^3), \\
\beta &= \beta_0 + \delta\beta = \beta_0 + \epsilon\beta_1 + \epsilon^2\beta_2 + O(\epsilon^3), \\
\Omega &= \Omega_0 + \delta\Omega = \Omega_0 + \epsilon\Omega_1 + \epsilon^2\Omega_2 + O(\epsilon^3), \\
\mu &= \mu_0 + \delta\mu = \mu_0 + \epsilon\mu_1 + \epsilon^2\mu_2 + O(\epsilon^3).
\end{aligned}$$

We use the 0-subscript here to indicate the symmetric state and ϵ is a small parameter. The $\sin\theta$ term at order ϵ is not included because it is degenerate with the $\cos\theta$ term due to the rotational symmetry. Substituting these expressions into Equation (2.8) we get

$$\begin{aligned}
\delta\omega = -\nabla^2\delta\psi &= \sum_{\alpha} \left. \frac{\delta h}{\delta A_{\alpha}} \right|_0 \delta A_{\alpha} \\
&\quad + \frac{1}{2} \sum_{\alpha\gamma} \left. \frac{\delta^2 h}{\delta A_{\alpha} \delta A_{\gamma}} \right|_0 \delta A_{\alpha} \delta A_{\gamma} + O(\delta A_{\alpha}^3).
\end{aligned}$$

Here A_{α} runs through ψ , β , Ω , and μ . Boundary conditions are as following:

$$\begin{aligned}
\psi_1(r = a) &= \psi_1(r = b) = (\partial\psi_{2,0}/\partial r)_{r=a} \\
&= \psi_{2,0}(r = b) = \psi_{2,2}(r = a) = \psi_{2,2}(r = b) = 0.
\end{aligned}$$

Here a equals zero for the disk and one for the annulus. The parameter b is the radius of the outer boundary. Now we collect terms with the same power of ϵ and angular mode, and set them equal to zero separately. It also becomes apparent here that only

$\psi_{2,0}$ and $\psi_{2,2}$ (not $\psi_{2,1}$) are needed for the ϵ^2 term.

$$\epsilon : \quad B_0\beta_1 + \beta_0 r^2 \Omega_1 - \beta_0 \mu_1 = 0$$

$$\epsilon \cos \theta : \quad (\nabla_1^2 - \beta_0 D_1)\psi_1(r) = 0 \quad (2.9)$$

$$\epsilon^2 \cos 2\theta : \quad (\nabla_2^2 - \beta_0 D_1)\psi_{2,2}(r) = -\frac{1}{4}\beta_0^2 D_2 \psi_1^2 \quad (2.10)$$

$$\begin{aligned} \epsilon^2 : \quad (\nabla_0^2 - \beta_0 D_1)\psi_{2,0}(r) &= \frac{1}{4}\beta_0^2 D_2 \psi_1^2 \\ &+ D_1(B_0\beta_2 + \beta_0 r^2 \Omega_2 - \beta_0 \mu_2)/q \end{aligned} \quad (2.11)$$

$$\epsilon^3 \cos \theta : \quad (\nabla_1^2 - \beta_0 D_1)\psi_{3,1}(r) = G(r; \beta_2, \Omega_2, \mu_2). \quad (2.12)$$

Here

$$\nabla_m^2 \equiv \frac{1}{r} \frac{d}{dr} \left(r \frac{d}{dr} \right) - \frac{m^2}{r^2},$$

$$B_0 \equiv q\psi_0 + \Omega_0 r^2 - \mu_0,$$

$$D_1 \equiv \omega_0(q - \omega_0),$$

$$D_2 \equiv \omega_0(q - \omega_0)(q - 2\omega_0),$$

$$D_3 \equiv \omega_0(q - \omega_0)(q^2 - 6\omega_0 q + 6\omega_0^2),$$

$$\begin{aligned} G \equiv & -\beta_0^2 D_2 \psi_1(\psi_{2,0} + \frac{1}{2}\psi_{2,2}) + D_1 \beta_2 \psi_1 + \frac{1}{8}\beta_0^3 D_3 \psi_1^3 \\ & - \beta_0 D_2 \psi_1(B_0\beta_2 + \beta_0 r^2 \Omega_2 - \beta_0 \mu_2)/q. \end{aligned}$$

The first equation just gives $\beta_1 = \Omega_1 = \mu_1 = 0$. The second one, Equation (2.9), is an eigenvalue equation for $\psi_1(r)$. The solution will only exist for a particular value of β_0 and thus defines the bifurcation point from the symmetric states. After the bifurcation point β_0 and $\psi_1(r)$ are obtained, $\psi_{2,2}(r)$ can be calculated from Equation (2.10). To solve for $\psi_{2,0}(r)$, we need three constraints to determine β_2 , Ω_2 , and μ_2 in Equation (2.11). Two of them are by requiring $\psi_{2,0}(r)$ to give no change in the total vorticity and angular momentum. The third one comes from the solvability condition of the third-order equation, Equation (2.12). Comparing Equation (2.12)

with (2.9), we see that

$$\int \psi_1(r)G(r; \beta_2, \Omega_2, \mu_2)rdr = 0.$$

Combining these three constraints and Equation (2.11) we can calculate $\psi_{2,0}(r)$, β_2 , Ω_2 , and μ_2 . The properties of the asymmetric branch near the bifurcation can then be easily computed from these functions.

2.7 Thermodynamic Instability

The mean field equations are obtained by requiring a vorticity distribution to be an entropy extremum. It remains to be shown whether a particular solution is a maximum, minimum, or saddle point. From thermodynamics we know that the condition for an equilibrium state to be stable is that the entropy is a maximum. Considering the stability will also help us to understand the bifurcation. To determine the thermodynamic stability we add a small variation $\delta n(\mathbf{r}, \sigma)$ to a solution $n_0(\mathbf{r}, \sigma)$ and examine how the system changes. For a closed system with a fixed energy, we will examine the entropy change under the constraints of constant total vorticity, angular momentum, and energy. On the other hand for a system equilibrating with a heat bath at a constant temperature, free energy will be studied with fixed Q , M , and β . Besides these thermodynamic constraints, all the infinite conservation laws of vorticity integrals should also be respected by the δn . Since the state is already in equilibrium, the entropy or free energy will be evaluated to the second order of δn . In our case of a two-level initial vorticity field, the perturbation is just a small $\delta\omega(\mathbf{r})$ and the conservation of the vorticity integrals is always satisfied. The changes in the total vorticity, angular momentum, and energy are

$$\begin{aligned} \delta Q &= \int \delta\omega d\mathbf{r}, & \delta M &= \int r^2 \delta\omega d\mathbf{r}, \\ \delta E &= \int (\psi_0 \delta\omega + \frac{1}{2} \delta\psi \delta\omega) d\mathbf{r} \equiv \delta E^{(1)} + \delta E^{(2)}. \end{aligned} \quad (2.13)$$

The entropy change, up to the second order, is

$$\delta S = \beta \int \psi_0 \delta \omega d\mathbf{r} - \int \frac{(\delta \omega)^2}{2\omega_0(q - \omega_0)} d\mathbf{r} \equiv \delta S^{(1)} + \delta S^{(2)}, \quad (2.14)$$

and the free energy change: $\delta F = \delta S - \beta \delta E = \delta S^{(2)} - \beta \delta E^{(2)}$. For convenience our F differs from the usual free energy by a factor of $-\beta$. Note that in δF the linear terms from δS and δE cancel and we have a quadratic form left. For a closed system, because δE is required to be zero we can also use $\delta S - \beta \delta E$ instead of δS . So for both cases we will investigate $\delta S^{(2)} - \beta \delta E^{(2)}$ but with the constraint $\delta E = 0$ required for a closed system in addition to $\delta Q = \delta M = 0$. In practice only $\delta E^{(1)} = 0$ is needed because δS is only evaluated to second order.

To proceed we expand $\delta \omega(\mathbf{r})$ in a complete set of orthonormal functions $\phi_i(\mathbf{r})$: $\delta \omega(\mathbf{r}) = \sum_i a_i \phi_i(\mathbf{r})$. Then δQ , δM , $\delta E^{(1)}$, and $\delta S^{(2)} - \beta \delta E^{(2)}$ can be expressed as

$$\begin{aligned} \delta Q &= \sum_i Q_i a_i, & \delta M &= \sum_i M_i a_i, & \delta E^{(1)} &= \sum_i E_i a_i, \\ \delta S^{(2)} - \beta \delta E^{(2)} &= \sum_{ij} S_{ij} a_i a_j. \end{aligned} \quad (2.15)$$

Here Q_i , M_i , and E_i are vectors and S_{ij} is a matrix depending only on $\omega_0(\mathbf{r})$ and $\psi_0(\mathbf{r})$. Now we make an arbitrary linear transformation from a_i to b_i but requiring

$$\begin{aligned} b_1 &= \sum_i Q_i a_i, & b_2 &= \sum_i M_i a_i, \\ b_3 &= \sum_i E_i a_i \text{ (in the case of a closed system.)} \end{aligned}$$

The constraints can now be satisfied with $b_1 = b_2 = 0$ (or $b_1 = b_2 = b_3 = 0$ for a closed system.) In this new representation, S_{ij} changes to another matrix T_{ij} and $\delta S^{(2)} - \beta \delta E^{(2)}$ becomes $\sum_{ij > 2(\text{or } 3)} T_{ij} b_i b_j$. By removing the first two (or three) rows and columns from T_{ij} , we can perform the analysis without worrying about the constraints. If all eigenvalues of the new T_{ij} are negative, the state (ω_0, ψ_0) will be a free energy (or entropy) maximum. When the largest eigenvalue reaches zero as the system parameters change, the state becomes a saddle point.

2.8 Numerical Simulation

In Chapter 6 we will study the dynamical relaxations of a two-dimensional ideal fluid by using the numerical simulation of the Euler equations with a small viscosity term in a disk,

$$\frac{\partial \omega}{\partial t} + (\mathbf{u} \cdot \nabla) \omega = \nu \nabla^2 \omega.$$

We discretize the disk in the polar coordinate. The Poisson's equation for the stream function ψ is then solved by the Fourier expansion in the azimuthal direction and the fourth-order finite difference in the radial direction. All the spatial derivatives are calculated with the fourth-order finite difference and the time marching scheme is the second-order Adam-Bashford method. The common difficulty of the coordinate singularity due to the diminishing grid spacing near the origin in the polar coordinate is alleviated by using a large enough viscosity constant. A constantly changing rotating frame may also be used to reduce average flow velocity and hence the effective Courant number.

All the results in Chapter 6 are done at a resolution 128×128 . The Reynolds number of the flow is about $10^5 \sim 10^6$ from typical flow velocity, system size, and viscosity. In the time period of interest, the changes in the total vorticity, angular momentum, and energy are less than a few percent. Higher Reynolds numbers and slower rates of change for these three quantities can be achieved by using a higher resolution and smaller viscosity, but we find that the conclusions in Chapter 6 remain the same. The other conserved quantities of higher-moment vorticity integrals, e.g., the enstrophy defined as $\int \omega^2 d\mathbf{r}$, change significantly. This is because during the dynamics the viscosity and finite grid size introduce a local averaging on the flow. However we think this is not a serious problem because we are mainly interested in the final large scale smooth vorticity distribution, and this is supported by results from different viscosity constants and resolutions. Note that the coarse-grained equilibrium distributions from the statistical theory also do not conserve these higher-moment vorticity integrals.

Chapter 3 Single Vortices in a Disk

3.1 Overview

We start our discussion with single-vortex solutions in a unit disk. These single vortices are the first step to understand the generic formation of coherent vortices in a two-dimensional ideal fluid. More specifically an electron plasma experiment [24] has been done in a cylinder to study these vortices. Theoretical single-vortex solutions in a disk have been investigated in reference [39, 43] using the point vortex model or the mean field theory. In these two papers symmetric single-vortex solutions at the disk center are calculated and a bifurcation to off-center single vortices is found by a linear bifurcation analysis on symmetric solutions. In this section we solve the two-dimensional mean field equations for both symmetric and asymmetric solutions to get a complete picture on the problem. We compare their thermodynamic quantities directly and show explicitly that there is a critical energy beyond which off-center vortices are thermodynamically more probable states. The shapes of the off-center vortices are also compared with the results of the electron plasma experiment [24].

We then do a second-order bifurcation analysis at the bifurcation point. By extending the analysis to second order we can quickly identify the bifurcation type and understand the behavior of off-center vortices near it. Although we could also get this information by computing all two-dimensional off-center asymmetric solutions, this analysis is faster and free of the numerical error from discretizing the disk. Combining weakly nonlinear analytic results with numerical solutions, we will show that the bifurcation is always supercritical (second-order transition) when the system energy is varied. However if the system temperature is used as the control parameter, a subcritical bifurcation (first-order transition) can happen for some parameters. An interesting aspect of this first-order transition is that, because of the long range vortex-vortex interaction, the system will not be in a mixture of two stable states as

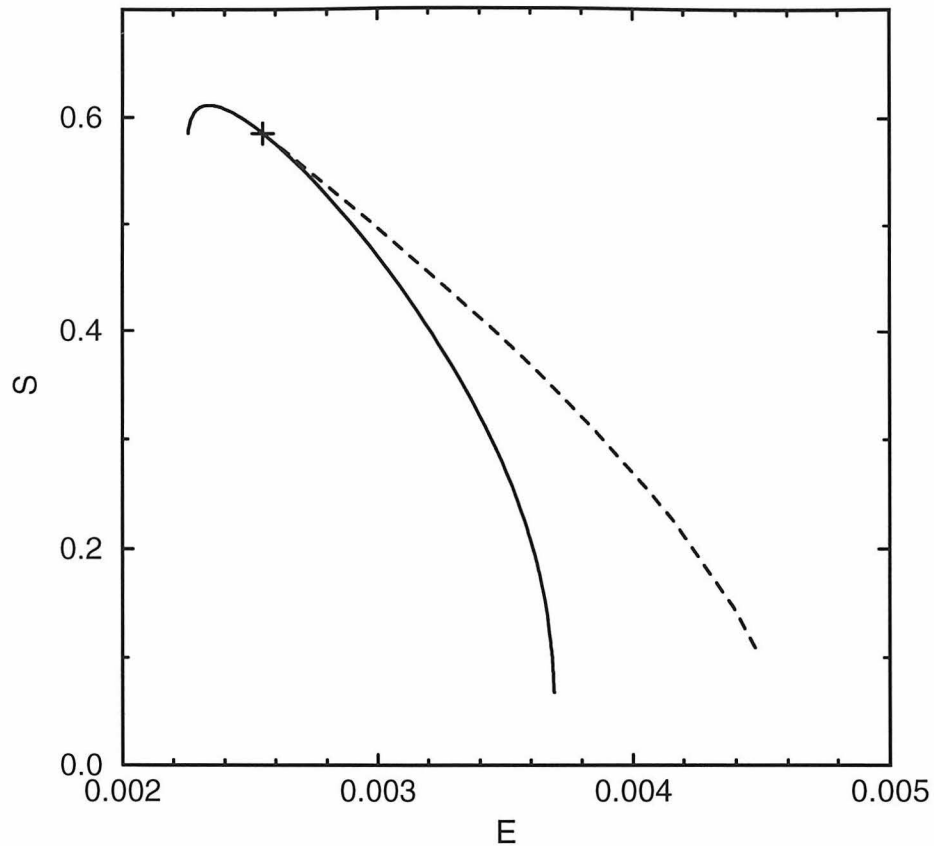


Figure 3.1: Mean field solutions for $Q = 0.2$ and $M = 0.04$. Solid line:symmetric solutions; dashed line:off-center vortices; cross:bifurcation point.

occurs in a system with short range interactions (e.g., water). Instead the system stays at an “unstable” state with fixed energy. Finally we use a stability analysis to calculate explicitly the thermodynamic stability properties of a solution, i.e., whether it is a local entropy maximum. It will be shown that the stability confirms both bifurcation behaviors.

3.2 Single-Vortex Solutions

Figure 3.1 shows the entropy as a function of energy for the symmetric and off-center vortices with $Q = 0.2$ and $M = 0.04$. The numerical method used was discussed in Section 2.5. Different values of Q and M yield similar results. The energy or

temperature can be considered as an indicator of how closely the vorticity is packed. At the minimum energy limit, corresponding to $\beta \rightarrow \infty$, the symmetric solution has a distribution of $\omega_0(r)$ which is a circular uniform-vorticity patch (Figure 3.2a), with its size ρ and vorticity level σ uniquely determined by Q and M :

$$\pi\rho^2\sigma = Q, \quad \frac{1}{2}\pi\rho^4\sigma = M.$$

It is interesting to note that ρ and σ are independent of the $g(\sigma)$ constraint, i.e., the value of q in the two-level vorticity special case. As the energy increases the vorticity level at the center rises. The entropy also increases but decreases again after passing the point $\beta = dS/dE = 0$ and reaches zero at the high energy limit when $\beta \rightarrow -\infty$. This rise and fall of the entropy is reasonable from the fact that the entropy density,

$$-\frac{\omega_0}{q} \ln\left(\frac{\omega_0}{q}\right) - \left(1 - \frac{\omega_0}{q}\right) \ln\left(1 - \frac{\omega_0}{q}\right), \quad 0 < \omega_0 < q,$$

has a single peak occurring at $\omega_0 = \frac{1}{2}q$. At the high energy limit the vorticity distribution saturates at level q and forms a circular vortex at the center and a vortex ring at the disk boundary, as shown in Figure 3.2b. The amount of vorticity in each region is determined by the angular momentum M . From this vorticity distribution we immediately see that the formation of an off-center vortex is likely to be favored at large energy: all vorticity can then stay in one region with the angular momentum constraint satisfied by adjusting the displacement from the center. When $\beta \rightarrow -\infty$ we again have $S \rightarrow 0$ for off-center vortices (the dashed line) only here the energy is greater than that of symmetric vortices.

The distribution of the off-center branch at the maximum energy limit is an elliptical-like vortex with uniform vorticity q at a certain displacement D from the center. As the energy decreases, the entropy increases and the vortex moves toward the disk center. At a critical energy E_c , D becomes zero and two branches of solutions join together at the bifurcation point. At a fixed energy $E > E_c$ the off-center vortex always has a larger entropy than the symmetric one, i.e., it is a more probable

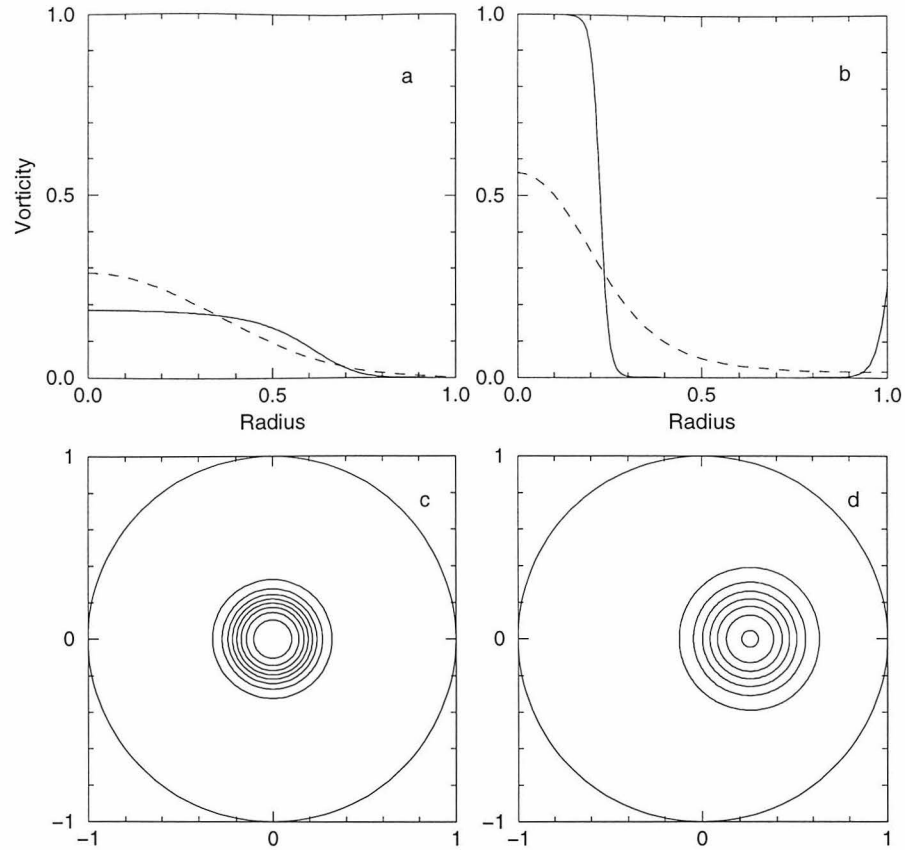


Figure 3.2: Vorticity distributions for $Q = 0.2$ and $M = 0.04$ at various conditions. (a) Symmetric solutions at $\beta = 1$ (dashed line) and $\beta = 800$ (solid line). (b) Symmetric solutions at $\beta = -200$ (dashed line) and $\beta = -1000$ (solid line). (c) Vorticity contours for the symmetric solution at $E = 0.003$. The contour levels start from 0.1 and increase by an interval of 0.1 toward the center. (d) Vorticity contours for the off-center vortex also at $E = 0.003$, with the same contour levels as (c).

state. Contour plots of a symmetric and off-center vortices at the same energy are plotted in Figure 3.2c and 3.2d, showing the off-center vortex is more diffusive than the symmetric one, yielding a higher entropy.

Fine *et al.* [24] have measured the electron density, equivalent to the vorticity distribution, for single equilibrium electron columns. They study how the quadrupole moment q_2 and rotating frequency f of off-center vortices depend on vortex sizes and distances to the disk center. Here q_2 is defined as $(p_{xx} - p_{yy})/(p_{xx} + p_{yy})$, with $p_{xx} \equiv \int x^2 \omega(\mathbf{r}) d\mathbf{r}$ and similarly for p_{yy} , to measure distortion of a vortex from a

circular shape. The position (x, y) is measured from the center of the vortex along the major and minor axes (defined as for an ellipse.) Although we use values of E at fixed Q and M in Figure 3.1 to describe the solutions, to compare our calculations with the experimental results, it is better to use different M at fixed Q and β . At a fixed β , different M will give vortices at different D with roughly the same internal distribution, similar to the vortices produced in the experiment.

For three different total vorticities measured in the experiment, we plot q_2 versus D for β equal to -1000 (solid lines) and -200 (dashed lines) in Figure 3.3. The vortices are very close to uniform patches for the first β and have some smooth distribution for the second. First we see that in all three cases both values of β give rather close values of q_2 . The likely physical reason is that distortion comes mainly from the effect of the boundary (or in terms of the position of the image charge), and is mostly determined by the position of a vortex, not its detailed distribution. The measured q_2 from the experiment, shown as symbols in Figure 3.3, are consistent with our calculations. Although the electron columns have internal distributions closer to those of $\beta = -200$ than $\beta = -1000$, experimental errors make it difficult to tell which line is closer to the experiment. This may also explain why an elliptical constant vorticity patch approximation [44] shown as the dotted lines also gives consistent q_2 values. At small D the results are almost identical to the mean field solutions with the larger negative β but deviate from the experimental results when vortices come close to the boundary. On the other hand the mean field calculations describe correctly the trend of the experimental data at large D .

3.3 Bifurcation Analysis

From the viewpoint of symmetric solutions, a bifurcation to off-center vortices occurs at the critical energy. In principle we can understand the nature of the bifurcation and behavior near it by computing all the solutions on the off-center branch. However this is very time-consuming and there is always the uncertainty whether the solutions are close enough to the bifurcation. Using the second-order bifurcation anal-

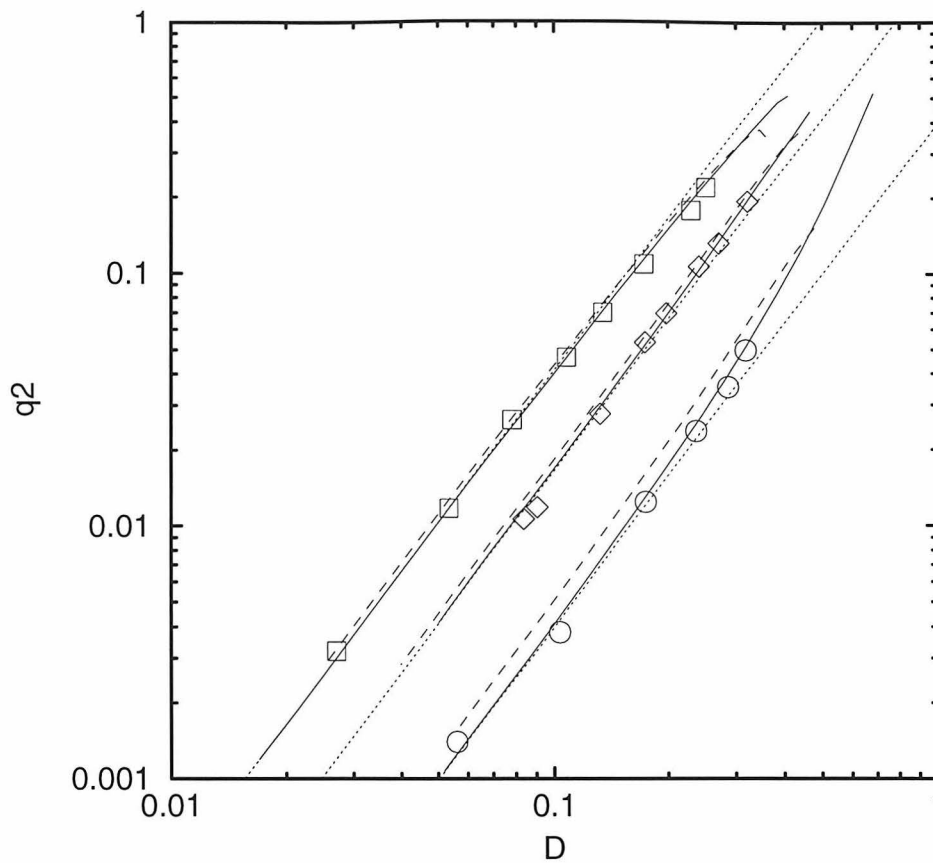


Figure 3.3: q_2 as a function of D . The three groups of lines correspond to, from top to bottom, $Q = 1.5837$, 1.0936 , and 0.45365 . See text for further descriptions.

ysis described in Section 2.6, we can not only quickly find the bifurcation point (from the first-order calculation) but also the bifurcation behavior (from the second-order results).

Properties of asymmetric vortices can be quickly calculated from the functions $\omega_1(r)$, $\omega_{2,0}(r)$, $\omega_{2,2}(r)$ of the bifurcation analysis. For example,

$$\begin{aligned}
 D &= \epsilon\pi \int \omega_1 r^2 dr / Q, \\
 q_2 &= (\epsilon^2\pi \int \omega_{2,2} r^3 dr - QD^2) / (M - QD^2), \\
 E - E_c &= \epsilon^2 2\pi \int \psi_0 \omega_{2,0} r dr + \epsilon^2 \frac{\pi}{2} \int \psi_1 \omega_1 r dr,
 \end{aligned}$$

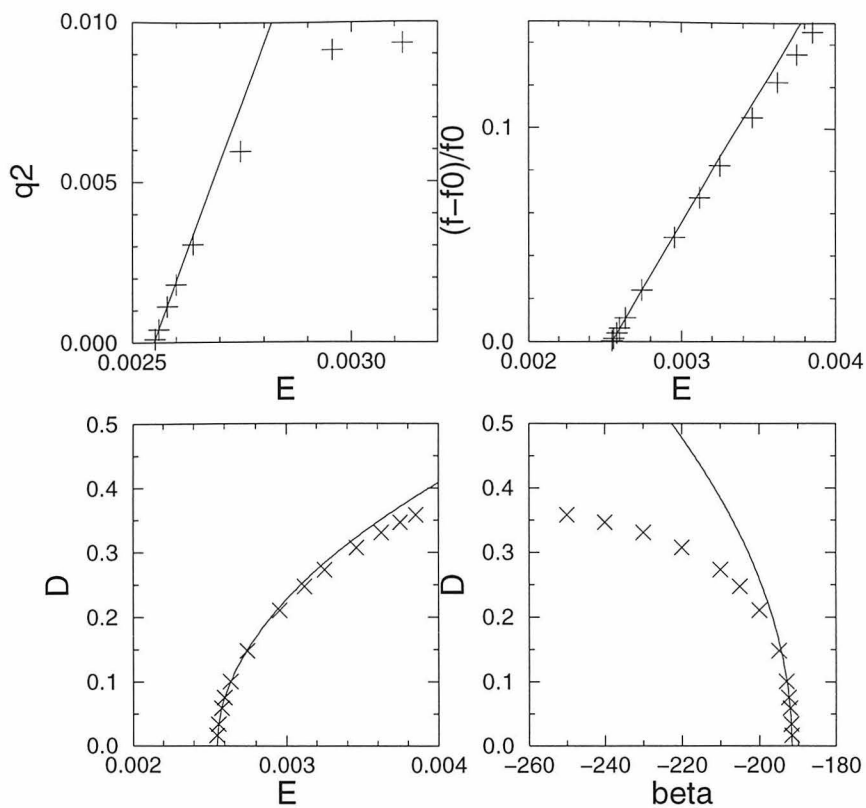


Figure 3.4: Off-center vortex solutions for $Q = 0.2$ and $M = 0.04$. Solid lines: bifurcation analysis calculations; cross: off-center vortex numerical solutions.

and the rotational frequency shift $\Delta f \equiv (f - f_0)/f_0 = \epsilon^2 \Omega_2 / \Omega_0$, with $f_0 \equiv f(D \rightarrow 0)$.

The bifurcation point calculated from Eq. (2.9) is plotted as a cross in Figure 3.1. We see that it agrees perfectly with the start of the off-center branch. In Figure 3.4 we plot D , q_2 , and Δf as functions of E or β for $Q = 0.2$ and $M = 0.04$. The solid lines are results from bifurcation calculations and we find that the numerical solutions of off-center vortices, shown as crosses, agree well with the lines near the critical energy. If the displacement D is taken as the order parameter of an off-center state, its behavior clearly indicates a supercritical bifurcation. Thermodynamically we have a second-order (continuous) phase transition at E_c .

Interestingly for a larger value of M the situation changes. The bifurcation and

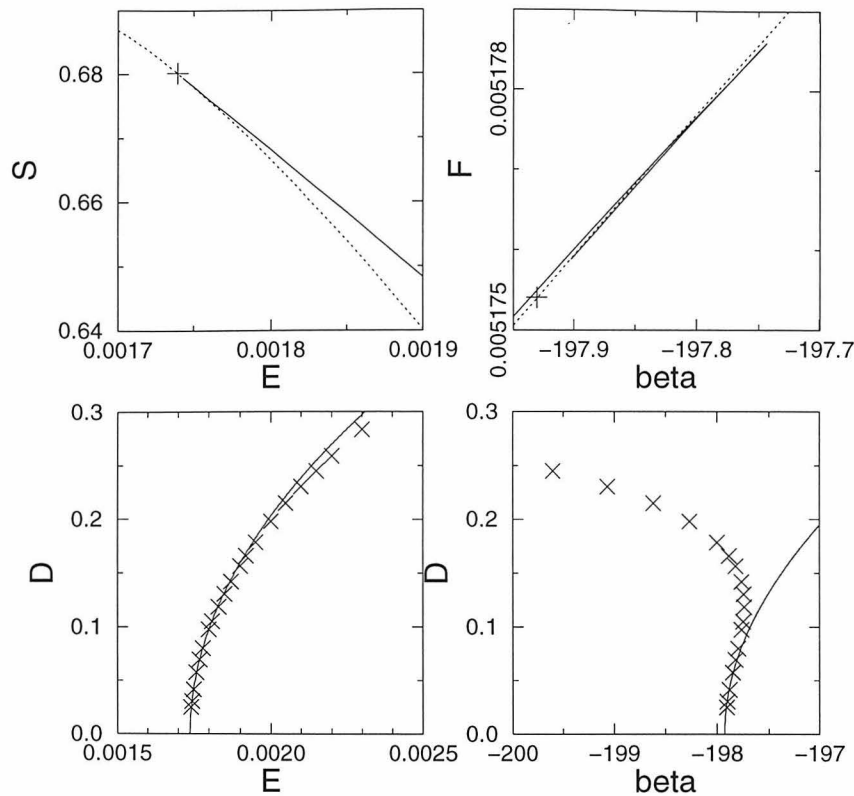


Figure 3.5: Equilibrium states for $Q = 0.2$ and $M = 0.06$. In the upper two graph, solid lines:off-center vortices; dotted lines:symmetric vortices; cross:bifurcation point. In the lower two graphs, solid lines:bifurcation analysis calculations; cross:off-center vortex numerical solutions.

numerical results are shown in Figure 3.5 for $Q = 0.2$ and $M = 0.06$ (larger M yielding a larger vortex). The D versus E curve is similar to the previous case, but now $\beta - \beta_c$ near the bifurcation (which is just $\epsilon^2 \beta_2$ from Eq. (2.11)) is positive. Figure 3.5 indicates that we have a subcritical bifurcation when using the inverse temperature as the control parameter. Thermodynamically when the system is equilibrated with a heat bath at a fixed temperature, the transition to off-center vortices will be first-order. The transition point β_f can be identified from the crossing of the solid and dashed lines in the free energy-inverse temperature plot. Although it may be difficult to see from the plot, in the small segment of the off-center branch near the bifurcation

point (the portion with $dD/d\beta > 0$), $d^2F/d\beta^2$ is negative. This leads to a negative specific heat and indicates the state is thermodynamically unstable.

The behavior becomes clearer when we plot the inverse temperature versus energy in Figure 3.6. Considering the solid line in the blow-up, we have the curve of a typical equation of state with a first-order transition. The dashed line marks the temperature where the transition will occur. However in the vortex system the usual interpretation of a system at the transition temperature as a mixture of two phases no longer applies due to the long range interaction between vortices. When a system at point A is fed energy by a heat bath at the same temperature, the system will not be in an equilibrium state until it gains enough energy to reach point B. If the contact with the heat bath is cut before reaching E_B , for example, at E_C , the system will relax to the equilibrium state C which is stable in an isolated environment. So if the system energy is controlled continuously we can have a continuous transition from symmetric to off-center states.

3.4 Thermodynamic Instability

As discussed in Section 2.7, it remains to be shown whether a particular mean field solution is an entropy maximum. From previous sections, some of the mean field solutions are expected to be unstable, e.g., the symmetric solutions with energy higher than E_c , or the off-center solutions near a subcritical bifurcation point at a fixed temperature. It is our purpose in this section to investigate this property using the thermodynamic instability.

In the unit disk we expand $\delta\omega(\mathbf{r})$, discussed in Section 2.7, in Fourier modes in the azimuthal direction and in Chebyshev polynomials in the radial direction:

$$\delta\omega(\mathbf{r}) = \sum_{m=-\infty}^{\infty} \sum_{\substack{n=0 \\ m+n=\text{even}}}^{\infty} a_{mn} T_n(r) e^{im\theta}. \quad (3.1)$$

Here $m + n$ even is required to give the correct parity for each m mode. When the calculation is applied to a symmetric distribution, the components for different

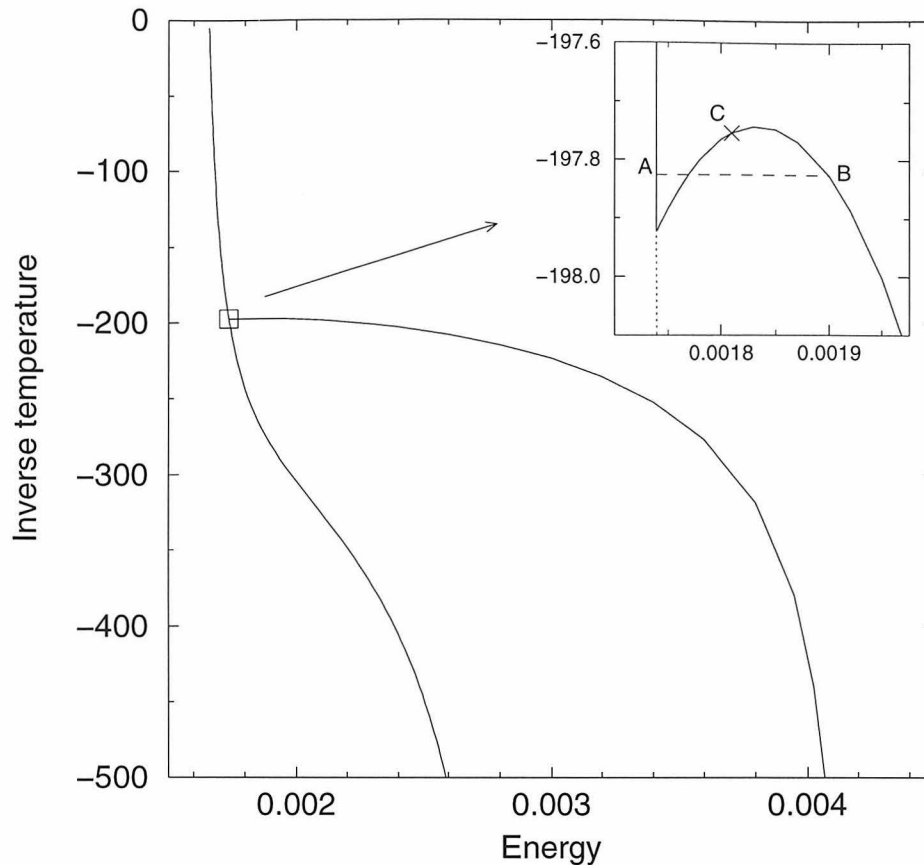


Figure 3.6: $\beta - E$ relation for the symmetric and off-center states with $Q = 0.2$ and $M = 0.06$. The line on the left is the symmetric solutions; on the right the off-center vortices. In the blow-up the symmetric branch below the bifurcation point is drawn dotted and the horizontal dashed line marks the inverse temperature where free energy of both branches cross in Figure 3.5.

m separate and each eigenvector has a definite value of m . The calculation is then faster because each m can be done separately. This is no longer true for an off-center vortex where all m modes are coupled together. Both fixed energy and fixed temperature calculations discussed in Section 2.7 are done as Figure 3.5 shows that different behaviors happen depending on whether the energy or temperature is controlled.

The largest eigenvalues for $m \leq 3$ modes about the symmetric solutions are shown in Figure 3.7 for a closed system with $Q = 0.2$ and $M = 0.04$. For a fixed temperature calculation the $m = 0$ eigenvalues will be different but the results are similar. All

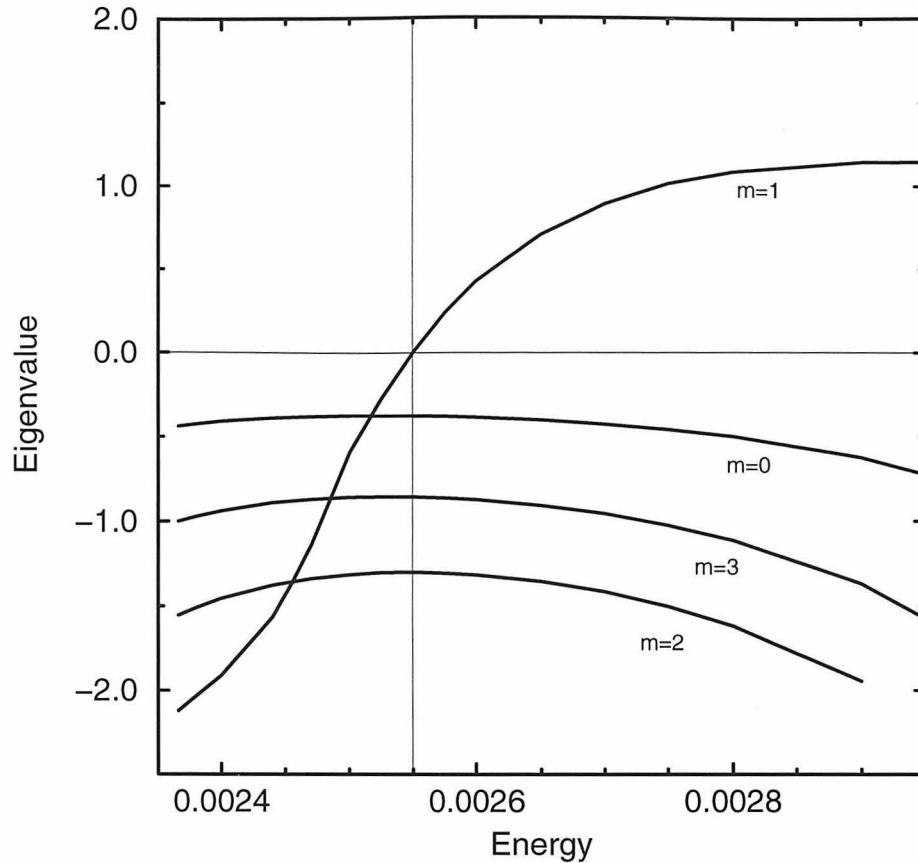


Figure 3.7: Largest eigenvalues for symmetric solutions with $Q = .2$ and $M = .04$. The vertical line indicates the bifurcation energy.

eigenvalues are negative except for $m = 1$ at energies larger than the critical energy from the bifurcation analysis. This agrees with our previous results by predicting that symmetric states are stable below E_c . Above E_c the solution is no longer a local entropy maximum and the unstable eigenvector having $m = 1$ confirms that a bifurcation to an off-center vortex occurs. The $m = 1$ eigenvector at the bifurcation point plotted in Figure 3.8 shows a complete agreement with $\omega_1(r)$ and $\psi_1(r)$ from the bifurcation analysis.

Next we examine the stability of off-center vortices. For the case in Figure 3.4 with a supercritical bifurcation, it is natural to expect that these single vortices are stable. This is exactly the case as shown in the upper part of Figure 3.9 that all eigenvalues

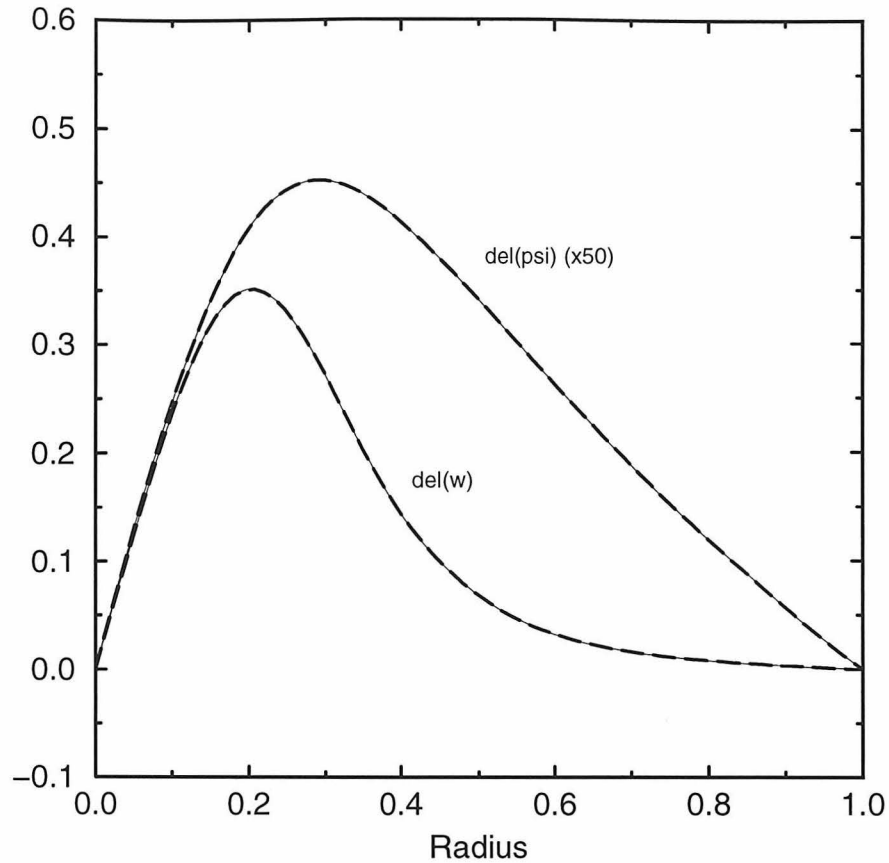


Figure 3.8: $m = 1$ eigenvector (thin solid lines) and bifurcation analysis results (thick dashed lines) at the bifurcation point with $Q = 0.2$ and $M = 0.04$.

are negative and approach zero at E_c for both fixed energy and temperature cases. There is actually a zero eigenvalue not shown in the figure because of the rotational degeneracy. However for $M = .06$ at a fixed temperature, we have shown that the bifurcation is a subcritical and, from the behavior of thermodynamic quantities, the first portion of the off-center branch is unstable (e.g., a negative specific heat.) The solid line in the lower graph of Figure 3.9 with a positive eigenvalue in this region explicitly shows that the states are not free energy maxima. On the other hand when we consider a closed system we have all negative eigenvalues and this again agrees with the bifurcation analysis.

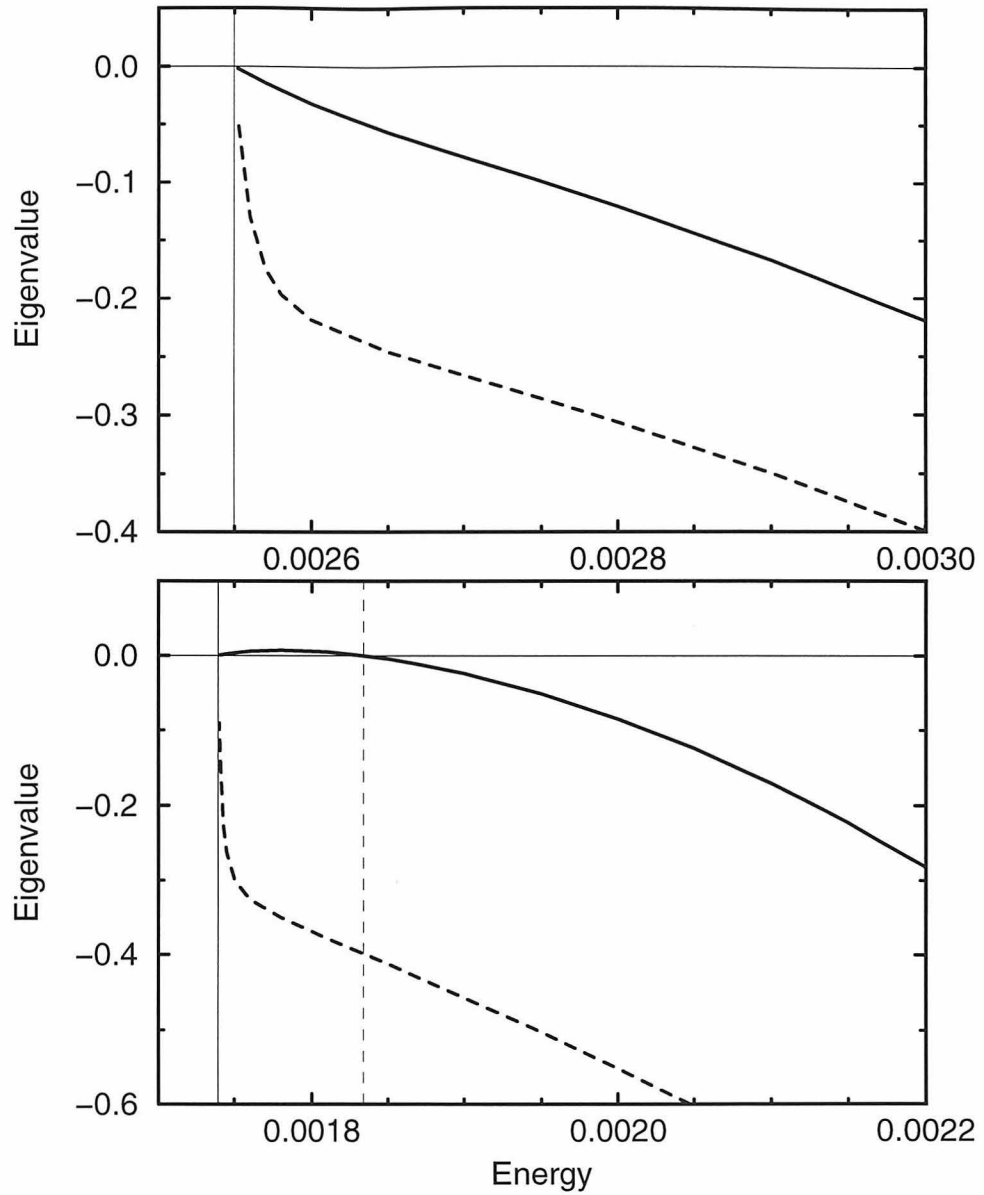


Figure 3.9: Largest eigenvalues for off-center vortex solutions with $Q = 0.2$. M equals to 0.04 and 0.06 for the upper and lower graph respectively. In both graphs, solid lines correspond to fixed β , dashed line fixed E . The vertical solid lines indicate the bifurcation points; the vertical dashed line marks the beginning of the unstable segment calculated from the off-center solutions.

Chapter 4 Double and Multiple Vortex States

4.1 Overview

Many numerical simulations [13, 14, 15, 16, 17, 18] of two-dimensional high-Reynolds-number fluids with random initial conditions have shown that beyond an early stage during which many coherent vortices are formed, the evolution is dominated by merging of like-sign vortices. Similar relaxation processes have also been observed in an experiment on an electron plasma [31]. A turbulence model has been proposed based on a description of vortex merging [21]. Hence many studies have been done on the merging of two identical vortices, as possibly a first step to understanding the evolution of turbulence. In numerical simulations different methods have been used to study the dynamics of two-vortex initial distributions [45, 46, 47, 48, 49, 50]. A pure electron plasma experimental investigation of symmetric vortex merging has also been done [25]. These dynamical studies find that two vortices will remain separated if their initial separation is greater than a critical value and below it they will quickly merge together. Equilibrium calculations for a pair of uniform elliptical vortices [51, 52] are consistent with this picture because no steady-state solutions are found for small vortex separations.

In this chapter we look at the vortex merging problem using the equilibrium theory. Here we want to solve for two-vortex solutions and determine their thermodynamic stability properties. A recent work investigated some two-vortex solutions in a disk [53] but the stability, which is crucial for explaining these states and the mergers observed in experiments and simulations, were not tested. We will separate the stability eigenvectors of a two-vortex solution into those that might be expected to be strongly mixing, and those that are not. In terms of ergodicity this assumes that the phase space is separated into two distinct parts, one being explored by the flow and the other not explored. The justification of this separation comes from the fact

that the nonmixing eigenvectors correspond to collective symmetry motions of the vortex pair (translations and rotation) in the infinite system limit. In a disk we will show that the assumption about their nonmixing nature leads to a prediction of the stability of equilibrium positions at large separations, and this prediction agrees very well with an experimental observation. We then identify the passage of the eigenvalue of a “mixing” eigenvector through zero as indicating vortex merging in the dynamics.

Finally we propose the idea of “vorticity localization” for the statistical theory to solve the difficulty that two-vortex solutions cannot exist in a large system. The basic idea is that for some special configurations, global ergodicity of the whole system will not be achieved and thermal equilibrium is reached in a local region. Observations of stable two-vortex states in experiments and simulations provide evidence for its validity. Vorticity localization will then be generalized to explain stable multiple-vortex states, which are observed recently in an electron plasma experiment [31].

4.2 Mean Field Two-Vortex Solutions in a Disk

Using the iteration method for solving Equation 2.6 in a disk as described in Section 2.5, we can find two-vortex solutions by starting the iteration with an initial distribution with two identical vortices sitting at $\theta = 0$ and $\theta = \pi$ of the polar coordinates. The size and separation of the vortices are chosen to be roughly consistent with the required Q and M . Explicitly enforcing the symmetry about the x and y axes at each iteration is also used to avoid converging to an off-center single vortex due to numerical round-off error.

In Section 3.2 we study the single-vortex states by varying the system energy with fixed total vorticity and angular momentum. Here we use a different approach motivated by past experiments and simulations. In these papers most attention is concentrated on how the dynamics of two similar vortices depends on their initial separation. To put our work in the same context, first we choose a total vorticity Q , which sets the size of vortices, and an entropy S , which roughly sets the vorticity distribution inside the vortices. Then two-vortex mean field solutions with different

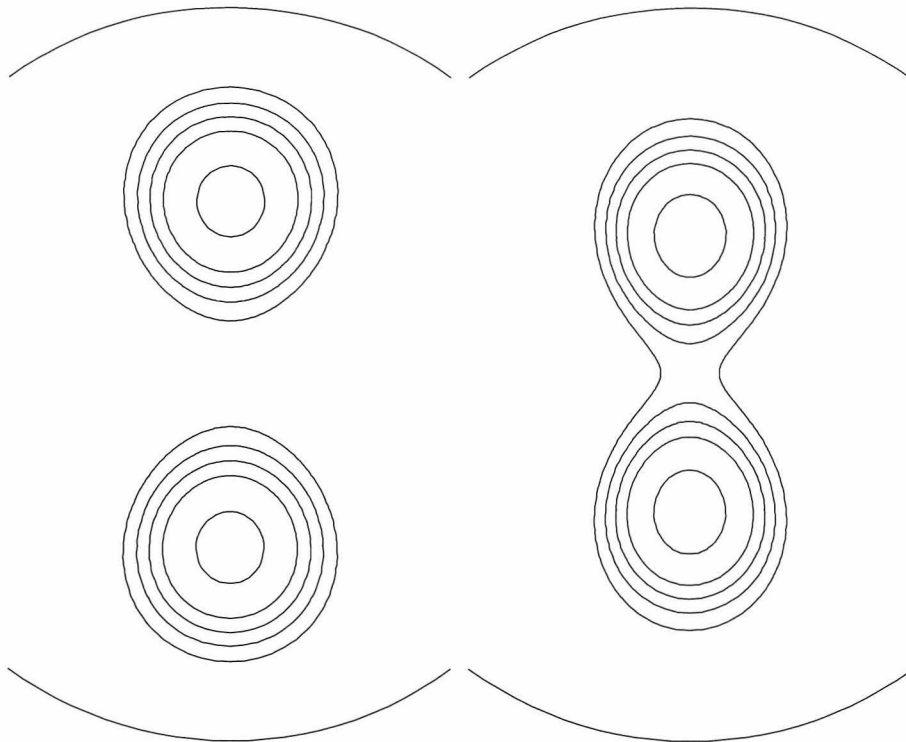


Figure 4.1: Vorticity distributions for $Q = 0.2$ and $S = 0.25$. On the left graph, $M = 0.05$; on the right, $M = 0.0373$. Contour levels are 0.9, 0.347, 0.134, 0.0518, 0.02. (A logarithmic scale.) Arcs indicate the disk boundaries.

separations are calculated by varying the angular momentum M .

Two typical two-vortex solutions are plotted in Figure 4.1 with $Q = 0.2$ and $S = 0.25$. Indeed they have very similar vortex sizes and internal distributions. On the left the angular momentum equals to 0.05 and the two vortices are well separated. The ratio between vortex separation and average vortex diameter is about 2.24. The vortex radius is defined as,

$$R_v \equiv \frac{3}{2} \int r \omega_0(\mathbf{r}) d\mathbf{r} / \int \omega_0(\mathbf{r}) d\mathbf{r},$$

with the origin at the center of the vortex and integration over the range of the vortex. For a uniform circular vortex, R_v will equal the radius. In the dynamics the vortices will rotate around the disk center by a rigid body motion with an angular frequency

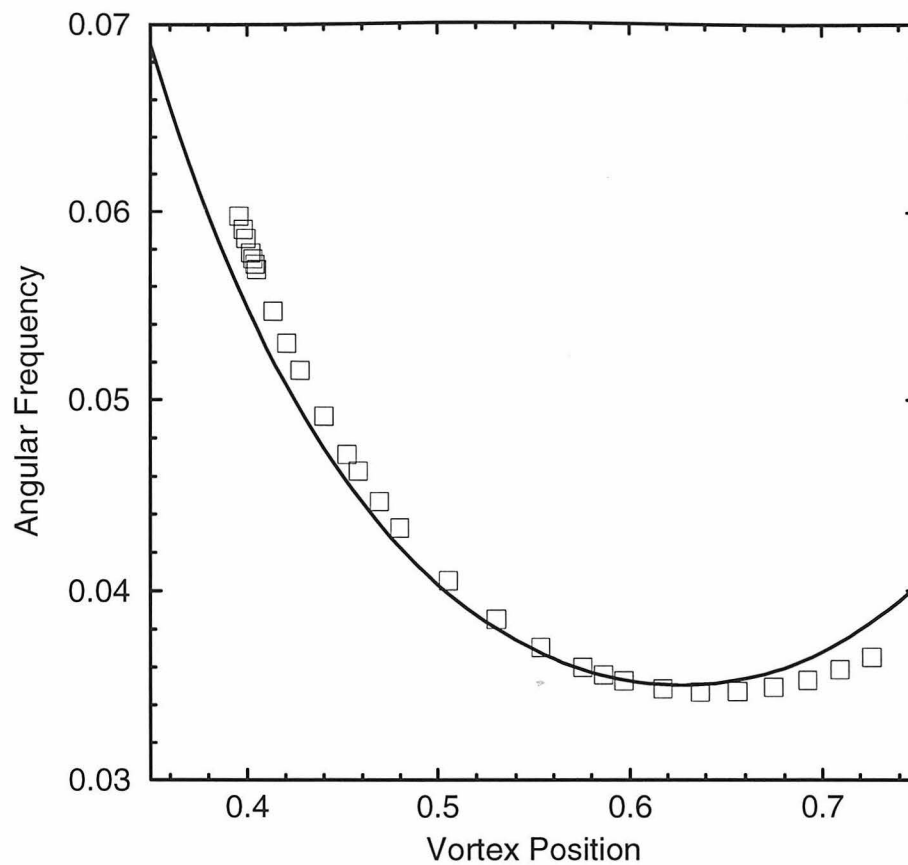


Figure 4.2: Angular frequency for two-vortex solutions with $Q = 0.2$ and $S = 0.25$ (the squares) and two point vortices each with strength $\Gamma = 0.1$ (the solid line).

2Ω . This can be seen considering the equilibrium vorticity as a function of $\psi(\mathbf{r}) + \Omega r^2$: $\omega(\mathbf{r}) = f(\psi(\mathbf{r}) + \Omega r^2)$. Substitute the expression into the Euler equations,

$$\begin{aligned} \frac{\partial \omega}{\partial t} &= -(\mathbf{v} \cdot \nabla)\omega = -v_r \left(\frac{\partial \psi}{\partial r} + 2\Omega r \right) f' - v_\theta \frac{1}{r} \frac{\partial \psi}{\partial \theta} f' \\ &= -2\Omega \frac{\partial \psi}{\partial \theta} f' = -2\Omega \frac{\partial \omega}{\partial \theta}. \end{aligned} \quad (4.1)$$

In Figure 4.2 we compare with the rotational frequency of two point vortices, which is

$$\frac{\Gamma}{4\pi D^2} \left(1 - \frac{2}{1 + R^2/D^2} - \frac{2}{1 - R^2/D^2} \right),$$

here Γ the strength of the point vortices, D the distance of the vortices to the disk

center, and R the radius of the disk. In the middle range of the vortex position where the vortices are well separated and far from the disk boundary, the frequency from the point vortices gives a good approximation. Large deviations appear when the vortices start to have large distortion from their mutual interaction at small separations and from boundary effects at large separations.

For the right-hand solution in Figure 4.1 the angular momentum is 0.0373 and the separation/diameter ratio is smaller at 1.73. The most significant difference from the larger M case on the left is that higher levels of vorticity contour lines from the two vortices join together to circulate both vortices. (These contours are too low to be shown on the left.) This means that more vorticity is in the exchange band which encompasses the two vortices together. Because the constant contours of $\psi(\mathbf{r}) + \Omega r^2$ coincide with those of $\omega(\mathbf{r})$, in the dynamics the vorticity will move back and forth between the two vortices while the whole distribution is rotating. This structure is observed in the simulations by Melander *et al.* [50] who find that for two vortices with a small initial separation near the merging critical value, an exchange band will develop in the final two-vortex steady state distribution.

The aspect ratio for each individual vortex (measured analogously to the aspect ratio of an ellipse) increases when the vortices get closer as we can see in Figure 4.1. This is reasonable due to the stronger vortex interaction. A similar situation is observed in the calculation of equilibrium elliptical two-vortex patches done by Saffman and Szeto [52].

When the angular momentum is further decreased, two-vortex solutions can no longer be found. More specifically we use a two-vortex solution as the initial guess in the iteration scheme described in Section 2.5 but decrease M by a small amount to find another solution with a smaller separation. In this way we can find a series of two-vortex solutions with smaller and smaller separations. But after a critical angular momentum (and hence a critical separation), the iteration suddenly converges to a symmetric single-vortex state, even if a very small decrease is taken in the angular momentum. This situation strongly suggests the existence of a critical separation such that there are no two-vortex mean field solutions below it. For the case in

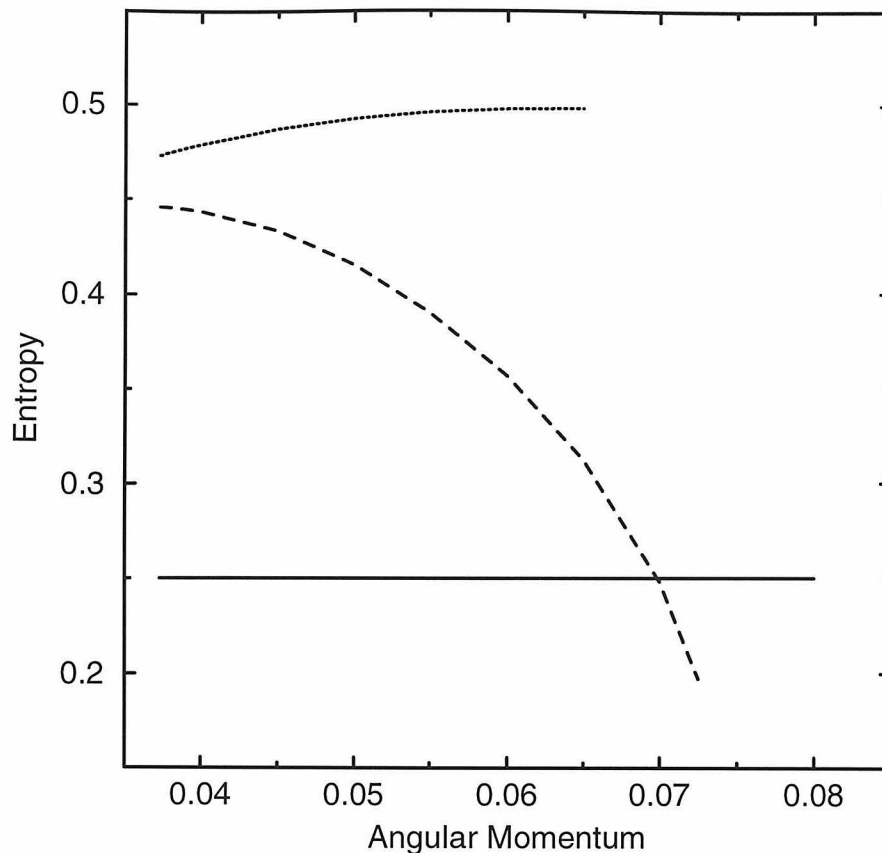


Figure 4.3: Entropies for states with $Q = 0.2$. Solid: two-vortex reference states. Dashed (symmetric vortex) and dotted (off-center vortex) lines have the same $E(M)$ as the solid line.

Figure 4.1 with $Q = 0.2$ and $S = 0.25$, the critical ratio is about 1.73 which is consistent with the values obtained by many dynamical studies of experiments and simulations [45, 46, 47, 48, 49, 50, 25, 51, 52]. Of course it is also possible that two-vortex solutions still exist below the critical ratio but the iteration method fails to find them. This question can be resolved by examining the thermodynamic stability which will be described in the next section.

In Figure 4.3 we compare the entropy of the two-vortex states with those of the symmetric and off-center vortices. Two-vortex states with fixed Q and S (varying M) are plotted as the solid line. For each of these solutions, the corresponding symmetric and off-center single-vortex states at the same energy are plotted as the

dashed and dotted lines respectively. The solid line starts from the minimum angular momentum mentioned above and ends on the right due to the finite size of the disk. Compared with symmetric vortices, two-vortex states have higher entropy at large M , but the entropy becomes lower as M decreases, i.e., the symmetric vortex is the thermodynamically more probable state at a small angular momentum. This is reasonable because at a large M , a symmetric solution will have a large amount of vorticity spreading over a large area near the boundary. At a small M , most vorticity of the symmetric vortex can stay together at the center as opposed to two separated regions in the two-vortex solutions. On the other hand off-center vortices always have the largest entropy when they exist. We suspect that they are absolute entropy maxima for this system.

4.3 Thermodynamic Stability

4.3.1 Separation of Eigenmodes

As discussed in the previous section, we cannot find two-vortex solutions for small values of angular momentum. The way to distinguish whether this is a true physical phenomenon or just a breakdown of the solution finding algorithm is to look at the thermodynamic stability of these solutions. Another question that may also be answered is why two-vortex states are observed to be stable above the critical separation even when single-vortex states have a larger entropy.

We apply the constant energy method described in Section 2.7 to the two-vortex solutions. Again the Fourier-Chebyshev expansion in Equation 3.1 is used. Because in the solutions the two vortices are identical and sit at $\theta = 0$ and $\theta = \pi$ (i.e., $\omega_0(\mathbf{r})$ is symmetric to both x and y axes), the expansion coefficients of $\omega_0(\mathbf{r})$ and $\psi_0(\mathbf{r})$ are nonzero only for even m modes and are all real. When these $\omega_0(\mathbf{r})$ and $\psi_0(\mathbf{r})$ are put into Equation 2.14 to calculate the entropy matrix S_{ij} in Equation 2.15, the matrix elements are divided into four decoupled subspaces: even-real(cosine), even-imaginary(sine), odd-real(cosine), and odd-imaginary(sine) modes. These four

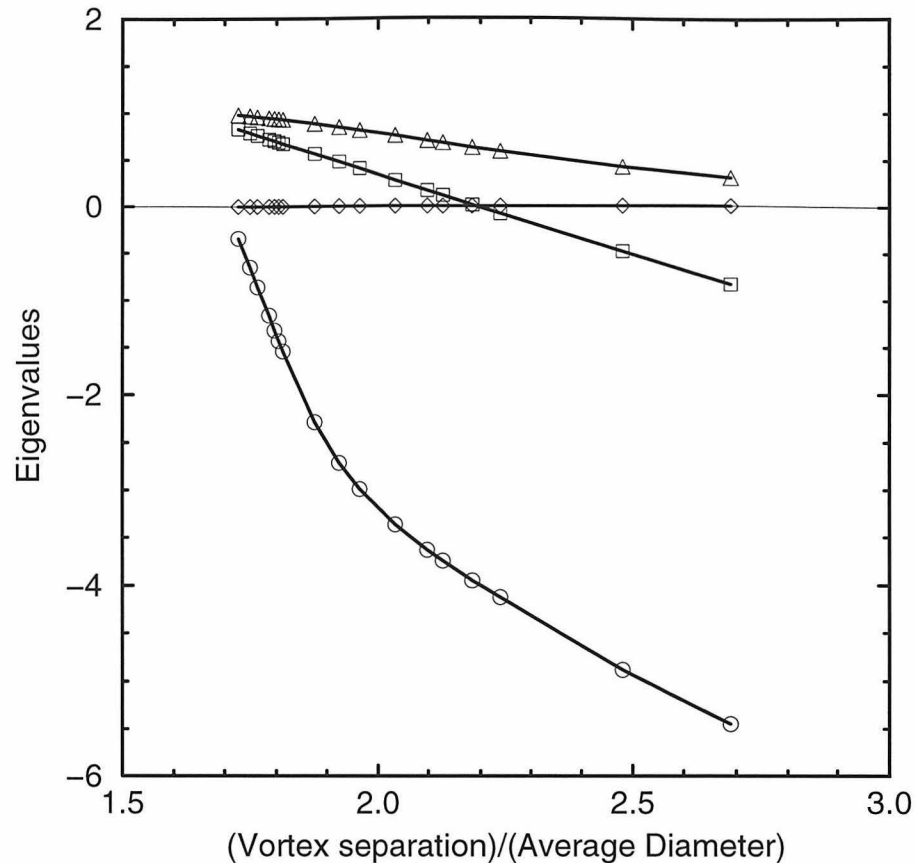


Figure 4.4: Largest eigenvalues for different modes. Circle: even-real mode; diamond: even-imaginary; square: odd-real; triangle: odd-imaginary.

subspaces will have their own eigenvalues and eigenvectors. This also greatly reduces the computation time and demand on computer memory due to a factor of four reduction on the linear size of the matrix.

4.3.2 Nonmixing Eigenmodes

For the series of two-vortex solutions shown as the solid line in Figure 4.3, the largest eigenvalue of each of the four subspaces are plotted in Figure 4.4. Of these four separate modes we will show that three of them (even-imaginary, odd-real, and odd-imaginary) are essentially nonmixing modes. The even-imaginary mode is straightforward because the mode just produces a rotation about the center of the disk. Due

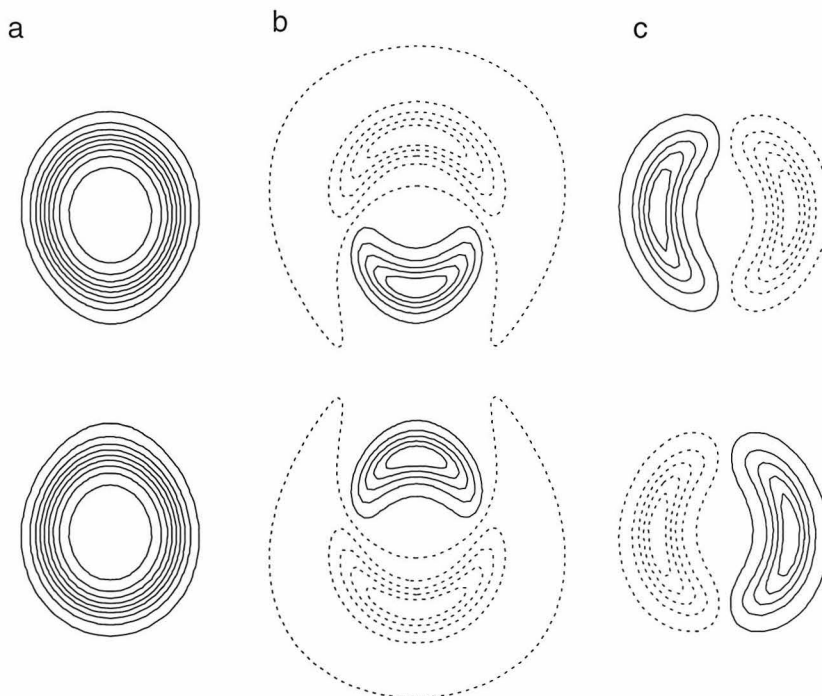


Figure 4.5: (a) Vorticity distribution for $Q = 0.2$, $S = 0.25$, and $M = 0.0373$. (b) Eigenvector for the even-real mode. (c) Eigenvector for the even-imaginary mode. For (a) the nine contours start from 0.1 to 0.9 with 0.1 increment. For (b) and (c) the ten contour levels are equally spaced with dotted lines for negative values. (The absolute amplitude is arbitrary.)

to the rotational symmetry, the eigenvalues should always be zero. The diamonds in Figure 4.4 are indeed all zero and the eigenvector shown in Figure 4.5c does represent a small angle rotation. We will now show that, under the assumption of nonmixing, the prediction from the odd modes regarding the dynamics of two vortices at a large separation agrees well with the dynamics observed in an experiment [26]. Thus we can assume that the odd modes are nonmixing or at most weakly mixing. This leaves the even-real mode as the only strongly mixing mode and the only mode related to the merging of two vortices at a small separation where vorticity mixing is essential.

The odd-real and odd-imaginary modes correspond to collective translational motions of the two vortices, along and perpendicular to the line joining the vortices (referred as the x axis hereafter) respectively, a first hint of their nonmixing nature.

In an infinite space their eigenvalues will be zero. In a finite disk, the odd-imaginary mode moves the vortices closer by reducing their azimuthal separation with the corresponding eigenvalues (the triangles in Figure 4.4) always positive. This is not surprising since this motion is in the direction to form a single off-center vortex which has a larger entropy (see Figure 4.3). The odd-real modes (the squares) have weakly positive eigenvalues at small M , and as M increasing the eigenvalues decrease and then become negative. This can be understood because the vortices then sit closer to the boundary and feel its repulsive influence more.

The odd-real and odd-imaginary modes are closely related to the stability of two-vortex states at a large separation in a disk. This stability has been studied experimentally in a pure electron plasma in a cylinder by Mitchel *et al.* [26]. Their observation shows that two identical vortices in a disk are stable below a separation $D/R = 0.46$, (D gives the positions of the vortices and R the size of the disk) but larger than the merging critical separation which depends on the vortex size, and unstable above it. If the vortices are displaced from their equilibrium positions, they will rotate around the equilibrium points in the stable case or the displacement will exponentially grow in the unstable case. Also their observation gives a good agreement with the analytic prediction from two point vortices.

Now if we suppose the dynamics is nonmixing, the entropy will be a constant. Since the odd-real mode gives a displacement in x axis and the odd-imaginary mode in y axis, using the eigenvalues calculated in Figure 4.4, the constant entropy paths on the $x - y$ plane can be plotted, as shown in Figure 4.6. At the smaller vortex separation, both eigenvalues are positive and the constant entropy contours are closed ellipses. For the larger separation, the odd-real eigenvalue becomes negative and the fixed entropy lines become hyperbolic. Thus the eigenmodes predict the nonmixing dynamics as

$$\begin{aligned}
 \text{elliptical:} & \quad A \cos(\lambda t)(\text{odd-real}) + B \sin(\lambda t)(\text{odd-imaginary}) \\
 \text{hyperbolic:} & \quad Ae^{\lambda t}(\text{odd-real}) + Be^{\lambda t}(\text{odd-imaginary}),
 \end{aligned} \tag{4.2}$$

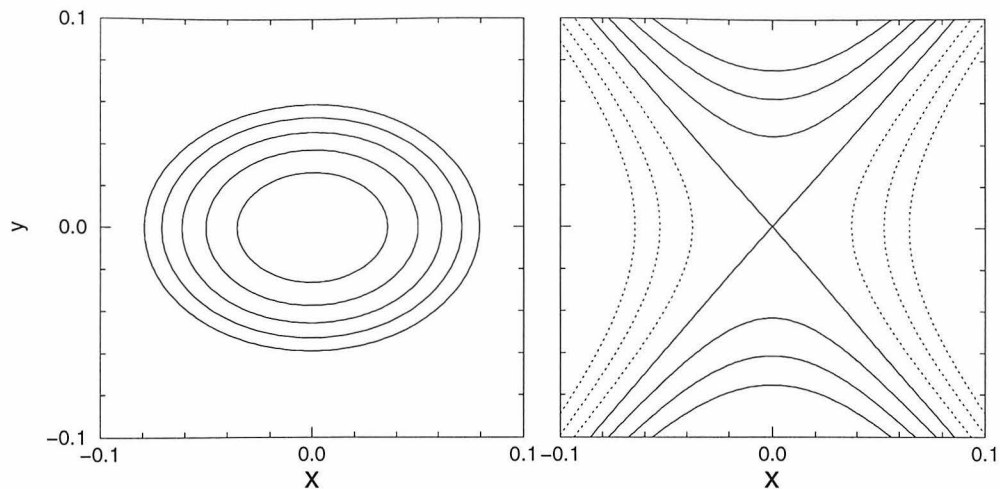


Figure 4.6: Constant entropy contours for odd modes with $Q = 0.2$, $S = 0.25$. $M = 0.04$ ($D = 0.421$) at left and $M = 0.06$ ($D = 0.530$) at right. x and y axes measure the displacement of the vortex from their equilibrium positions in the direction parallel and perpendicular to the line connecting the two vortices respectively. The entropy equals the equilibrium value at the origin and the contour interval is 0.001. Solid lines have higher entropy and dotted lines lower.

with A/B determined by the eigenvalues. Now compared with the results of the electron plasma experiment, Equations 4.2 give correctly the oscillatory and divergent motions observed in the experiment. The switching from elliptical to hyperbolic at $D/R = 0.47$ (the point with zero odd-real eigenvalue) agrees well with the observed switching from stable to unstable at $D/R = 0.46$. From this agreement we can conclude that the odd modes are nonmixing. The ratio between maximum displacements in y and x axes can also be calculated and are shown in Figures 4.7. These ratios shown as circles agree with the solid line from the analytic results of two point vortices, with which the experimental results are consistent. Unfortunately there are no good measurements of these data in the experiment.

4.3.3 Mixing Eigenmode and Merging Critical Ratio

The last eigenmode is the even-real mode which is the mode relevant to the vortex merging at small separations. The eigenvalues, shown in Figure 4.4 as the circles, are

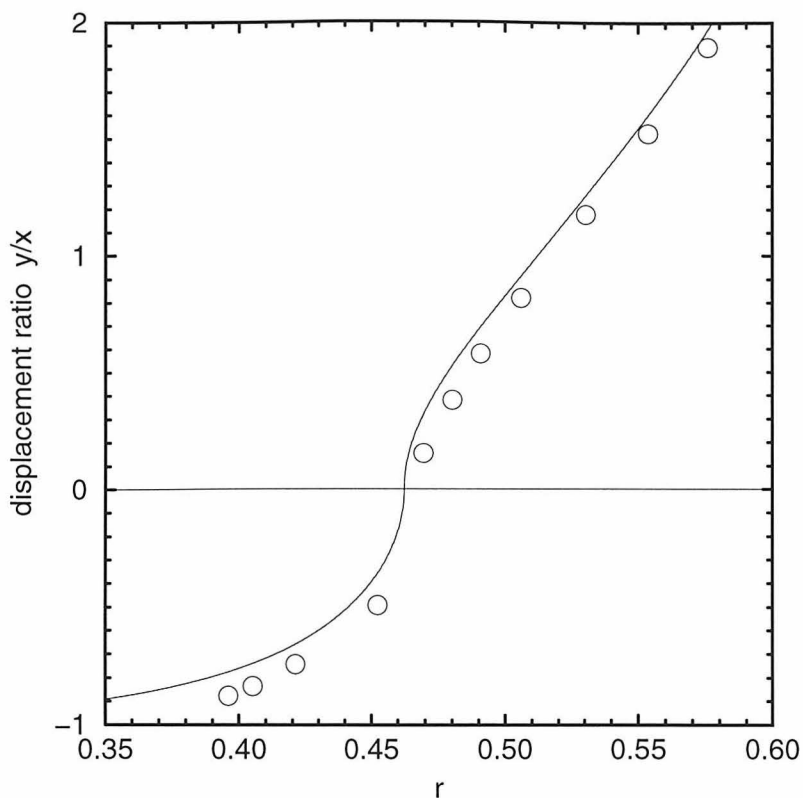


Figure 4.7: Ratio between displacements in y and x axes. The symbols are calculated from the odd eigenvalues. The solid line from the calculation of two point vortices.

all negative indicating that the two-vortex solutions we found are all local maxima on the entropy surface restricted to the mixing even-real modes. Thus although the single-vortex states have higher entropy than the two-vortex states (see Figure 4.3), these states are local maxima in this subspace and we expect that they are stable as observed in experiments and simulations. The even-real eigenvector of the left-most point in Figure 4.4 is plotted in Figure 4.5b which shows a symmetric deformation of the two vortices in the direction producing a vortex merger. We estimate the critical merging separation by extrapolating the circles in Figure 4.4 to zero. This is the point where the two-vortex solutions switch from a local maximum to a saddle point and become thermodynamically unstable. In the particular case of Figure 4.4 the critical ratio (separation divided by average vortex diameter) is about 1.7, which lies in the range of values obtained by previous dynamical studies [45, 46, 47, 48, 49, 50, 50, 25,

51, 52].

This result also partly explains why we cannot find two-vortex solutions below the critical separation. For some reason, the iteration scheme in Section 2.5 seems to converge to a thermodynamically stable state, although it has no clear connection to the dynamics.

The critical separation for the merging scales linearly with vortex size (manifested as a constant critical ratio). This is observed in experiments and simulations and is a consequence of the scaling of the Euler equations which leaves the dynamics unchanged:

$$\begin{aligned} \mathbf{r} &\longrightarrow \lambda \mathbf{r} \\ \omega(\mathbf{r}) &\longrightarrow \omega(\lambda \mathbf{r}) \\ \psi(\mathbf{r}) &\longrightarrow \lambda^2 \psi(\lambda \mathbf{r}), \end{aligned}$$

with λ an arbitrary positive constant. This scaling also applies to the mean field equations, Equation 2.6, with the following additional relations:

$$\begin{aligned} q &\longrightarrow q \\ Q &\longrightarrow \lambda^2 Q \\ M &\longrightarrow \lambda^4 M \\ \beta &\longrightarrow (1/\lambda^2)\beta \\ \Omega &\longrightarrow \Omega \\ \mu &\longrightarrow \lambda^2 \mu. \end{aligned}$$

So the critical separation should also scale linearly with vortex size for mean field solutions.

One problem is that this scaling also requires that the system boundary scales with λ or that the system is infinite. This is usually not the case in experiments and simulations where a fixed system size is used for various vortex sizes. The fact that

the critical ratio is roughly a constant in these studies suggests that the boundary plays a minimal role in the vortex merging process. At a first glance the roughly 10% variation for different vortex sizes in our calculation of the critical ratio from the thermodynamic instability is also consistent with these results. However to get a complete picture, the concept of “vorticity localization” must be used; this will be discussed next.

4.4 Vorticity Localization

4.4.1 Two-Vortex State in a Large System

To illustrate vorticity localization we consider the simplest case, namely a two-vortex distribution in free space. To simulate the situation we construct a vorticity distribution by putting two circular vortices in a large disk with a separation larger than the merging critical value. The effect of the boundary on the vortices should be negligible if the ratio R/D is large enough, here again R is the disk radius and D the vortex distance to the center. The two vortices will rotate around the disk center with an angular frequency 2Ω which is well approximated by the frequency computed from two point vortices. (See Section 4.2.) Of course the vortex shape of a two-vortex equilibrium will not be circular but the distortion will not affect the following discussion. With this vorticity distribution, $\omega(\mathbf{r})$, the stream function $\psi(\mathbf{r})$ can quickly be calculated. Because the vortices are rotating with an angular frequency 2Ω , we will look at the corotating stream function defined as $\psi(\mathbf{r}) + \Omega r^2$, which is the stream function in the rotating frame with frequency 2Ω .

In Figure 4.8 contours of $\omega(\mathbf{r})$ and $\psi(\mathbf{r}) + \Omega r^2$ are plotted with R/D about 5. The first thing to notice is that the contours of $\psi(\mathbf{r}) + \Omega r^2$ near the positions of the vortices are not exact circles due to the vortex interaction. In the final equilibrium, the vortex shapes will deform such that contours from $\omega(\mathbf{r})$ and $\psi(\mathbf{r}) + \Omega r^2$ coincide, but we expect that the overall structure of $\omega(\mathbf{r})$ and $\psi(\mathbf{r}) + \Omega r^2$ will be unchanged. Next we see that each vortex is completely enclosed by separated, closed, corotating

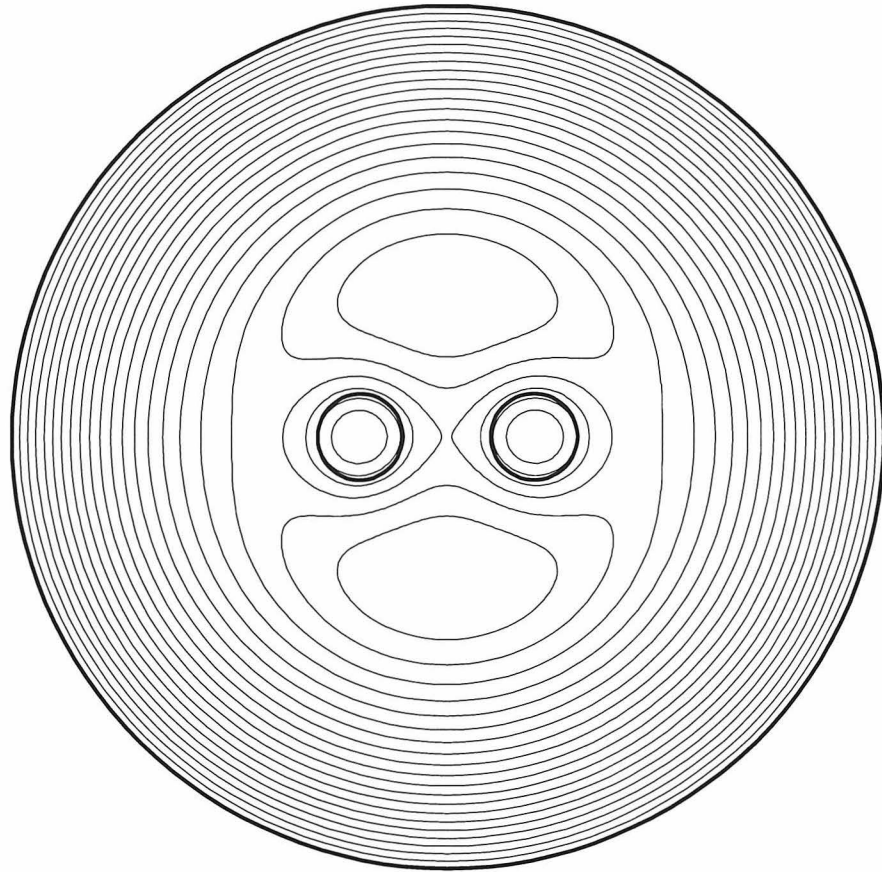


Figure 4.8: Contours of the vorticity (thick lines) and corotating stream function (thin lines) for two circular vortices in a unit disk. The vortex size and distance from the center are 0.1 and 0.2 respectively.

stream lines. Since in the dynamics the vorticity is following corotating stream lines, a two-vortex final state is expected. Finally in the region outside about three times D , contours of $\psi(\mathbf{r}) + \Omega r^2$ are nearly concentric circles with values increase toward boundary, due to the Ωr^2 term. If the boundary is enlarged, more nearly circular contours will be added but the structure of $\psi(\mathbf{r}) + \Omega r^2$ in the center region will remain the same.

Now the key observation is that although a dynamically stable two-vortex state is expected in Figure 4.8, this kind of structure cannot be a mean field solution, because

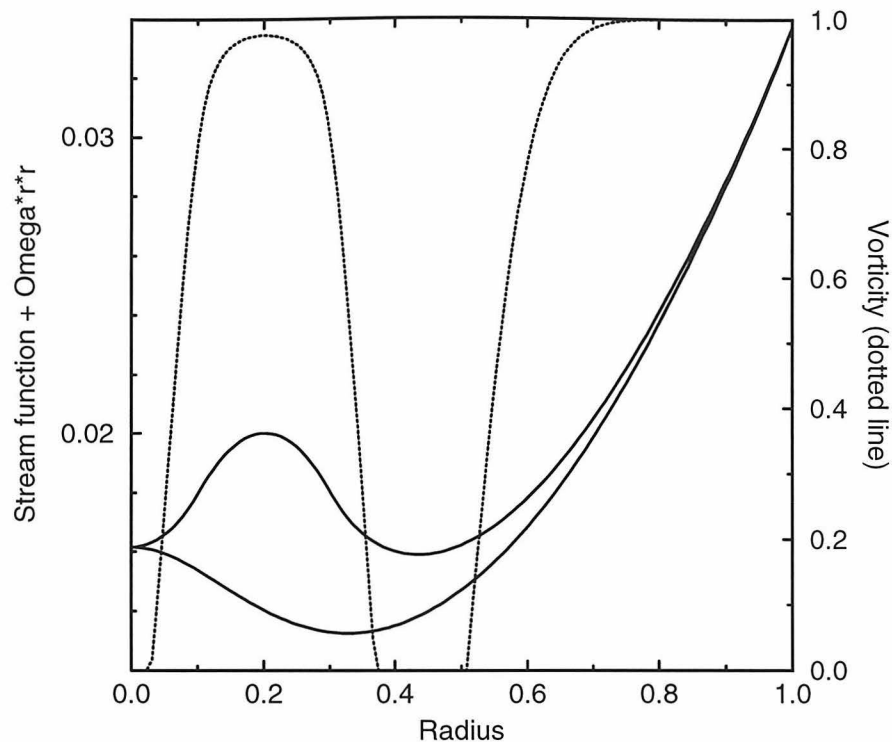


Figure 4.9: Corotating stream function and vorticity field of Figure 4.8. The solid lines are the corotating stream function. Upper and lower lines are along x and y axes respectively. The dotted line is the vorticity field along the x axis.

then $\omega(\mathbf{r})$ must always be a function of $\psi(\mathbf{r}) + \Omega r^2$. In a large disk $\omega(\mathbf{r})$ will increase with $\psi(\mathbf{r}) + \Omega r^2$ toward the disk boundary as we have sketched with the dotted line in the Figure 4.9. Because of the mean field relation, Equation 2.6, between $\omega(\mathbf{r})$ and $\psi(\mathbf{r}) + \Omega r^2$, the vorticity drops to almost zero around the minimum of $\psi(\mathbf{r}) + \Omega r^2$ (at about $r = 0.45$), but will increase again afterward. Hence a ring of vorticity appears at the disk boundary and gets larger with larger disk size. Of course, if the vorticity ring gets too large the structure of the corotating stream function will be completely different. This means that to get a two-vortex solution to the mean field equations, the disk boundary must be somewhere near the minimum of $\psi(\mathbf{r}) + \Omega r^2$ to yield a negligible vorticity ring. This is exactly the situation employed in previous sections.

4.4.2 Vorticity Localization in Mean Field Solution

In the previous section we found that two-vortex mean field solutions only exist for not too large disks. However in a real physical system there seems to be no such restriction as evident in many experiments and simulations. We believe the explanation comes from the property of an ideal fluid that dynamically vorticity can only flow from one place to another but cannot suddenly appear at an isolated region. In Figure 4.8 vorticity is completely enclosed by local corotating stream lines and the minimum of $\psi(\mathbf{r}) + \Omega r^2$ forms a barrier around each vortex which prevents vorticity from moving across. In terms of statistical mechanics, it is unfavorable entropically for vorticity to move through the minimum region, and the vorticity only explores its own neighborhood. In other words the barrier prevents global ergodicity but local ergodicity allows thermal equilibria to be reached in separated regions. In the final state $\omega(\mathbf{r})$ and $\psi(\mathbf{r}) + \Omega r^2$ will follow the mean field relation only inside the minimum and $\omega(\mathbf{r})$ will be zero outside.

One requirement for this localization of vorticity to be a good approximation is that the minimum value of $\psi(\mathbf{r}) + \Omega r^2$ should give a very small value of ω in the mean field equations. In our examples of two-vortex solutions in the two-level initial vorticity case, this value was less than 10^{-3} . The value will never be exactly zero but a small value is good enough in practice due to, e.g., the presence of the viscosity in the real physical systems or the consideration of time scales.

Therefore we propose that in this kind of situation vorticity will be localized and statistical equilibrium is only achieved locally. We may call this a “local” mean field solution. One of the immediate consequences of this construction is that the size of the boundary only has minimal effect on the two-vortex mean field states, as observed in experiments and simulations. Another interesting consequence is that the two vortices need not to be identical, since the two vortices may “live” in separate regions following their own mean field relations. For example the inverse temperatures of the vortices can be different yielding different internal vorticity distributions, or the total vorticity of each vortex can be different yielding an equilibrium state with uneven

vortex sizes. In Figure 4.10 we plot two examples of these particular situations. It will be interesting to see the observation of these states in future experiments or simulations.

We also note here that so far two-vortex solutions are always found in a disk. Actually a disk is necessary because other boundaries are not consistent with the Ωr^2 term. This of course is due to the fact that angular momentum is only conserved in a disk (or an annulus). However by using vorticity localization, two-vortex rotating solutions (i.e., with the Ωr^2 term) can be found in any sufficient large asymmetric system. Of course the asymmetry of the boundary will make the distribution vary at different two-vortex orientations. Nevertheless vorticity localization ensures that this variation is minimal in a large system and we can have nearly steady rotating two-vortex states. One example in this situation is the numerical simulation done in a square with periodic boundary conditions [50].

4.4.3 Multiple-Vortex Solution

The concept of vorticity localization can be used for distributions with more than two vortices. Two examples of “local” multiple-vortex solutions with three or four vortices are shown in Figure 4.11. Again we see that the corotating stream function (the dotted lines) is closed around every vortex, the requirement for vorticity localization and a local thermal equilibrium.

We note here how these solutions with vorticity localization are calculated numerically. Basically we still follow the iterative scheme described in Section 2.5, but with two modifications. The first is that at each iteration step when $\omega_t(\mathbf{r})$ is calculated from $\psi_t(\mathbf{r})$, $\omega_t(\mathbf{r})$ at locations outside the minimum of the corotating stream function are set to zero. The second is that each vortex region has its own parameters (β, Ω, μ) to satisfy its own conserved quantities (Q, M, E) . However the angular momenta are not all arbitrary. They must give a single Ω for every vortex in order to have a steady rotating state.

Fine *et al.* [31] have done an electron plasma experiment studying final equilib-

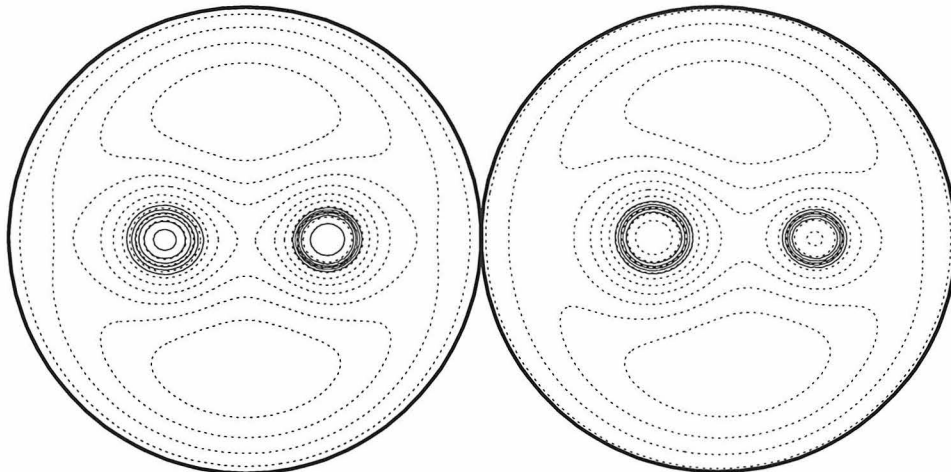


Figure 4.10: Examples of asymmetric “local” two-vortex solutions. On the left: two vortices with the same Q but different β . On the right: two vortices with different Q but the same β . Solid lines show the vorticity field and dotted lines show the corotating stream function. The levels for both contour lines are equally spaced between the maximum and minimum values.

rium states from an initial distribution with unstable vortex filaments. They observe the formation of different stable multiple-vortex final states under some conditions. Figure 6 in the paper shows some regular vortex patterns with vortex numbers ranging between three and nine. Although the transition from the initial distributions to the multiple-vortex states is still not well understood (e.g., the interaction between the coherent vortices and the small background vorticity field may play some role), we believe these final states can be explained by the “local” mean field solutions with vorticity localization. For example, we put six or seven circular vortices in a disk, arranged similarly to the vortex patterns of the third and fifth graphs in Figure 6 of the paper, and calculate their corotating stream functions. The results are plotted in Figure 4.12. We see that all the circular vortices are again encircled by the corotating stream lines as in Figure 4.11, therefore by using vorticity localization, similar “local” mean field solutions will be found.

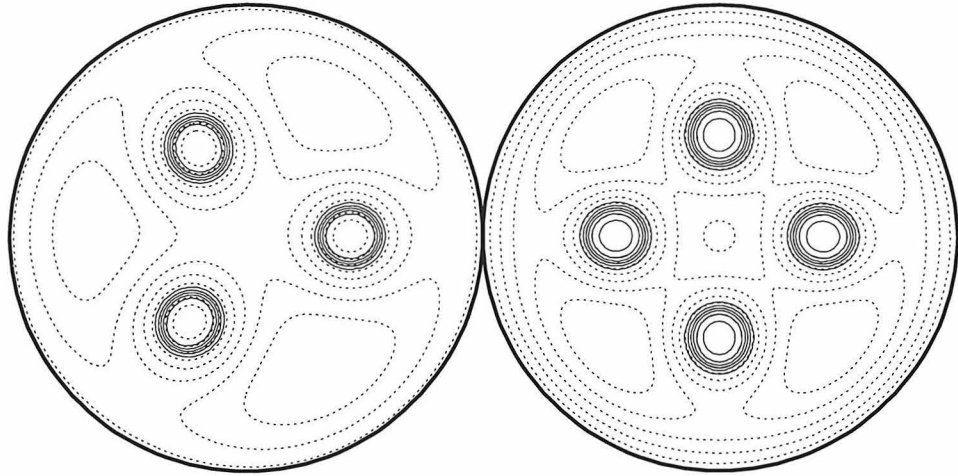


Figure 4.11: Examples of “local” mean field solutions with three and four identical vortices. Solid lines: the vorticity field, and dotted lines: the corotating stream function. The levels for both contour lines are equally spaced between the maximum and minimum values.

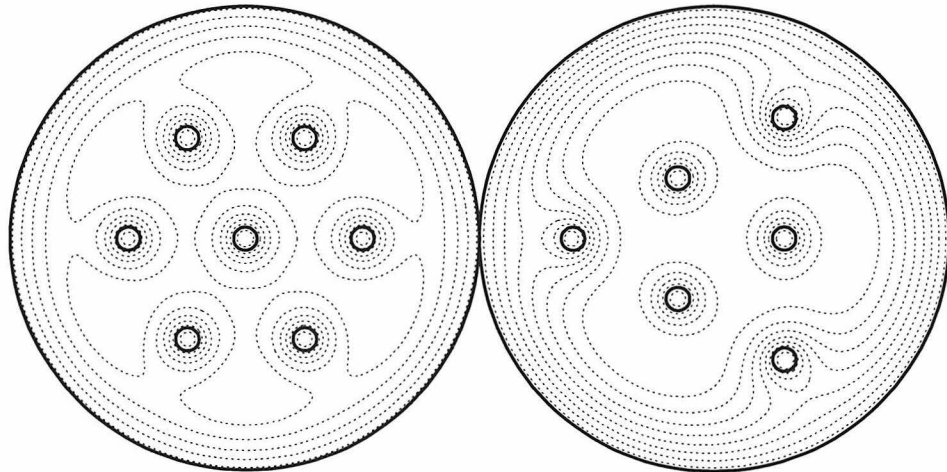


Figure 4.12: The corotating stream lines (dotted line) of six or seven circular vortex (solid line) patterns. The contour levels of dotted lines are equally spaced between the maximum and minimum values.

Chapter 5 Vortex Formation in an Annulus

5.1 Overview

In this chapter we investigate mean field solutions in an annulus, concentrating especially on symmetric vortex layer and single coherent vortex solutions. This geometry is relevant to the upper layer of planetary atmospheres. On an outer planet this surface layer usually has a shear band structure and there are stable vortices at particular locations in this stratified zonal flow, with the Jupiter's Great Red Spot as the best known example. As discussed in Chapter 1, many models of Jupiter's atmosphere have shown that the deeper, steady shear flow below will induce and support stable vortices on the upper layer. Numerical simulations [9, 11] done by Marcus in an annulus show that the shear applied by a background steady flow is the dominant factor in the formation of single coherent vortices. Thus, using the mean field solutions in an annulus, we want to study the relation between the symmetric and single-vortex states, and the effect of a background shear.

In the following sections, we first discuss the conserved inner circulation which plays the important role of providing a background shear. We begin with a discussion of the axisymmetric solutions and their dependence on system parameters. Next, the bifurcation analysis described in Section 2.6 is used to find the bifurcation to single-vortex solutions. The effect of the inner circulation, and hence the background shear, on the bifurcation is investigated. Finally, two-dimensional single-vortex solutions are found and with them we not only confirm the results of the bifurcation analysis but also identify the discontinuous transitions from the symmetric to single-vortex states when no bifurcations are present. With these calculations a complete picture in the parameter space, especially the inner circulation, concerning the formation of coherent vortices will be established.

5.2 Inner Circulation and Background Shear

Before discussing the mean field solutions in an annulus, we need first to consider the special property of an annulus coming from the fact that it is not a simply connected region. From the conservation law, Equation 2.2, the circulation C on any boundary, defined as

$$\oint_{\text{boundary}} \mathbf{u} \cdot d\mathbf{l} \equiv 2\pi C$$

is conserved dynamically. For a system with a single boundary, e.g., a disk, conservation of the circulation is trivial because it always equals $Q/(2\pi)$. However for an annulus the circulations C and C' on the inner and outer walls are conserved separately. The inner circulation C , which can also be seen as an effective vortex at the center, becomes an additional conserved quantity to be specified by initial conditions and $C' = Q/(2\pi) - C$ is set automatically (or vice versa). This new conserved quantity C does not change the mean field equations but sets a constraint on the boundary conditions. If the stream function $\psi(\mathbf{r})$ on the outer wall is chosen to be zero, $\psi(\mathbf{r})$ on the inner wall will change continuously during the dynamics depending on the vorticity distribution to give a constant value of C . Numerically, when solving for $\psi(\mathbf{r})$ from Poisson's equation with a given $\omega(\mathbf{r})$, we first solve it with the boundary conditions $\psi(r = a) = \psi(r = b) = 0$. Then $A \ln(r/b)$ is added to the solution $\psi(\mathbf{r})$ to obtain the correct C by adjusting A .

The important consequence of a nonzero value of C is that a background shear is produced in the system. To see this, consider an annulus (assuming boundary radii 1 and 2) with zero vorticity but a nonzero C , the stream function and azimuthal velocity become

$$\psi(r) = C \ln(r/2), \quad u_\theta = -C/r.$$

So there is a background shear in the system,

$$\sigma \equiv r \frac{d}{dr} \left(\frac{u_\theta}{r} \right) = \frac{2C}{r^2}.$$

In the numerical simulations [11] the fluid evolves under the influence of a background

shear flow and the final equilibria are found to be strongly dependent on the background shear strength. In our mean field calculations we will study the influence of C , and hence the shear, on the vortex formation and compare with the results from the simulations.

5.3 Axisymmetric Solutions

First we want to consider axisymmetric solutions. We choose the inner and outer radii to be one and two: results are qualitatively similar for different system sizes. The equation for symmetric solutions is Equation 2.7 and the numerical method is discussed in Section 2.5.

Results for $Q = 2$, $M = 4$, and different C are shown in Figure 5.1. The first two rows of Figure 5.1 show the states of the system characterized by the energy, entropy and inverse temperature β . The energies are bounded both above and below. The two limiting energy states correspond to β going to $\pm\infty$, clearly seen in the second row of Figure 5.1. The solutions have a maximum entropy when β is zero, consistent with the thermodynamic relation $\beta = \partial S / \partial E$. The entropy usually goes to zero when β goes to $\pm\infty$, or equivalently when the temperature goes to zero, except when $\beta \rightarrow \infty$ for $C = 0$. This is because in these low and high energy limits the vorticity will saturate at the value q in a finite region of space and then Equation 2.5 will give zero entropy. The vorticity distributions in these limits are shown in the bottom row of Figure 5.1. The distributions can be understood as follows: In (b) and (c) the dominant forces are the interactions between the effective vortex at the center and the vorticity distribution in the annulus. With negative values of β , the interaction is repulsive in (b) and attractive in (c), and the vorticity distributions (dashed lines) become a top hat distribution centred away from the walls in (b) and two distinct regions on the walls in (c). The reason for the two regions in (c) is that the circulation inside attracts vorticity to the inner wall, with the rest sent to the outer wall to conserve angular momentum. With positive values of β , the effects of the interactions change sign and the distributions (solid lines) just reverse

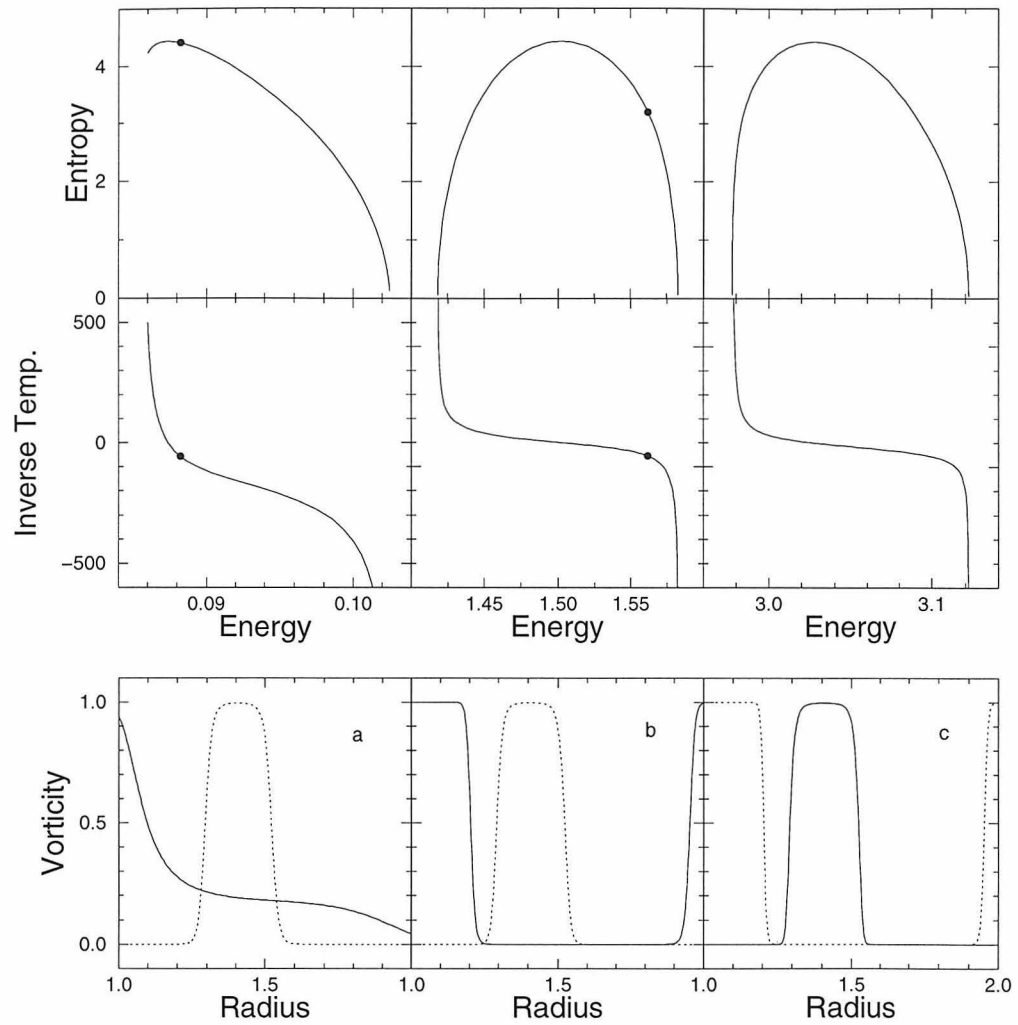


Figure 5.1: Axisymmetric solutions in the annulus with total vorticity $Q = 2$, angular momentum $M = 4$, and initial vorticity level $q = 1$. The three columns are with circulation C equal to 0, 1, and -1 respectively. On the bottom row showing the vorticity distributions, solid lines are for the large positive inverse temperature β ; dashed lines for large negative β . The solid circles are the bifurcation points.

the situation for the dashed lines. In (a) with zero circulation inside, there is only the self-interaction between vorticity. The dashed line distribution comes from the self-attraction of the vorticity at $\beta \rightarrow -\infty$. However at the minimum energy limit ($\beta \rightarrow \infty$), the interesting interplay between conservation of angular momentum and vorticity self-repulsion leads to the particular distribution plotted as the solid line in (a).

5.4 Bifurcation to Coherent Vortex

At high energy (large negative β) the vortex system is likely to form a single coherent vortex instead of a symmetric vortex layer. This has been suggested by a Monte Carlo simulation [3] of the mean field equations. Qualitatively speaking at large negative β the effect of the self-attraction between vorticity is stronger. This self-attraction will eventually break the axisymmetric distribution and a bifurcation will occur. Before solving the single-vortex two-dimensional solutions, we first use the bifurcation analysis described in Section 2.6 to see when it will occur. In particular we want to investigate the effect of the inner circulation C .

For the solutions in Figure 5.1, the bifurcations are plotted as the solid circles. As expected all the bifurcations happen at negative inverse temperatures. Also the bifurcation only occurs when the inner circulation C is one or zero, not minus one. Since C is directly related to the background shear in the system, this suggests a critical shear with a negative value for the bifurcation to a single-vortex state. The complete dependence of the bifurcation point on C is plotted in Figure 5.2. The dotted line marks the maximum possible energy $E_{\max} - E_{\min}$ for the axisymmetric solution. The bifurcation exists for C between two critical values $C_c^{\text{lower}} = -0.2741$ and $C_c^{\text{upper}} = 2.521$. In this region the symmetrical distribution will be unstable to a nonaxisymmetric perturbation if the system energy is larger than that of the bifurcation point. A second bifurcation point also occurs for the C near C_c^{lower} and C_c^{upper} . These lines divide the $E - C$ parameter space into two regions. In the upper region, we have unstable symmetrical solutions and presumably an asymmetrical

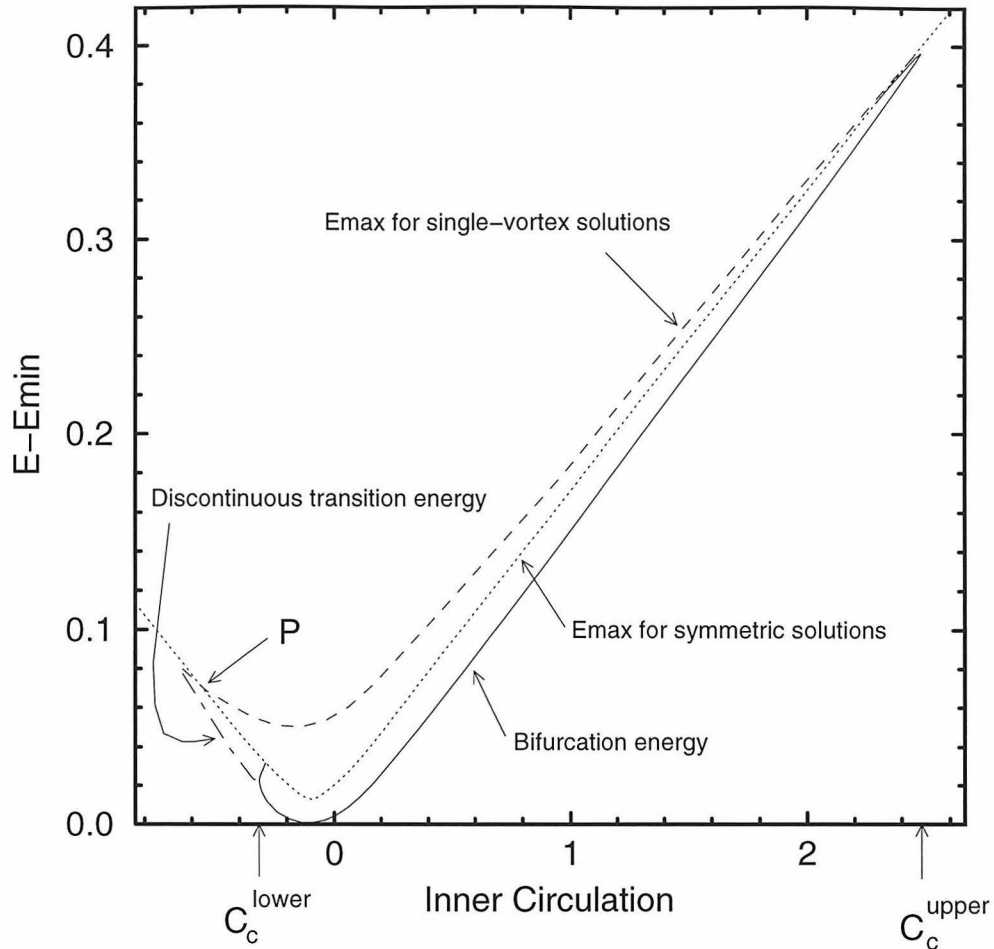


Figure 5.2: Phase diagram for asymmetric solutions. The solid line is the bifurcation line for $m = 1$ mode in the annulus with $Q = 2$, $M = 4$. The dotted and dashed lines are the maximum energy for the axisymmetric and asymmetric solutions respectively. The dot-dashed line is the first order transition point when a bifurcation is not present.

coherent vortex will be the long time state. Qualitatively similar diagrams are found when different values of Q and M are used.

The vorticity distributions at the bifurcation energy for different values of C are plotted in Figure 5.3. The figure shows that for a positive C the symmetric vorticity distribution at the bifurcation is strongly peaked with a peak value growing with C and with a position mostly determined by M . The driving force in the bifurcation may be ascribed to the increased vorticity interaction due to its larger peak value in the asymmetric coherent vortex. As C increases however, the vorticity in the

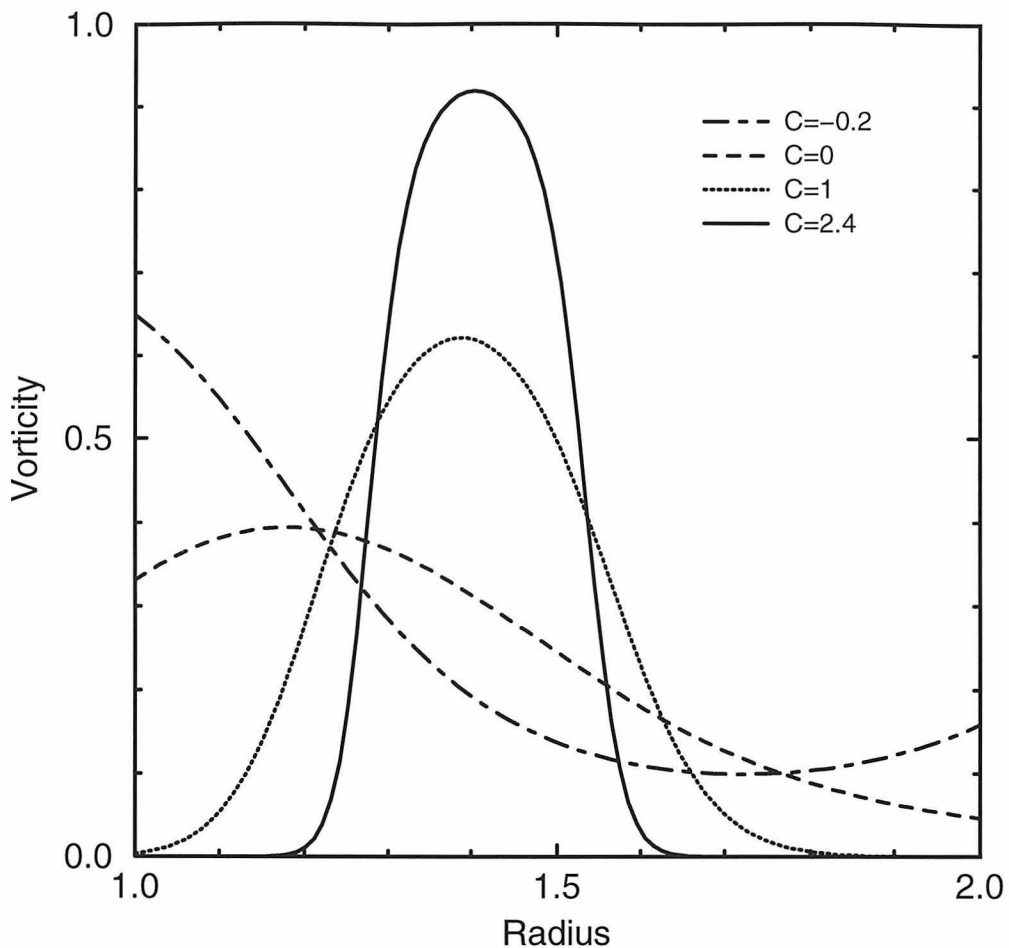


Figure 5.3: Axisymmetric vorticity distributions at the bifurcation for different values of C at $Q = 2$ and $M = 4$.

symmetric ring approaches saturation, so that a maximum value C_c^{upper} for which the bifurcation occurs is to be expected.

5.5 Single-Vortex Solution

We have found that situations exist where a vortex layer will bifurcate to an asymmetric solution. In this section we solve the two-dimensional mean field equation to find these single-vortex solutions and compare with the symmetric solutions and results from the bifurcation analysis. Moreover it is also possible that single-vortex

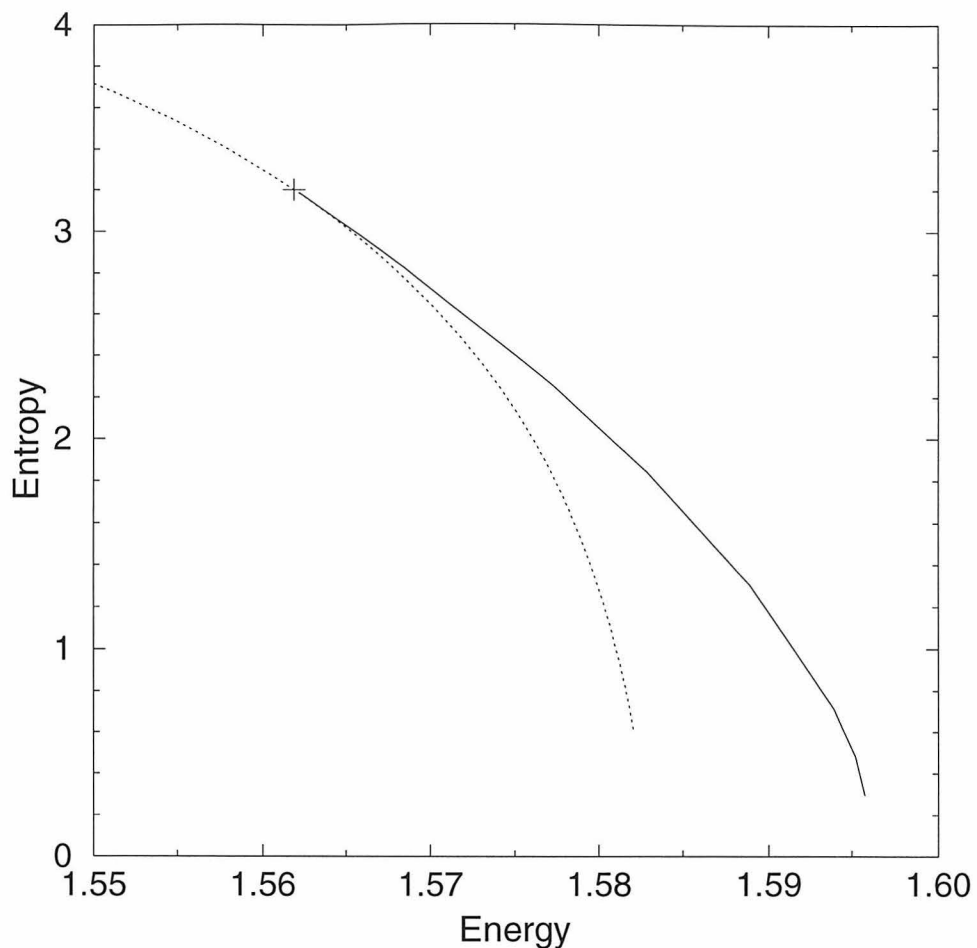


Figure 5.4: Entropy of symmetric (dotted line) and single-vortex (solid line) solutions for $C = 1$, $Q = 2$ and $M = 4$. Cross is the bifurcation point.

solutions exist even when symmetric ones lack bifurcations. In this case a discontinuous transition will occur, a situation somewhat similar to the merging of two vortices discussed in Chapter 4.

Figure 5.2 predicts single-vortex states at high energy for C between C_c^{upper} and C_c^{lower} . These states are indeed found and are plotted in Figure 5.4 showing the entropy-energy relation for $C = 1$. A number of points are worth noticing. Firstly we see that the single-vortex states join perfectly with the symmetric branch at the bifurcation point calculated in previous section. Secondly, this state always has a higher entropy compared to the symmetric state at the same energy. This indicates

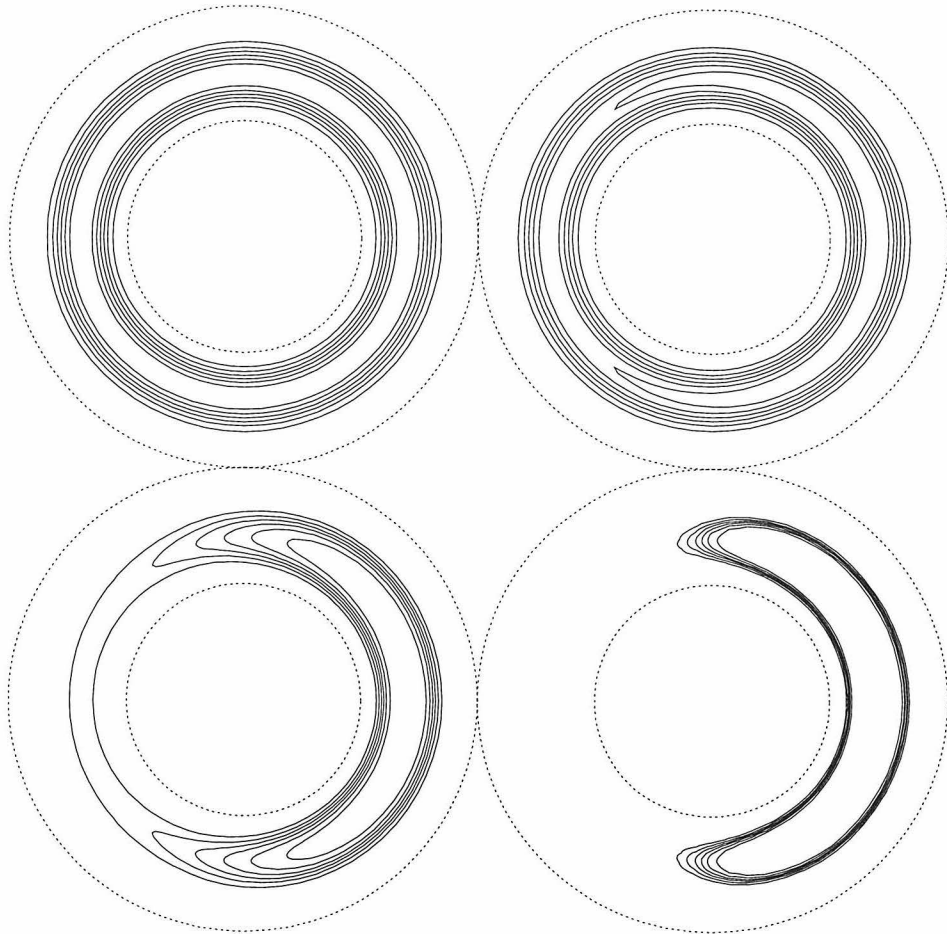


Figure 5.5: Vorticity contours for $C = 1$, $Q = 2$ and $M = 4$. Upper-left: axisymmetric solution at $\beta = -50$. Upper-right: asymmetric solution at $\beta = -55$. Lower-left: $\beta = -70$. Lower-right: $\beta = -150$.

that single vortices are thermodynamically more probable states.

Following the solutions from an axisymmetric state through the bifurcation point onto the asymmetric branch we would expect to see an axisymmetric vortex layer gradually breaking up and finally reaching a single-vortex state. This transition is clearly shown in Figure 5.5 with contour plots of the vorticity distributions for $C = 1$. The final maximum energy ($\beta \rightarrow \infty$) state will be a uniform vorticity patch with its shape strongly depending on the inner circulation C : as the circulation, and hence the positive background shear, increases, the shape becomes more elongated in the azimuthal direction and thinner in the radial direction. This is similar to the increase

of the aspect ratio of an elliptical vortex with increasing shear flow found in analytic solutions [54].

To quantify the asymmetric states we define the average azimuthal angle spanned by a single vortex, s , as

$$s \equiv 4 \int_0^\pi \int_a^b \theta \omega(\mathbf{r}) r dr d\theta / \int_0^\pi \int_a^b \omega(\mathbf{r}) r dr d\theta$$

for a distribution centered at $\theta = 0$. The difference \bar{s} between 2π and s can then be treated as the order parameter of the transition and it is zero for a symmetric vortex layer. If the bifurcation is a forward pitchfork bifurcation, \bar{s} will scale as the square root of $E - E_{\text{bif}}$, with E_{bif} the bifurcation energy. For $C = 1$, \bar{s} plotted as a function of energy in Figure 5.6 clearly shows this scaling behavior. Actually if the bifurcation analysis is expanded to second order as described in Section 2.6, the scaling becomes apparent because \bar{s} is proportional to $\omega_1(r)$ and $E - E_{\text{bif}}$ to $\omega_1(r)^2$ and $\omega_{2,0}(r)$ as,

$$\begin{aligned} \bar{s} &= \frac{16}{Q} \int \omega_1(r) r dr \\ E - E_{\text{bif}} &= 2\pi \int \psi_0(r) \omega_{2,0}(r) r dr + \frac{\pi}{2} \int \psi_1(r) \omega_1(r) r dr. \end{aligned}$$

The results calculated from the above equations are shown as the solid lines in Figure 5.6. For $C = 1$ the solid line agrees perfectly with the single-vortex states (the crosses) at small \bar{s} and the agreement remains quite good even when \bar{s} approaches π . The positive value of $E - E_{\text{bif}}$ found in the bifurcation analysis for $C = 1$ indicates a forward pitchfork bifurcation. However as C is lowered, $E - E_{\text{bif}}$ becomes negative at a particular C , signaling a backward pitchfork bifurcation. Particular examples are shown in Figure 5.6 for C equal to -0.249 and -0.27 . In these situations the traces from the bifurcation calculated at second-order point to the left, and single-vortex states also extend all the way below the bifurcation energy. Presumably the solid line should turn over at a certain energy and connect back to the asymmetric branch. However because we calculate the solutions using a fixed energy scheme, this missing portion of unstable solutions will not be found, since the iteration procedure always

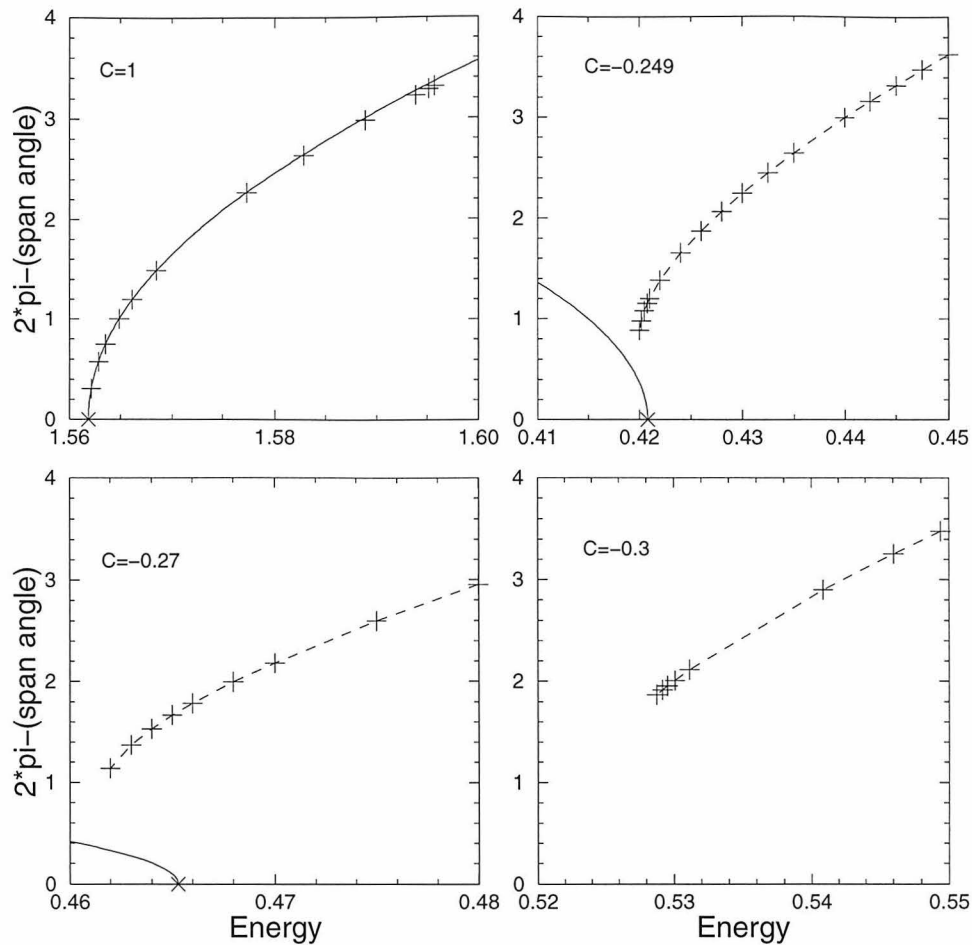


Figure 5.6: \bar{s} dependence on E . \times indicates the bifurcation energy and $+$ the asymmetric solution. Note that the symmetric solutions always have \bar{s} equal to zero. The solid lines are the prediction from the second-order bifurcation analysis. The dashed lines just connect the $+$'s.

favors the stable solution at the same energy.

Thus we find that there exists a particular value of C above which there is a continuous transition from a symmetric vortex layer to a single coherent vortex. Below this value the transition will be discontinuous. For $Q = 2$ and $M = 4$, this value of C is about -0.2 . Actually the discontinuous transition can still exist even without a bifurcation point present for the symmetric solutions, as shown in Figure 5.6 for $C = -0.3$. We estimate the discontinuous transition energy as the minimum energy where single-vortex solutions can be found, i.e., the leftmost point in Figure 5.6 for

$C = -0.3$. This energy is plotted as the dot-dashed line in Figure 5.2 for different values of C .

As C is further decreased, eventually a point will be reached where a coherent single vortex is no longer a thermodynamically more probable state than a symmetric solution. What happens is that the asymmetric branch falls below the symmetric branch in the entropy-energy graph. One way to quickly estimate the point is to compare the maximum energy of these two states, shown as the dashed and dotted lines in Figure 5.2. They cross at the point marked as P in Figure 5.2 at about $C = -0.55$. Below it a single vortex will yield a smaller entropy compared with the symmetric state at the same energy. In other words the mean field theory predicts the formation of coherent single vortices for a ratio between background shear and vorticity larger than a negative value which is about -0.5 in this particular case.

This result is consistent with the numerical simulations done by Marcus [11]. In the simulations a background velocity distribution, e.g., $v_\theta = \beta r^2/3 + \bar{C}/r$, is assumed unchanged with the extra vorticity evolving on top of it. (His \bar{C} is equal to our $-C$. The β term corresponds to a gradient in the Coriolis force which we have not included, although this could easily be done by adding to the Hamiltonian an external potential $-\beta r^3$.) The background velocity acts as a shear on the evolving vorticity. One of the main results of the simulations is that for a range of background shear a single vortex is stable for $\langle \hat{\sigma} \rangle / \langle \omega \rangle$ greater than a critical value ranging from -0.1 to -0.2 , with $\langle \omega \rangle$ the average vorticity of the vortex and $\langle \hat{\sigma} \rangle$ the average value of shear at the vortex. This result holds for different values of \bar{C} and β , including the case $\beta = 0$. We believe that our calculations explain the basic mechanism of this simulation result. The difference between our numerical value of $\langle \hat{\sigma} \rangle / \langle \omega \rangle \approx -0.5$ and the simulation result is likely to be due to the different conditions used in the calculation and simulation.

As a final result we calculate the single-vortex solution with total vorticity, angular momentum, and background shear very similar to the simulation shown in Figure 8 in Marcus' paper [11], where a final coherent vortex is formed from an initial vortex layer. The vorticity contour plot shown in Figure 5.7 is in a good agreement with the final state of the simulation.

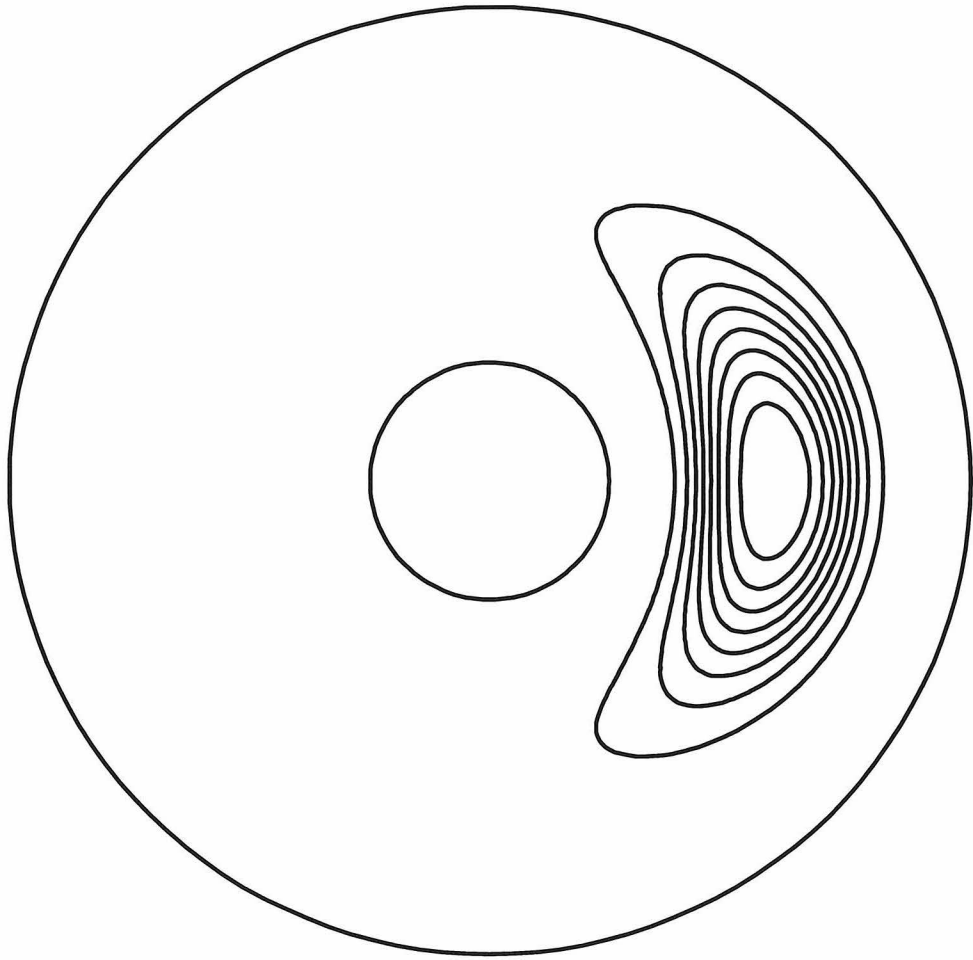


Figure 5.7: Vorticity contour plot for $Q = 3.14$, $M = 19.67$, $C = 0.875$, and $\beta = -12.8$. Contour levels are equally spaced.

Chapter 6 Dynamical Relaxation

6.1 Overview

In this chapter we use numerical simulations of the Euler equations to study the dynamical relaxation of a two-dimensional ideal fluid. The motivation is to check the validity of the ergodic assumption for the two-dimensional ideal flow in some well-controlled dynamical examples and to draw some general conclusions. We wish to study the following questions: 1) how does an initial vorticity distribution reach the final steady state? 2) what final states are reached and how do they compare with the statistical equilibria? In particular the vorticity mixing during the dynamics, which is needed for the ergodicity assumption to be valid, is closely monitored. Two recent experiments on the electron plasma [28] and fluid flow [23] have been carried out to study the final relaxation states. In the plasma experiment a hollow initial distribution is observed not to decay to a statistical equilibrium but to a state close to one having a minimum enstrophy, defined as $\int \omega^2 d\mathbf{r}$. The fluid experiment studies the final states from initial vortex arrays consisting of different numbers of vortices, and both states similar and different to thermal equilibria are observed. Here using numerical simulations we can precisely control the initial conditions and observe the dynamics very carefully, something that cannot be easily done in experiments. By carefully studying a few examples, we hope to shed some light on the general principle of the dynamics and the question of vorticity mixing in two-dimensional ideal fluids. Particular examples investigated in this chapter are different instabilities and the subsequent relaxation of a vortex ring.

It is well-known that a fluid shear layer may be susceptible to the Kelvin-Helmholtz instability and the instability will lead to vortex formation. For a vortex ring in a disk the unstable modes depend on the ratio between the ring radius and thickness. A larger ratio results a higher marginal mode number between unstable and stable

modes. By adding different m mode perturbations, we can study the dynamics and final equilibria of the vortex ring with different instability modes and hence different dynamical paths. Because the perturbations are small, the initial states are virtually identical and a unique thermal equilibrium is predicted from statistical mechanics. The final steady states and the “degree” of vorticity mixing during the dynamics resulting from the different dynamical paths can then be studied and compared to the thermal equilibrium.

The mean field equations describe a relation between the vorticity field $\omega(\mathbf{r})$ and the stream function $\psi(\mathbf{r})$, or the corotating stream function $\psi(\mathbf{r}) + \Omega r^2$ in a rotational symmetric system, for an ergodic flow, i.e., the vorticity being completely mixing and exploring all the possible states. For this reason this relation provides a precise test of the “degree” of mixing leading to a final steady state. Furthermore this relation can tell us how much mixing happens in different spatial regions. If in a region the vorticity experiences strong mixing, we expect $\omega(\mathbf{r})$ and $\psi(\mathbf{r}) + \Omega r^2$ to follow the mean field relation in this particular region although the whole vorticity distribution may not be a mean field state. In practice, every grid point in the system will yield a point in the plot of $\psi(\mathbf{r}) + \Omega r^2$ versus $\omega(\mathbf{r})$. In a steady state all the points will fall on a smooth curve and the curve can be compared with the mean field solution calculated from the same initial condition. More interesting and useful is that if the initial distribution is close enough to uniform such that the two-level initial vorticity is a good approximation, the mean field relation becomes

$$\ln[q/\omega(\mathbf{r}) - 1] = \beta[\psi(\mathbf{r}) + \Omega r^2] - \beta\mu,$$

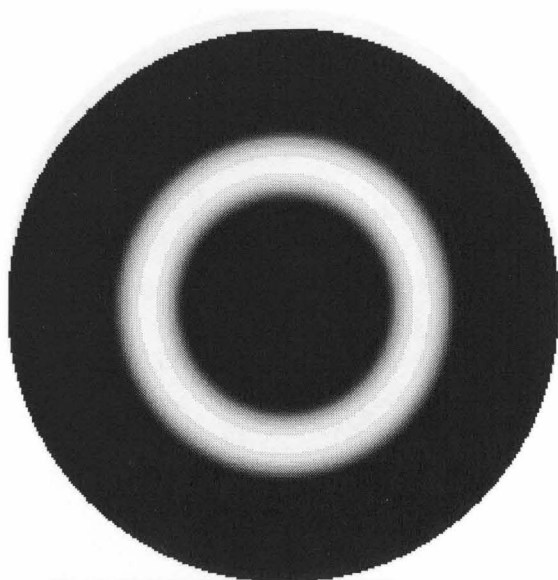
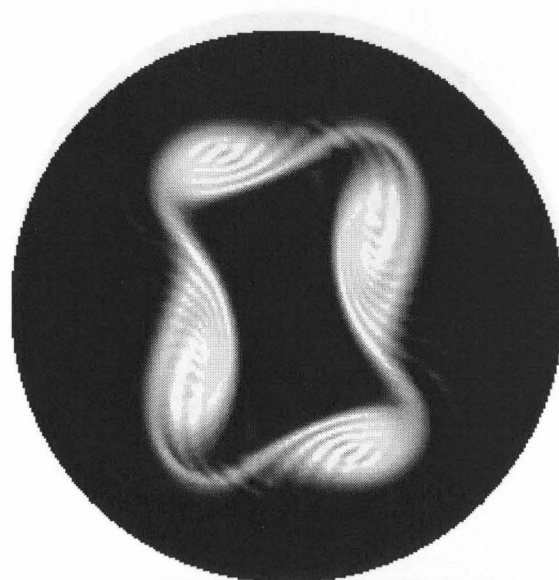
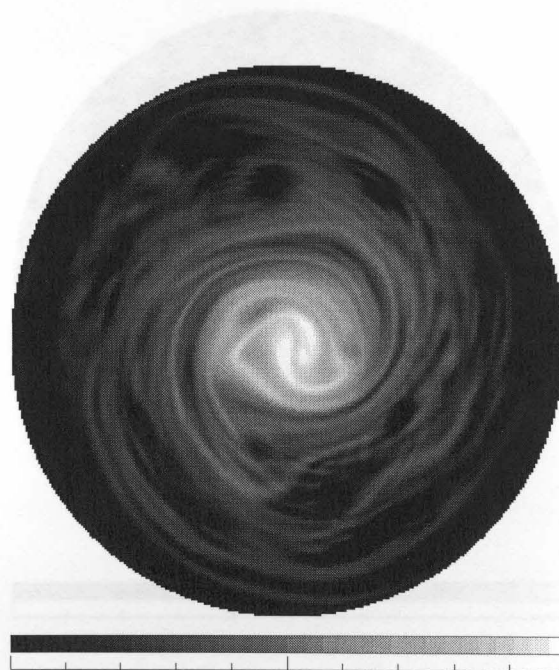
i.e., $\ln[q/\omega(\mathbf{r}) - 1]$ is a linear function of $\psi(\mathbf{r}) + \Omega r^2$. For a steady state tracing a curve on the $\ln[q/\omega(\mathbf{r}) - 1]$ versus $\psi(\mathbf{r}) + \Omega r^2$ plot, a linear segment will indicate a region with strong vorticity mixing. Actually this is even better than the direct comparison with the mean field solution because the presence of weakly-mixing regions will surely keep the parameters (e.g., β and μ) of the strongly-mixing region different from the global mean field solution.

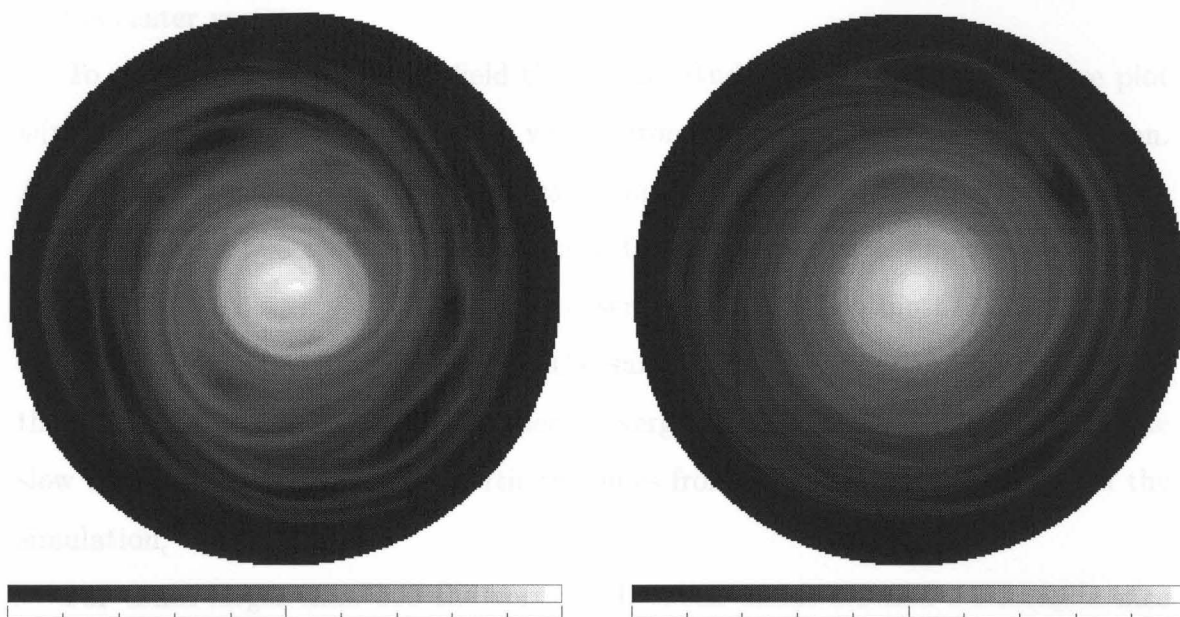
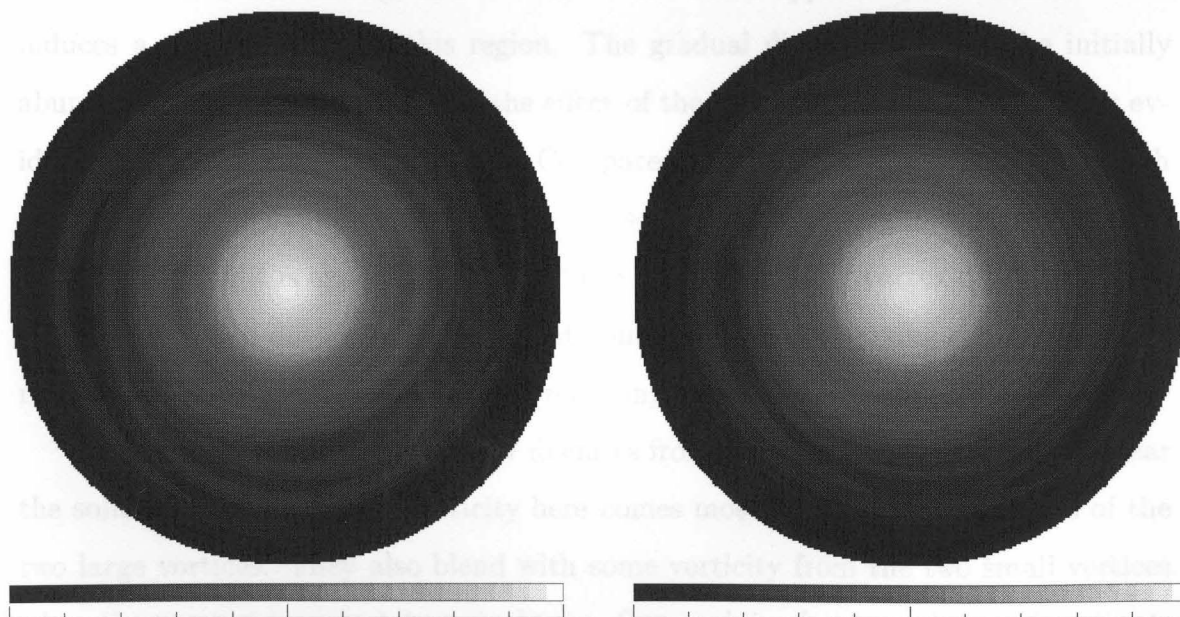
One last note is how to find Ω which is needed to plot the curve and in principle is only known from the mean field solution. Fortunately we can use the physical correspondence between 2Ω and the rotational frequency of a distribution that is not exactly axisymmetric. This usually applies to a final steady state where either a small displacement from the disk center or an elliptical distortion could be present. A calculation of the vortex position or orientation quickly yields Ω .

6.2 Relaxation of the $m=2$ Instability

As discussed in the previous section, we induce different m mode instabilities in a vortex ring by adding different perturbations. Snapshots of the dynamics with an $m = 2$ instability are shown in Figure 6.1. At first the $m = 2$ perturbation grows and leads to formation of two large vortices accompanied by two small ones. The large vortices quickly start a merging process by converging to the center and expelling filaments outside. The small vortices also converge and eventually are absorbed by the large ones during the merging. As the core regions of the large vortices move to the center they become adjacent to each other, separated only by a thin stretching region with low vorticity. The completion of the merger is signified by the vanishing of this thin stretching region and the formation of a single core. One conclusion immediately implied by this picture is that there is not much mixing happening for the vorticity in the core regions of the large vortices, while at the same time the small vortices are strongly mixed with the outer portions of the large vortices by being totally stretched into filaments during the absorption.

A long stretch of thin filament from each vortex extends to the outside region when the four vortices converge to the center. This filament formation may be considered as required by the conservation of angular momentum. With signs of secondary instability (see Figure 6.1 at $t = 100$), these filaments dissolve into a diffuse halo. Initially the halo is scattered with many vorticity holes which will gradually disappear on a time scale larger than the secondary instability time scale. Interestingly the holes possess some characteristics of coherent vortices, e.g., the merging of two holes is

Figure 6.1: (a) $t = 0$ (b) $t = 65$ Figure 6.1: (c) $t = 100$ (d) $t = 200$

Figure 6.1: (e) $t = 300$ (f) $t = 400$ Figure 6.1: (g) $t = 500$ (h) $t = 600$

Dynamical relaxation of a vortex ring in a disk with the $m = 2$ instability. Vorticity level is 0 to 1 from black to white.

observed. The evolution of this halo is also strongly influenced by the shear produced by the center vortex.

To compare with the mean field theory and study the vorticity mixing, we plot $\psi(\mathbf{r}) + \Omega r^2$ versus $\omega(\mathbf{r})$ in Figure 6.2, with Ω from the symmetric mean field solution. At $t = 300$ there is still a fairly large scattering of these points but with a converging trend. At $t = 500$ all the points already fall very close to a single curve except those points with a very low vorticity representing the small outmost filaments. After this time the curve basically remains the same except for the gradual decrease of the maximum vorticity and the further convergence to a single smooth curve. The slow decrease of the maximum vorticity comes from the small viscosity term in the simulation.

For times larger than 500 the vorticity between about 0.1 and 0.3 forms a nice straight line in Figure 6.2, indicating a complete mixing region. Examining the dynamical pictures in Figure 6.1, we find that this range of vorticity comes mostly from the filaments expelled by the converging vortices. The secondary instability of the filaments starts the mixing, and we believe the shear applied by the center vortex induces a strong mixing in this region. The gradual disappearance of the initially abundant vorticity holes, in which the effect of the shear is easily seen, is another evidence for the strong mixing process. Compared with the mean field solution, which assumes a total global mixing, plotted as the solid line, this straight segment is shifted slightly. This shift is expected in light of the large nonmixing vortex core at the center. However this does demonstrate that complete vorticity mixing can happen in a real flow and will yield the mean field relation, even if in only part of the system.

The vorticity between 0.3 and 0.7 deviates from a straight line but still stays near the solid line. Dynamically vorticity here comes mostly from the outer parts of the two large vortices. They also blend with some vorticity from the two small vortices when the two cores merge into a single one. Some mixing happens during the process but the curve in Figure 6.2 shows that the mixing is not strong enough to reach the mean field relation. Finally the core region with vorticity higher than 0.7 lies completely away from a straight line and the mean field solution, and is essentially

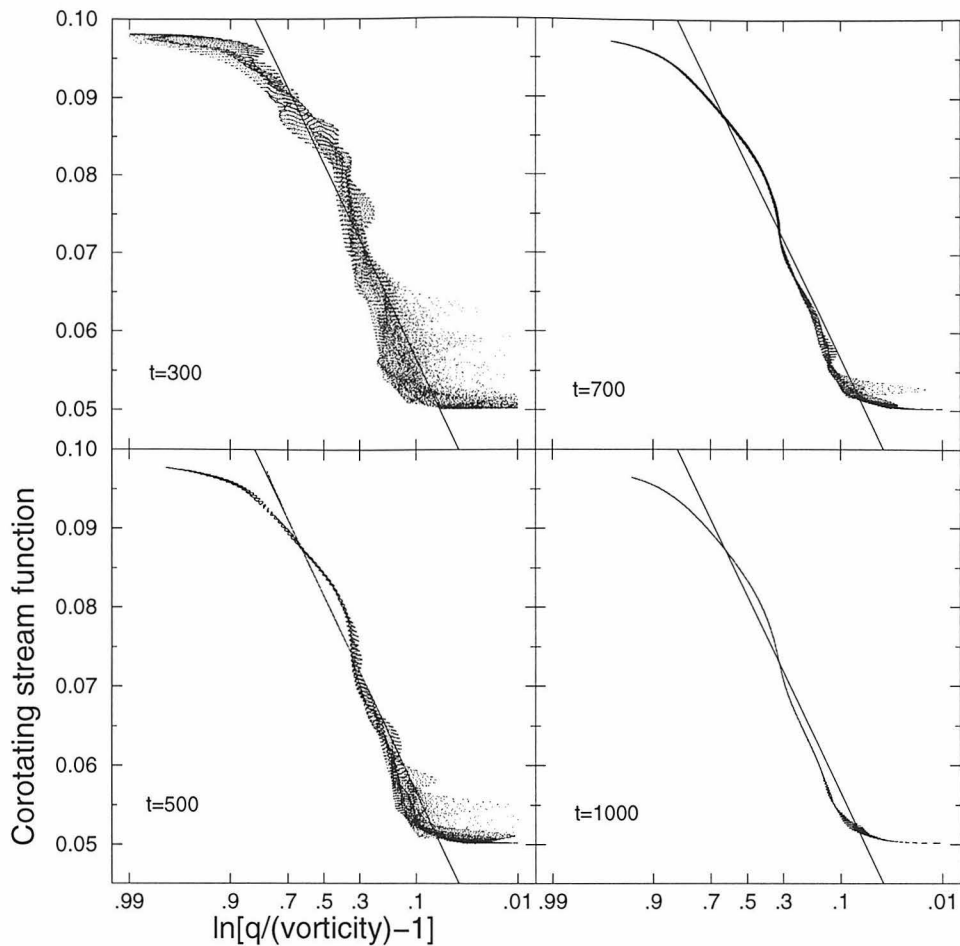


Figure 6.2: $\psi(\mathbf{r}) + \Omega r^2$ versus $\ln[q/\omega(\mathbf{r}) - 1]$ plots for the $m = 2$ instability at four different times. The solid line is the calculated symmetric mean field solution. Note that the numbers on x axis are the vorticity levels.

nonmixing. This confirms our previous prediction about the nonmixing nature of the core region merger.

In summary, the $m = 2$ instability first induces the formation of two large and two small vortices. These vortices quickly undergo a merging process in which the cores of the two large vortices do not mix with the low vorticity, and the vorticity at the outer part of the vortices experiences some degree of mixing. Also filaments extending to the outside region from the vortices during the merging eventually form a low vorticity halo around the center vortex. The shear effect of the center vortex induces complete mixing in the halo and the vorticity follows closely the mean field

relation.

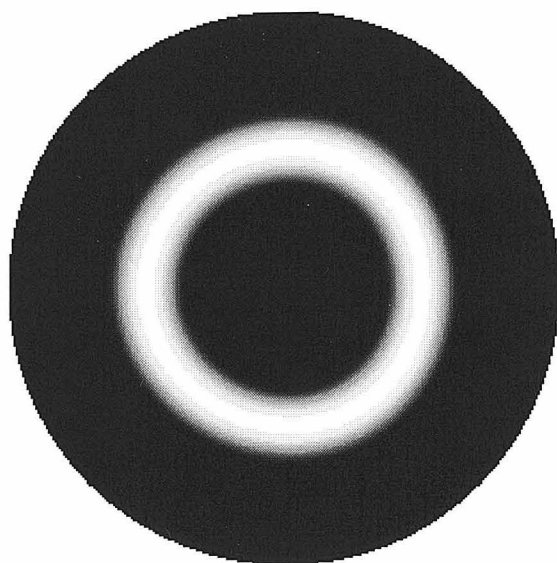
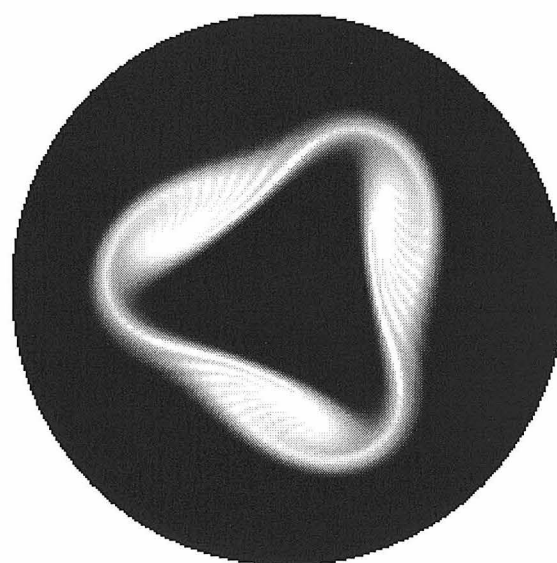
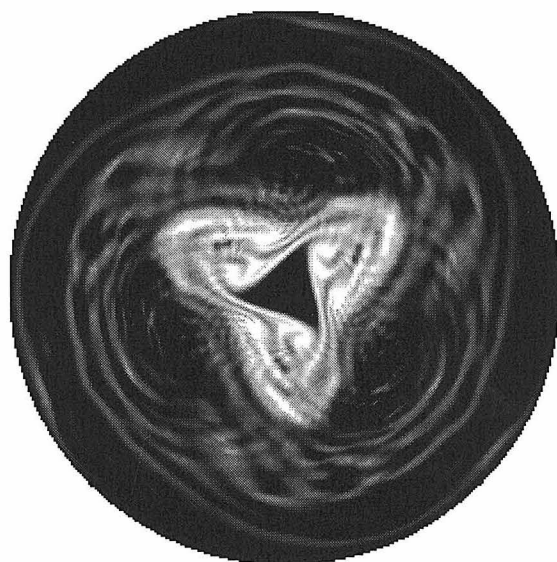
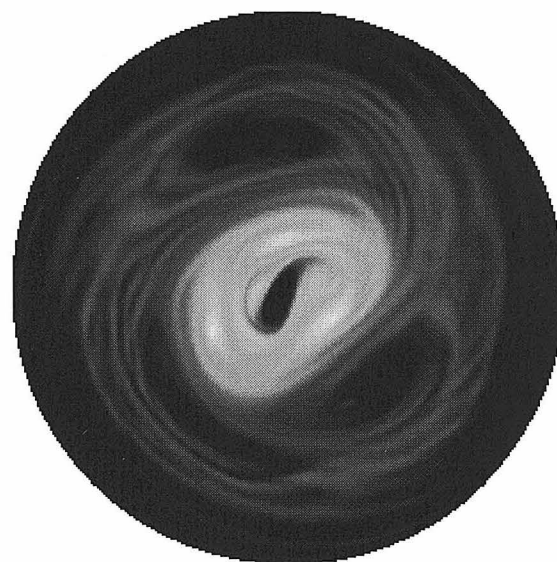
6.3 Relaxation of the $m=3$ Instability

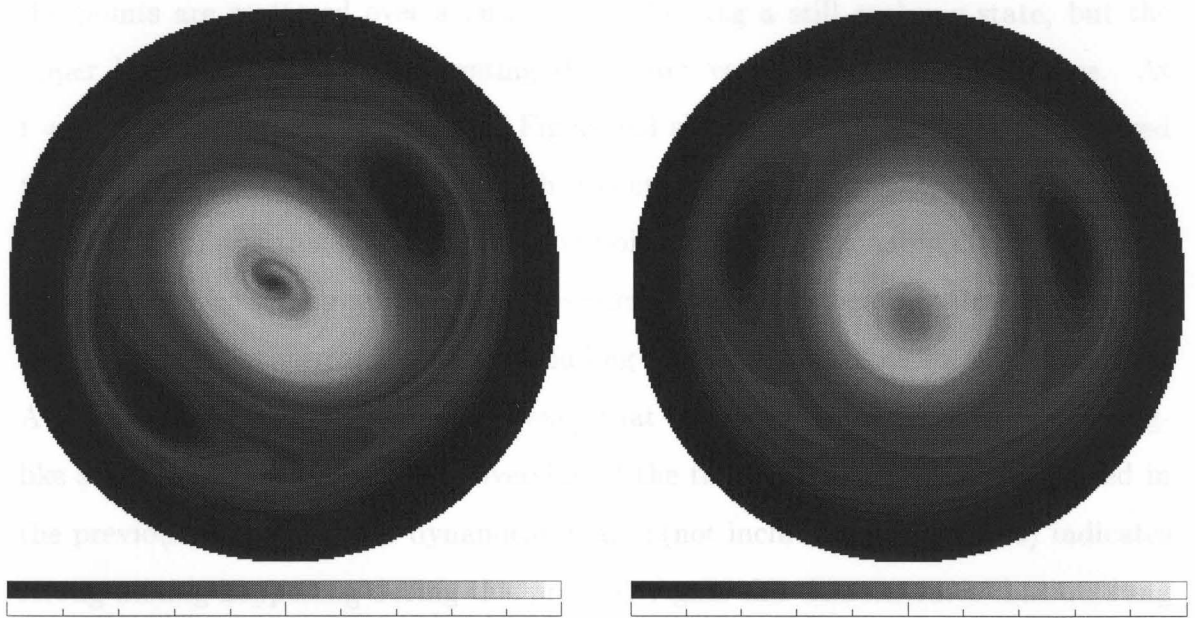
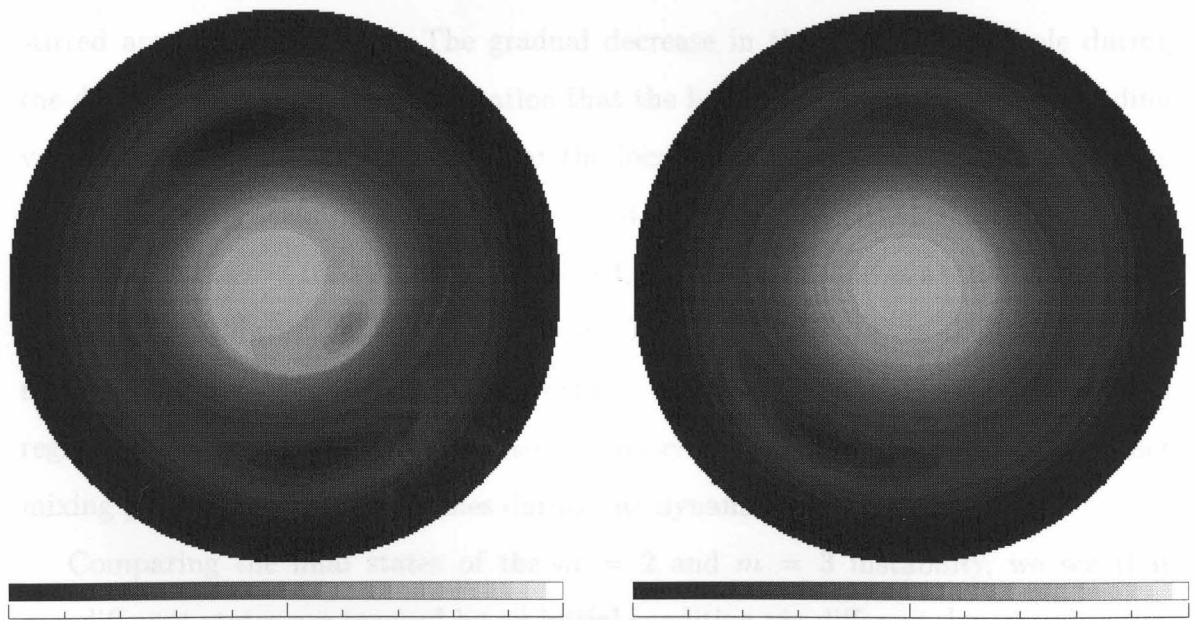
For the particular vortex ring discussed in the previous section, the unstable modes are $m = 2, 3$, and 4. When the $m = 3$ instability is induced to grow, three vortices quickly form. The dynamical sequence is shown in Figure 6.3. After their formation the three vortices immediately start converging to the center while expelling vortex filaments to the outside, similar to the $m = 2$ instability. However, instead of merging into a single vortex, the three vortices converge near the center forming a ring-like structure with a deep vorticity hole in the center. In the process of forming this structure, there is strong vorticity mixing going on, as is evident from the quick decrease of both the maximum vorticity and the area with high vorticity from $t = 100$ to $t = 400$.

In the meantime the filaments also quickly decay to a diffusive halo similar to the case of $m = 2$. However there are two or three major vorticity holes embedded in the halo. The number depends on the shape of the inner ring-like structure: three holes with a triangular shape earlier and two with an elliptical shape later. This formation of holes is understood from the distribution of the corotating stream function which exactly gives minimum regions at the positions of the holes. This is similar to the simulation of an ellipse done by Melander *et al.* [55]

Around $t = 400$ the vorticity distribution becomes an ellipse with a hole at its center and a low vorticity halo following the corotating stream function which has two minimum regions on the opposite sides of the ellipse. The dynamics after this point is the gradual outward drifting of the center hole. The drifting has a very slow time scale and the depth of the hole also gradually decreases. This motion of the hole still induces mixing as signalled by the further decrease of the maximum vorticity. It takes until very late, about $t = 1300$, for the hole to disappear at a vorticity level of about 0.6 and the vorticity distribution reaches a steady elliptical shape.

Again the mixing behavior of the dynamics will be seen more clearly in Figure 6.4

Figure 6.3: (a) $t = 0$ Figure 6.3: (b) $t = 30$ Figure 6.3: (c) $t = 100$ Figure 6.3: (d) $t = 200$

Figure 6.3: (e) $t = 400$ (f) $t = 800$ Figure 6.3: (g) $t = 1200$ (f) $t = 1500$

Dynamical relaxation of a vortex ring in a disk with the $m = 3$ instability. Vorticity level is 0 to 1 from black to white.

as a plot between the corotating stream function and the vorticity field. At $t = 200$ the points are scattered over a large area indicating a still evolving state, but the upper horizontal branch representing the center vortex hole is already there. At $t = 400$ the dynamical snapshot in Figure 6.3 shows that the vorticity has relaxed to an overall smooth distribution with a center hole. The corresponding graph in Figure 6.4 reflects this situation with the points staying reasonably close to a single curve except for some regions of small vorticity. More significant is that the portion with vorticity between 0.2 to 0.8 (excluding the hole) lies close to a straight line. A close examination of Figure 6.3 reveals that this portion corresponds to the ring-like structure formed from the converging of the three original vortices. As noted in the previous paragraph, the dynamical images (not included in Figure 6.3) indicates strong mixing happening during this process. Again this demonstrates that a strong mixing between the vorticity leads to the mean field relation.

The center hole starts the slow outward drift at about $t = 400$ and vanishes at about $t = 1300$ at a location with a vorticity level 0.6. The plots for $t = 800$ and $t = 1000$ in Figure 6.4 show that the region with vorticity larger than 0.5 is being stirred around by the hole. The gradual decrease in the depth of the hole during the drifting, we believe, is an indication that the hole is mixing with the surrounding vorticity. The vanishing of the hole at the location with vorticity level 0.6 suggests that a mixing process involving the hole and vorticity larger than 0.6 is completed. As shown in the $t = 1500$ graph in Figure 6.4, this mixing achieves a straight line, i.e., statistical equilibrium, in this inner region. The complete curve in the graph is now mainly composed of two straight segments. The system consists of two separated regions following their own mean field relations and they come from two distinct mixing processes at different times during the dynamical relaxation.

Comparing the final states of the $m = 2$ and $m = 3$ instability, we see that two different states are reached by an initial condition via different dynamical paths, a symmetric circular vortex and an elliptical vortex. Although they are both not the completely mixing statistical equilibria, the vorticity mixing and the mean field relation do play important roles in their final states.

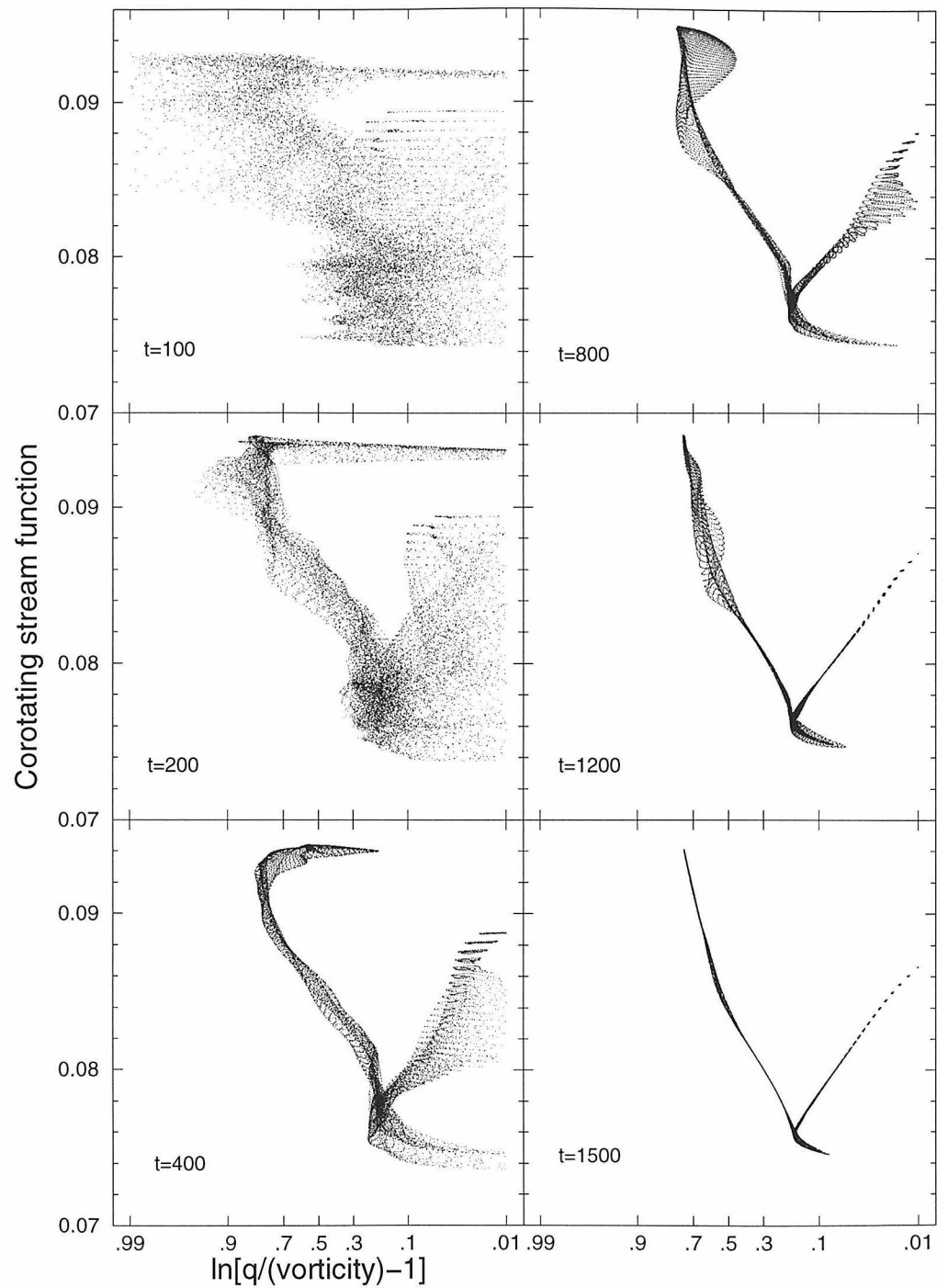


Figure 6.4: $\psi(\mathbf{r}) + \Omega r^2$ versus $\ln[q/\omega(\mathbf{r}) - 1]$ plots for the $m = 3$ instability at six different times. Again note that the numbers on x axis are the vorticity levels.

6.4 Higher Mode Instability

For the $m = 4$ perturbation, four vortices form from the initial instability. They also quickly converge to the center and start the vortex merging. In most aspects the dynamics is very similar to that of the $m = 2$ instability with two exceptions. First, since the four vortices are all about the same size, the merging is a more complicated four-vortex process instead of the mostly two-vortex merging in the $m = 2$ case. Nevertheless the key nonmixing property remains the same, namely that only the vorticity from outer parts of the vortices takes part in the mixing and the core regions remain unmixed, resulting in a nonmixing core in the final state. Second the final state is not a circular vortex but an elliptical vortex similar to the final state of the $m = 3$ case, but as mentioned with a significant nonmixing core. The relation between the vorticity field and corotating stream function for the final state is plotted in Figure 6.5a. It has a larger strong mixing region following the mean field relation than the $m = 2$ instability (Figure 6.2) does. This is reasonable due to the four-vortex merging. The curved upper portion indicates again the nonmixing center core.

We have also done an $m = 5$ simulation for a thinner vortex ring because the vortex ring in Figure 6.1 is stable against a $m = 5$ perturbation. First five vortices are formed. However in this case they are smaller and further apart, and initially they do not converge to the center. Instead, after a short period of time, two-vortex mergings between adjacent vortices begin, although the other vortices still have some influence. Filaments are also produced during the merging processes. In the end an elliptical vortex similar to the state in the $m = 4$ case is formed and Figure 6.5b again shows a nonmixing core and a strong mixing middle ground.

6.5 Conclusion

In this chapter we have studied the dynamical relaxation of a vortex ring to final steady states through different dynamical paths. The $m = 2$ to 5 cases of instability we studied all lack the total mixing (ergodicity) assumed in the statistical theory and

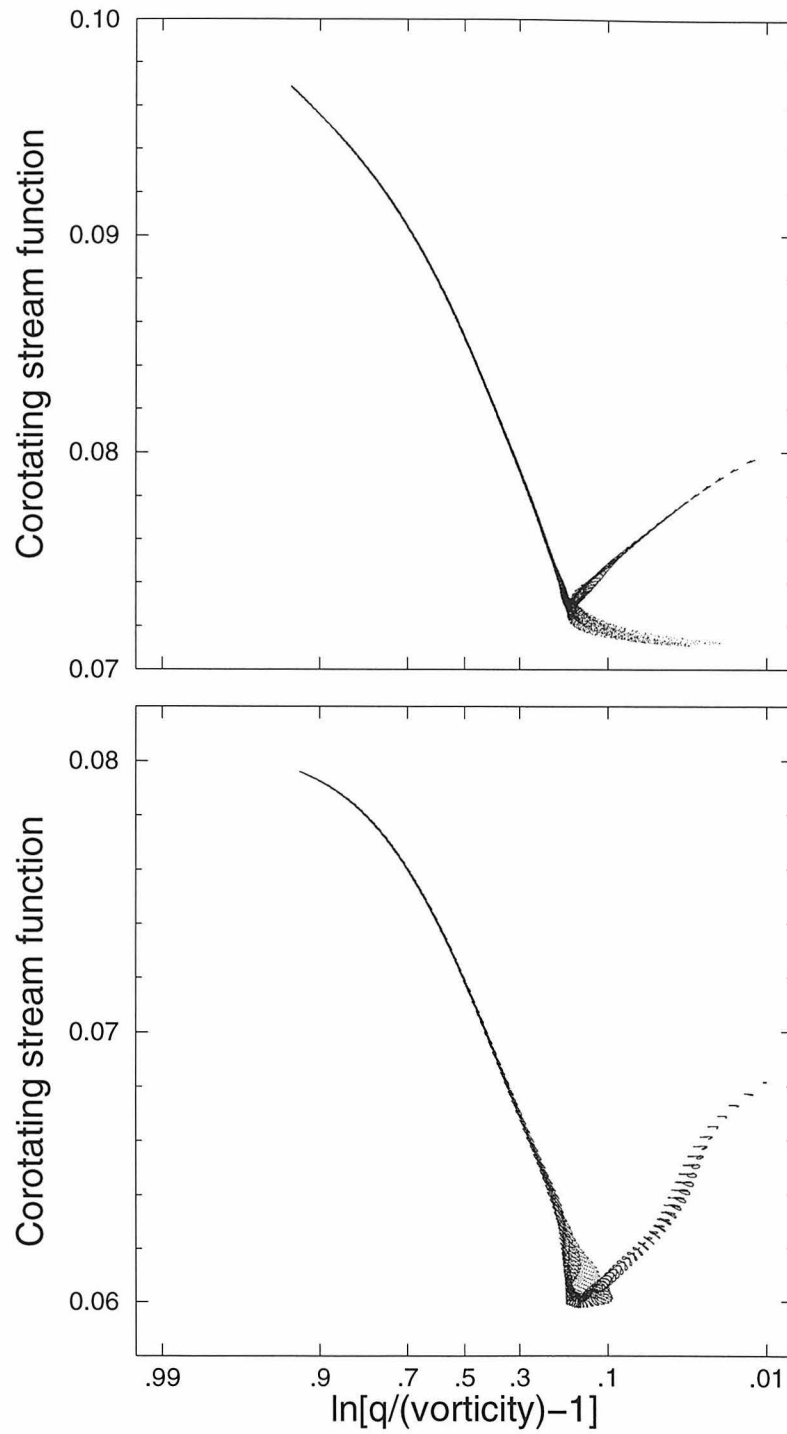


Figure 6.5: $\psi(\mathbf{r}) + \Omega r^2$ versus $\ln[q/\omega(\mathbf{r}) - 1]$ plots of the final steady states for the $m = 4$ (upper graph, referred to as (a)) and $m = 5$ (lower graph, referred to as (b)) instability.

do not reach a unique final state. However these dynamics also show that for each case strong vorticity mixing does happen in particular regions and at particular times. Whenever this is true, the vorticity and stream function follow the relation predicted by statistical mechanics. The most interesting example is the $m = 3$ instability where two mixing processes at different times and locations lead to two thermal equilibrium regions. We believe this demonstrates that the concept of thermal equilibrium for the turbulent mixing is valid and this is the most important conclusion from this chapter. A complete understanding of ergodicity and the implication for real physical systems remains to be answered by future work.

Chapter 7 Summary and Conclusion

We have studied in this thesis the coherent vortex states in two-dimensional ideal fluids using the statistical theory respecting all the infinite conservation laws of the flow and dynamic numerical simulations. The biggest question in the statistical theory is of ergodicity, i.e., whether the flow will explore all the phase space consistent with the conservation laws which results from complete flow mixing. Our general conclusion concerning ergodicity from our numerical simulations and the comparison between our statistical calculations and dynamical observations of past experiments and simulations is the following: Mixing processes during the dynamics have strong effects on the final steady states. Mixing may not be complete as required for ergodicity, but it can happen in particular regions or time periods, or even in some special flow modes. When strong mixing does occur, the flow structure follows very closely to the prediction of statistical mechanics.

Specifically, we have calculated the single-vortex solutions in a disk and studied the interesting bifurcation behavior between the symmetric and off-center vortices. Good agreement is found between the off-center vortices and the observed equilibrium states in an electron plasma experiment. Two-vortex mean field solutions are next calculated. By the comparison between the statistical calculations and experimental data, we are able to separate the mixing and nonmixing flow modes. We can then use the mixing mode to predict a merging critical separation which is in a good agreement with many simulation and experimental data. The experimental observations of two-vortex states in a large system also prompt us to propose “vorticity localization” which states that in special configurations the flow is confined in some small domains, and ergodicity and thermal equilibrium are reached locally. Vorticity localization is then used to explain the recent experimentally observed regular multiple-vortex patterns. We also use the mean field solutions to study the coherent vortex formation in an annulus under the influence of a background shear. The results are consistent with the

numerical simulation modeling the stable vortices in planetary atmospheres. Finally numerical simulations are used to investigate the different dynamical relaxations of a vortex ring. By carefully studying the dynamics and final states, we are able to demonstrate the relation between flow mixing and the statistical theory, and their implications for the final flow structure.

Bibliography

- [1] J. Miller, “Statistical mechanics of Euler equations in two dimensions”, *Phys. Rev. Lett.*, 65, 2137–2140, 1990.
- [2] R. Robert and J. Sommeria, “Statistical equilibrium states for two-dimensional flows”, *J. Fluid Mech.*, 229, 291–310, 1991.
- [3] J. Miller, P. B. Weichman, and M. C. Cross, “Statistical-mechanics, Euler equation, and Jupiter Red Spot”, *Phys. Rev. A*, 45, 2328–2359, 1992.
- [4] A. P. Ingersoll and P. G. Cuong, “Numerical model of long-lived Jovian vortices”, *J. Atmos. Sci.*, 38, 2067–2076, 1981.
- [5] M. V. Nezlin, “The soliton model for the Great Red Spot and other large vortices in planetary atmospheres”, *Sov. Astron. Lett.*, 10, 221–226, 1984.
- [6] G. P. Williams and T. Yamagata, “Geostrophic regimes, intermediate solitary vortices and Jovian eddies”, *J. Atmos. Sci.*, 41, 453–478, 1984.
- [7] G. P. Williams and R. J. Wilson, “The stability and genesis of Rossby vortices”, *J. Atmos. Sci.*, 45, 207–241, 1988.
- [8] T. E. Dowling and A. P. Ingersoll, “Potential vorticity and layer thickness variations in the flow around Jupiter’s Great Red Spot and white oval BC”, *J. Atmos. Sci.*, 45, 1380–1396, 1988.
- [9] P. S. Marcus, “Numerical-simulation of Jupiter’s Great Red Spot”, *Nature*, 331, 693–696, 1988.
- [10] T. Dowling and A. Ingersoll, “Jupiter’s Great Red Spot as a shallow water system”, *J. Atmos. Sci.*, 46, 3256–3278, 1989.

- [11] P. S. Marcus, “Vortex dynamics in a shearing zonal flow”, *J. Fluid Mech.*, 215, 393–430, 1990.
- [12] J. Sommeria, S.D. Meyers and H.L. Swinney, “Laboratory simulation of Jupiter’s Great Red Spot”, *Nature*, 331, 689–693, 1988.
- [13] J. C. McWilliams, “The emergence of isolated coherent vortices in turbulent flow”, *J. Fluid Mech.*, 146, 21–43, 1984.
- [14] A. Babiano, C. Basdevant, B. Legras, and R. Sadourny, “Vorticity and passive-scalar dynamics in two-dimensional turbulence”, *J. Fluid Mech.*, 183, 379–397, 1987.
- [15] M. E. Brachet, M. Meneguzzi, H. Politano, and P. L. Sulem, “The dynamics of freely decaying two-dimensional turbulence”, *J. Fluid Mech.*, 194, 333–349, 1988.
- [16] P. Santangelo, R. Benzi, and B. Legras, “The generation of vortices in high-resolution, two-dimensional decaying turbulence and the influence of initial conditions on the break”, *Phys. Fluid A*, 1, 1027–1034, 1989.
- [17] J. C. McWilliams, “The vortices of two-dimensional turbulence”, *J. Fluid Mech.*, 219, 361–385, 1990.
- [18] W. H. Matthaeus, W. T. Stribling, D. Martinez, S. Oughton, and D. Montgomery, “Decaying, two-dimensional, Navier-Stokes turbulence at very long times”, *Physica D*, 51, 531–538, 1991.
- [19] P. Tabeling, S. Burkhart, O. Cardoso, and H. Willaime, “Experimental study of freely decaying two-dimensional turbulence”, *Phys. Rev. Lett.*, 67, 3772–3775, 1991.
- [20] O. Cardoso, D. Marteau, and P. Tabeling, “Quantitative experimental-study of the free decay of quasi-2-dimensional turbulence”, *Phys. Rev. E*, 49, 454–461, 1994.

- [21] G. F. Carnevale, J. C. McWilliams, Y. Pomeau, J. B. Weiss, and W. R. Young, “Rates, pathways, and end states of nonlinear evolution in decaying two-dimensional turbulence: Scaling theory versus selective decay”, *Phys. Fluid A*, 4, 1314–1316, 1992.
- [22] W. H. Matthaeus, W. T. Stribling, D. Martinez, S. Oughton, and D. Montgomery, “Selective decay and coherent vortices in two-dimensional incompressible turbulence”, *Phys. Rev. Lett.*, 66, 2731–2734, 1991.
- [23] D. Marteau, O. Cardoso, and P. Tabeling, “Equilibrium states of two-dimensional turbulence: an experimental study”, *Phys. Rev. E*, 51, 5124–5127, 1995.
- [24] K. S. Fine, C. F. Driscoll, and J. H. Malmberg, “Measurements of a nonlinear diocotron mode in pure electron plasmas”, *Phys. Rev. Lett.*, 63, 2232–2235, 1989.
- [25] K. S. Fine, C. F. Driscoll, J. H. Malmberg, and T. B. Mitchell, “Measurements of symmetric vortex merger”, *Phys. Rev. Lett.*, 67, 588–591, 1991.
- [26] T. B. Mitchell, C. F. Driscoll, and K. S. Fine, “Experiments on stability of equilibria of two vortices in a cylindrical trap”, *Phys. Rev. Lett.*, 71, 1371–1374, 1993.
- [27] N. S. Pillai and R. W. Gould, “Damping and trapping in 2D inviscid fluids”, *Phys. Rev. Lett.*, 73, 2849–2852, 1994.
- [28] X.-P. Huang and C. F. Driscoll, “Relaxation of 2D turbulence to a metaequilibrium near the minimum enstrophy state”, *Phys. Rev. Lett.*, 72, 2187–2190, 1994.
- [29] A. J. Peurrung and J. Fajans, “Experimental dynamics of an annulus of vorticity in a pure electron plasma”, *Phys. Fluid A*, 5, 493–499, 1993.
- [30] X.-P. Huang, K. S. Fine, and C. F. Driscoll, “Coherent vorticity holes from 2D turbulence decaying in a background shear flow”, *Phys. Rev. Lett.*, 74, 4424–4427, 1995.

- [31] K. S. Fine, A. C. Cass, W. G. Flynn, and C. F. Driscoll, “Relaxation of 2D turbulence to vortex crystals”, *Phys. Rev. Lett.*, 75, 3277–3280, 1995.
- [32] L. Onsager, “Statistical hydrodynamics”, *Nuovo Cimento Suppl.*, 6, 279–287, 1949.
- [33] G. Kirchoff, *Lectures on mathematical physics, mechanics*. Teubner, Leipzig, 1877.
- [34] G. Joyce and D. Montgomery, “Negative temperature states for the two-dimensional guiding-centre plasma”, *J. Plasma Phys.*, 10, 107–121, 1973.
- [35] Y. B. Pointin and T. S. Lundgren, “Statistical mechanics of two-dimensional vortices in a bounded container”, *Phys. Fluid*, 19, 1459–1470, 1976.
- [36] T. S. Lundgren and Y. B. Pointin, “Non-Gaussian probability distributions for a vortex fluid”, *Phys. Fluid*, 20, 356–363, 1977.
- [37] T. S. Lundgren and Y. B. Pointin, “Statistical mechanics of two-dimensional vortices”, *J. Stat. Phys.*, 17, 323–355, 1977.
- [38] R. A. Smith, “Phase-transition behavior in a negative-temperature guiding-center plasma”, *Phys. Rev. Lett.*, 63, 1479–1482, 1989.
- [39] R. A. Smith and T. M. O’Neil, “Nonaxisymmetric thermal equilibria of a cylindrically bounded guiding-center plasma or discrete vortex system”, *Phys. Fluid B*, 2, 2961–2975, 1990.
- [40] R. Robert and J. Sommeria, “Relaxation towards a statistical equilibrium state in two-dimensional perfect fluid dynamics”, *Phys. Rev. Lett.*, 69, 2776–2779, 1992.
- [41] R. H. Levy, “Diocotron instability in a cylindrical geometry”, *Phys. Fluid*, 8, 1288–1295, 1965.

- [42] R. J. Briggs, J. D. Daugherty, and R. H. Levy, “Role of Landau damping in crossed-field electron beams and inviscid shear flow”, *Phys. Fluid*, 13, 421–432, 1970.
- [43] P. Chen and M. C. Cross, “Phase diagram for coherent vortex formation in the two-dimensional inviscid fluid in circular geometries”, *Phys. Rev. E*, 50, 2022–2029, 1994.
- [44] K. S. Fine, “Simple theory of a nonlinear diocotron mode”, *Phys. Fluid B*, 4, 3981–3984, 1992.
- [45] K. V. Roberts and J. P. Christiansen, “Topics in computational fluid mechanics”, *Comput. Phys. Comm.*, 3, 1972.
- [46] J. P. Christiansen and N. J. Zabusky, “Instability, coalescence and fission of finite-area vortex structures”, *J. Fluid Mech.*, 61, 219–243, 1973.
- [47] V. J. Rossow, “Convective merging of vortex cores in lift generated wakes”, *J. Aircraft*, 14, 283–290, 1977.
- [48] N. J. Zabusky, M. H. Hughes, and K. V. Roberts, “Contour dynamics for the Euler equations in two dimensions”, *J. Comput. Phys.*, 30, 96–109, 1979.
- [49] E. A. Overman and N. J. Zabusky, “Evolution and merger of isolated vortex structures”, *Phys. Fluid*, 25, 1297–1305, 1982.
- [50] M.V. Melander, N.J. Zabusky, and J.C. McWilliams, “Symmetric vortex merger in two dimensions: causes and conditions”, *J. Fluid Mech.*, 195, 303–340, 1988.
- [51] D.W. Moore and P.G. Saffman, “The density of organized vortices in a turbulent mixing layer”, *J. Fluid Mech.*, 69, 465–473, 1975.
- [52] P.G. Saffman and R. Szeto, “Equilibrium shapes of a pair of equal uniform vortices”, *Phys. Fluid*, 23, 2339–2342, 1980.

- [53] N. Whitaker and B. Turkington, “Maximum entropy states for rotating vortex patches”, *Phys. Fluid*, 6, 3963–3973, 1994.
- [54] D.W. Moore and P.G. Saffman. “Structure of a line vortex in an imposed strain”. In J. H. Olsen, A. Goldburg, and M. Rogers, editor, *Aircraft Wake Turbulence*, pages 339–354. Plenum, 1971.
- [55] M. V. Melander, J. C. McWilliams, and N. J. Zabusky, “Axisymmetrization and vorticity-gradient intensification of an isolated two-dimensional vortex through filamentation”, *J. Fluid Mech.*, 178, 137–159, 1987.